

DISSERTATION

**Light tetraquarks and mesons in a DSE/BSE  
approach**

WALTER HEUPEL

INSTITUT FÜR THEORETISCHE PHYSIK  
JUSTUS LIEBIG UNIVERSITÄT GIESSEN

# Table of contents

<b>Outline</b>	<b>5</b>
<b>A. Tetraquarks</b>	<b>6</b>
<b>1. Introduction</b>	<b>7</b>
1.1. Light tetraquarks and the quark model . . . . .	7
1.2. Tetraquarks in large $N_c$ . . . . .	10
1.3. Experimental situation and tetraquarks in other frameworks . . . . .	11
<b>2. Theoretical framework</b>	<b>13</b>
2.1. Green functions and the generating functional . . . . .	13
2.2. The QCD-Lagrangian . . . . .	14
2.3. Effective action and Dyson-Schwinger equations . . . . .	15
2.4. The quark DSE . . . . .	16
2.5. Bound state equations in QCD . . . . .	17
2.5.1. Tetraquark bound-state equation . . . . .	19
2.6. Normalization of the homogeneous BSE . . . . .	20
2.7. Solving strategies - Quark-DSE . . . . .	21
2.8. Solving strategies - BSE . . . . .	23
2.9. Truncation . . . . .	24
2.9.1. Rainbow ladder truncation - Quark . . . . .	24
2.9.2. Rainbow ladder truncation - Two-body kernel . . . . .	27
<b>3. Constructing a symmetric amplitude for tetraquarks</b>	<b>30</b>
3.1. General considerations . . . . .	30
3.2. Phase space . . . . .	31
3.2.1. Doublet . . . . .	34
3.2.2. Triplet $\mathcal{T}_0$ . . . . .	36
3.2.3. Triplet $\mathcal{T}_1$ . . . . .	38
3.3. Flavor structure . . . . .	40
3.4. Color structure . . . . .	42
3.5. Tensor structure . . . . .	43
3.5.1. Quantum numbers . . . . .	44
3.5.2. LS-decomposition . . . . .	47
3.5.3. Construction of symmetric tensor structures . . . . .	49

3.6. Amplitude conventions and Fierz transformations . . . . .	50
3.7. Polynomial representation and interpolation . . . . .	51
<b>4. Singularity structure and threshold effects</b>	<b>54</b>
4.1. Phase space arguments . . . . .	54
4.2. Numerical evidence - Shape of amplitudes . . . . .	56
4.3. Numerical evidence - Eigenvalue spectrum . . . . .	59
4.3.1. Light quarks . . . . .	59
4.3.2. Heavy quarks . . . . .	60
4.4. Pole ansatz . . . . .	62
<b>5. Results</b>	<b>65</b>
5.1. Comparing Lorentz invariants . . . . .	65
5.2. Mass curve . . . . .	69
5.3. Masses of the scalar nonet . . . . .	73
<b>6. Conclusion and outlook</b>	<b>74</b>
<b>B. Beyond Rainbow ladder</b>	<b>77</b>
<b>7. Introduction</b>	<b>78</b>
<b>8. Theoretical foundation</b>	<b>80</b>
<b>9. Constructing the kernel</b>	<b>84</b>
9.1. The 2BC Vertex model . . . . .	85
9.2. The Ball-Chiu vertex model . . . . .	86
9.3. The Munczek vertex model . . . . .	88
<b>10. Numerical results</b>	<b>91</b>
<b>11. Conclusions</b>	<b>95</b>
<b>Appendices</b>	<b>97</b>
<b>A. Appendix - Tetraquarks</b>	<b>98</b>
A.1. Eigenvalue curves . . . . .	98
A.2. Phase space supplements . . . . .	102
A.3. Color traces . . . . .	104
A.4. Momentum routing and $S_4$ relations . . . . .	105
A.5. $S_4$ toolbox . . . . .	107
<b>B. Appendix - Beyond rainbow ladder</b>	<b>111</b>
B.1. Constructing beyond ladder kernels . . . . .	111
B.2. Massless pion and BC vertex . . . . .	112

B.3. Gluon model . . . . .	115
B.4. Munczek model . . . . .	116

<b>Bibliography</b>	<b>117</b>
---------------------	------------

## Outline

The work is divided into two parts. The first part is dedicated to the investigation of light and heavy scalar tetraquarks in a four-body approach within the Dyson-Schwinger/Bethe-Salpeter (DSE/BSE) framework.

The second part of the work deals with a novel approach to describe light  $\bar{q}q$  mesons with a ‘beyond rainbow-ladder’ truncation. That part is entirely based on the already published paper [1], a combined work of the author of this thesis, T. Göcke and C.S. Fischer.

The first part is motivated by the old idea that the lightest scalar nonet in the hadron spectrum is in fact a tetraquark nonet instead of an ordinary  $\bar{q}q$  nonet. Additionally, recent findings of charged charmonia, which can be interpreted as a ‘smoking gun’ for tetraquarks, rekindled the interest in tetraquarks in general.

The approach used in this work was already applied successfully in the meson sector (two-body equation) and the nucleon sector (three-body equation), and therefore it is interesting to apply similar techniques to the four-body equation that describes tetraquark bound states. Within our framework, the equal-mass tetraquarks are investigated and besides shedding some light on the enigmatic nature of the  $\sigma$ -particle, we will also investigate all-charm/strange tetraquarks.

The second part deals with a general framework to describe  $\bar{q}q$  bound states beyond the frequently used rainbow ladder approximation for the quark-gluon interaction inside the meson. At the first glance, this is unrelated to the first part that deals with tetraquarks, except for some overlap of the theoretical and numerical framework used. But on a second look, the nature of the scalar particle can only be understood, if its  $\bar{q}q$  and  $\bar{q}q$  component are well under control.

Following this argument, in the first part of this thesis the DSE/BSE-framework is applied for the first time to study scalar tetraquarks in the four-body picture, improving and supplementing our previous studies of scalar tetraquarks in the two-body picture, whereas the second part of this thesis is dedicated to obtain a better description and understanding of the  $\bar{q}q$ -mesons in general and the scalar meson in particular.

**Part A.**

# **Tetraquarks**

# 1. Introduction

In this chapter we will provide arguments found in literature for the existence of tetraquarks, in particular scalar tetraquarks. For a review of scalar mesons and their long and winding story through the history of hadron physics, see ref. [2].

## 1.1. Light tetraquarks and the quark model

Since the introduction of the quark model in the 60' [3], the bulk properties of the hadron spectrum are related to multiplets formed by quarks in the flavour  $SU(3)$ -fundamental representation. The mesons, described as  $q\bar{q}$ -states, can be ordered into nonets by the  $SU(3)$  relation

$$3 \otimes \bar{3} = 8 \oplus 1, \quad (1.1.1)$$

and the baryons reside in multiplets formed by

$$3 \otimes 3 \otimes 3 = 10 \oplus 8 \oplus 8 \oplus 1. \quad (1.1.2)$$

Even when taking into account that the flavour  $SU(3)$  symmetry is explicitly broken by the different quark masses, the model is very successful in explaining the plethora of different mesons and baryons in the hadron spectrum and provides insight into the origin of their mass splittings.

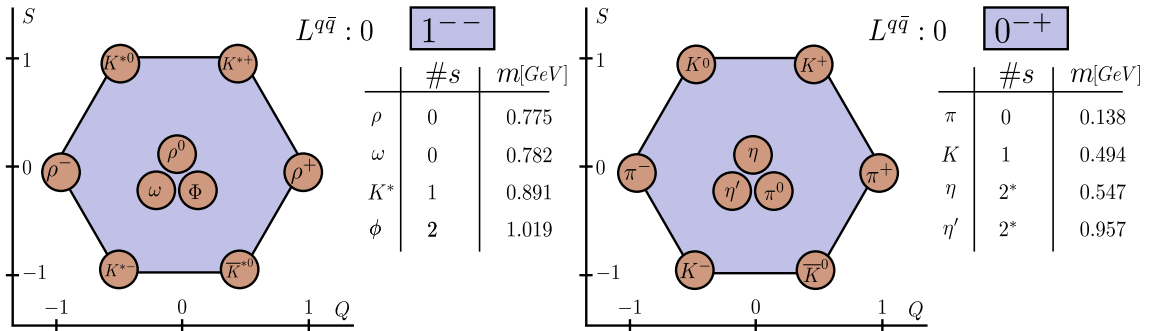


**Figure 1.1.:** Lowest nonet in the  $0^{-+}$  and  $1^{--}$  channel. The electrical charge is denoted by  $Q$ , the strangeness by  $S$  and the number of strange and anti-strange quarks by  $\#s$ . For the  $\eta$  mesons,  $\#s$  is not well defined, because the mixing angle between them is not zero. All masses are rounded and taken from the PDG [4].

As examples, the vector nonet and the pseudo scalar nonet are shown on the left and right side of figure 1.1 respectively, including the tabulated masses of its members. The mass hierarchy is closely tied to the quark content. The much heavier strange quark causes

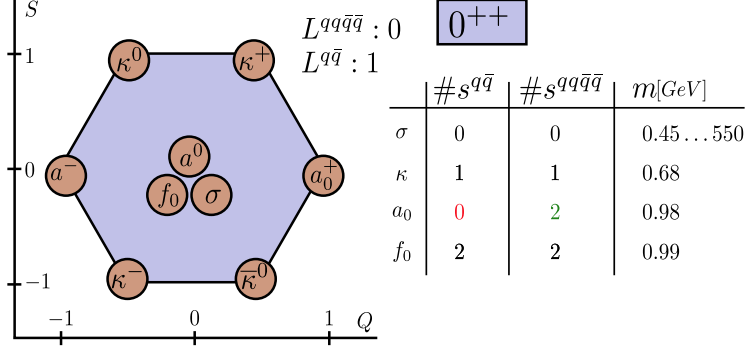


**Figure 1.2.:** Lowest nonet in the  $0^{++}$  channel. The first and second column show the s-quark content in the  $\bar{q}q$  and  $\bar{q}q\bar{q}q$  picture respectively. The red and green colour highlight the striking discrepancy of the  $\bar{q}q\bar{q}q$  and  $\bar{q}q$  picture.

the increased masses of the  $K^*$  and the  $\Phi$  in the vector nonet and a similar argument also explains the increased masses of the  $K, \eta$  and  $\eta'$  in the pseudo scalar nonet. The large mass splitting between  $\eta$  and  $\eta'$  is attributed to the anonymously broken axial  $U(1)$  symmetry [5, 6].

State	$J^{PC}$	$L$	$S$
Pseudo scalar	$0^{-+}$	0	0
Scalar	$0^{++}$	1	1
Vector	$1^{--}$	0	1
Axial vector	$1^{++}$	1	1
Pseudo vector	$1^{+-}$	1	0

**Table 1.1.:**  $L$ - $S$ -decomposition of the scalar, pseudoscalar, vector and axial vector mesons in the  $\bar{q}q$  picture.

In the case of the scalar  $\bar{q}q$  nonet, the quark model has some difficulties to explain the masses of its members. Before going into details, some basic facts concerning multiplets are provided.

Multiplets are denoted by their quantum numbers, written as  $J^{PC}$ , where  $J$  is the total angular momentum obtained from coupling the spin  $S$  to the orbital angular momentum  $L$ . In the quark model, the parity  $P$  of a two-quark bound state is related to  $L$  via  $P = (-1)^{L+1}$  and the C-parity  $C$  is related to  $S$  and  $L$  via  $C = (-1)^{L+S}$ . In table 1.1 we collected all the possible multiplets in the  $\bar{q}q$ -picture with  $J = 0, 1$  and provided the corresponding  $L$  and  $S$  quantum numbers.

Similar to classical quantum mechanics, one associates orbital angular momentum with excitations and therefore expects a higher mass for higher  $L$ . In the same way, a state with spin  $S = 0$  is presumed to have a lower mass than a state with  $S = 1$ . For example, the  $1^{--}$  has orbital angular momentum  $L = 0$  and spin  $S = 1$  whereas the  $1^{++}$  nonet has  $L = 1$  and  $S = 1$ . Looking at the mass of the neutral isospin triplet meson in the vector nonet, the  $\rho^0$ , which has a mass of  $0.775 \text{ GeV}$  and comparing it to the mass of the neutral

isospin triplet meson in the axial vector nonet, the  $a_1^0$ , which has a mass of  $1.26 \text{ GeV}$ , we see that the nonet with the higher  $L$  features indeed larger masses.

For the  $\bar{q}q$  scalar nonet which has an orbital angular momentum of  $L = 1$  and a spin of  $S = 1$ , one would predict that the masses of the members of the scalar nonet lay *above* the vector nonet. Interestingly, this is not the case as can be seen by comparing the masses of the scalar nonet, shown on the right side of figure 1.2, with the masses of the pseudo scalar and vector nonet; the scalar nonet in the  $\bar{q}q$  picture is located *between* the pseudo scalar and the vector nonet.

Another peculiarity in the  $\bar{q}q$  scalar nonet is the breakdown of the quark model to explain the mass ordering. The  $a_0(980)$  and the  $f_0(980)$  are much heavier than the  $\sigma$  and the  $\kappa$ . Whereas in the  $\bar{q}q$  picture the  $f_0(980)$  contains two  $s$ -quarks, explaining its large mass compared to the  $\sigma$  and  $\kappa$  which contain zero and one  $s$ -quarks respectively, the  $a_0(980)$  has no  $s$ -quark content. According to the quark model, predicting an  $a_0$  that is much lighter than both the  $f_0$  and the  $\kappa$ , a heavy  $a_0$  is a completely counter intuitive result.

But already in the 70', it was realized that a combination of four quarks, does not only yield a colour singlet state, necessary by confinement, but also reproduces the mass ordering in the scalar nonet nicely [7]. In detail this 'improved' mass ordering is shown in the table on the right side of figure 1.2. In the four quark picture the  $a_0$  contains two  $s$ -quarks and the large mass is a direct consequence of the quark content. At the same time, the  $s$ -quark content of the  $\kappa$ ,  $f_0$  and  $\sigma$  is not changed in the  $\bar{q}q$  picture, so that the mass order within the scalar nonet can be explained by the quark content only. It also turns out that the orbital angular momenta and the spin of the scalar tetraquark nonet are all zero [8]. According to the argument that small  $L$  and  $S$  lead to a small mass, the lightness of the scalar nonet finds a natural explanation.

In general, the most appealing feature of the four quark picture for the light scalars is the 'conservation of simplicity' of the quark model: gross features, decay patterns and mass splittings can be understood by simply investigating the structure of the multiplet and the quark content with no additional unexpected mechanisms necessary. Besides the valid question, 'if tetraquarks exist in general', the applicability of the quark-model to explain the masses of the scalar nonet was the beginning of the rising interest in tetraquarks.

Besides the masses, also some of the decay patterns and the width of the light scalar mesons can be explained by the four-quark picture [7, 9]: The  $\sigma$  has an enormous width of about  $0.35 \text{ GeV}$  which is of the same order as its pole mass of about  $0.45 \text{ GeV}$  [10]. On a qualitative level, the decay patterns of hadrons can be understood by considering the OZI-rule [11, 12, 13] which states that that the more internal gluon lines a decay contains, the more the process is suppressed. The dominant decay of the  $\sigma$  is the  $\sigma \rightarrow \pi\pi$  channel [14]. In terms of a  $\bar{q}q$  meson, this involves at least one internal gluon, whereas in the four quark picture, the decay would be facilitated by a gluon-less breakup into two pions, giving a natural explanation for the enormous width of the particle and its dominant decay into two pions. Regarding the other mesons of the nonet, the dominant decay of  $a_0$  into  $\pi\eta$  would find its explanation in the quark content of the four quark picture, whereas in the

two quark picture this decay would be yet another puzzle.

Concluding this section, we summarize that adhering to the simplicity of the quark model, the four quark picture is a much more ‘natural’ candidate to explain the lowest laying scalar nonet than the  $\bar{q}q$  picture.

## 1.2. Tetraquarks in large $N_c$

A useful tool to investigate certain aspects of QCD is the  $1/N_c$  expansion [15, 16]. Here  $N_c$  specifies the the number of colours of the theory which reads  $N_c = 3$  in the case of QCD. In the limit of  $N_c \rightarrow \infty$ , a hierarchy of contributing Feynman diagrams can be established with  $1/N_c$  as expansion parameter. According to an argument by Coleman [17], tetraquarks disappear from the spectrum for  $N_c \rightarrow \infty$ . As to whether or not  $N_c = 3$  is a large number, this argument was turned around to regard tetraquarks as unlikely states. Upon a closer inspection by Weinberg [18], it was found that the argument by Coleman [17] was flawed.

At this point we will provide a short sketch of the arguments, based on the review in ref. [19]. Introducing the quark/anti-quark bilinear

$$B_i(X) = \bar{q}\Gamma_i q \quad (1.2.1)$$

with  $\Gamma_i$  some spin-flavour object, the four two-quark/two-anti-quark operator  $Q$  can be expanded as

$$Q(x) = \sum_{ij} C_{ij} B_i(x) B_j(x), \quad (1.2.2)$$

with  $C_{ij}$  some expansion coefficients. Investigating the correlator

$$\begin{aligned} \langle T[Q(x)Q(y)^\dagger] \rangle &= \sum_{ijkl} C_{ij} C_{kl} \langle T[B_i(x)B_k(y)^\dagger] \rangle \langle T[B_j(x)B_l(y)^\dagger] \rangle \\ &\quad + \langle T[B_i(x)B_j(x)^\dagger B_k(y)B_l(y)^\dagger] \rangle + \mathcal{O}(N_c^0), \end{aligned} \quad (1.2.3)$$

one finds that the first term, corresponding to freely propagating  $\bar{q}q$  mesons, scales as  $N_c^2$ , and the second term, related to a genuine interacting four quark state, scales as  $N_c$ . Thus Coleman concluded that the tetraquark does not exist because it is suppressed by a factor of  $1/N_c$  compared to two non-interacting mesons. Weinberg pointed out that this correlator is the wrong object to look at and one should rather investigate the decay amplitude of a tetraquark into two mesons, which is proportional to the following expression:

$$\begin{aligned} \frac{1}{N_c^{3/2}} \langle T[Q(x)B_n(y)B_m(z)] \rangle &= \frac{1}{N_c^{3/2}} \sum_{ij} C_{ij} \langle T[B_i(x)B_n(y)] \rangle \langle T[B_j(x)B_m(z)] \rangle \\ &\quad + \frac{1}{N_c^{3/2}} \langle T[Q(x)B_i(y)B_n(y)] \rangle_{con} + \mathcal{O}(1/N_c). \end{aligned} \quad (1.2.4)$$

The first term on the right hand side is the disconnected part, corresponding to two freely propagating meson. Furthermore, this term is the leading one in a  $1/N_c$  expansion. Upon further calculations that can be found in the review of ref. [19], the decay width obtained from this term scales with  $N_c$ . One would therefore conclude that the tetraquark becomes an infinitely broad state in the  $N_c \rightarrow \infty$  limit. But as pointed out by the authors in [19], before taking the limit  $N_c \rightarrow \infty$ , one has to ‘amputate’ the quark legs, by projecting on the quark poles. This eliminates the disconnected first part and promotes the second part to be the leading term in an  $1/N_c$  expansion. Because the decay width obtained from the second term scales with  $1/N_c$ , one concludes on the contrary that the tetraquark is a *narrow* state in the large  $N_c$  limit. Therefore, from a large  $N_c$  point of view, there is no reason that tetraquarks are not a part of the hadron.

### 1.3. Experimental situation and tetraquarks in other frameworks

The literature on light scalars is vast and spans more than four decades of combined experimental and theoretical effort to elucidate their nature. In this short chapter we will just outline the experimental status in general.

The scalar sector is a notoriously difficult channel for experiments. In contrast to the vector channel  $1^-$ , which can be studied directly by  $e^-e^+$  colliders, the scalar channel is only accessible via secondary processes, for example in nucleon-pion scattering experiments. The early analysis of data from  $N\pi$ -scattering [20, 21] have large uncertainties and were contradictory, so that the  $\sigma$  or  $f_0(500)$  as bound-state or resonance was excluded from the PDG and was instead interpreted as a  $\pi\pi$ -scattering state.

Only later experiments, studying heavy meson decays [22] and kaon decays [23] could establish the  $\sigma$  as a physical particle, leading ultimately to its reappearance in the PDG but without solving the puzzle of  $\bar{q}q$  vs  $\bar{q}\bar{q}qq$ .

Besides the search for the  $\sigma$  pole in heavy meson decays, dispersive approaches using the Roy equations [24] to describe the  $\pi\pi$ -scattering were able to establish the  $f_0(500)$  as complex poles in the scattering matrix. Besides using the data of scattering experiments as input, these dispersive approaches utilize unitarity, analyticity and crossing symmetries as constraints. One much cited result for the  $\sigma$  is  $m_\sigma = 441_{-8}^{+16}$ ,  $\Gamma_\sigma = 544_{-25}^{+18} MeV$  [10] which is also backed up by a more recent calculations [25, 26, 27].

Besides the  $\sigma$ , the other particles of the scalar nonet are also assumed to be established. Using the Roy equations, the  $\kappa$  or  $K^*(800)$  was found in  $\pi K$ -scattering [28] and in  $J/\Psi$ -decays [29] and also the  $f_0$  and the  $a_0$  are found by dispersive methods, see refs. [25, 30].

Even if the experimental situation regarding the existence of the light scalar can be seen as more or less solved, it is difficult for experiments to gain insight into the structure of the scalar nonet and answer the question whether particles are  $\bar{q}q$  states or tetraquarks. Therefore, it is the task of theory to give an answer to this question. In the following we will provide a short list of various approaches that investigated light scalars in general and scalar tetraquarks in particular.

A hint to the non ordinary nature of the light scalar mesons is given by its Regge-behavior. Different to the vector meson, a pure  $\bar{q}q$  state, that develops a linear Regge-trajectory, the  $\sigma$  was found to show a non-linear behavior with a reduced slope [31], strongly indicating that the  $\sigma$  is more than an ordinary  $\bar{q}q$  meson.

Also studies in the large  $N_c$  limit employing unitarized Chiral Perturbation Theory, suggest a strong non  $\bar{q}q$  component for the  $\sigma$ , as do studies employing an instanton induced, six-fermion effective Lagrangian [32].

In ref. [33] the scalar tetraquark nonet and the scalar  $\bar{q}q$  nonet was investigated in a QCD sum rule approach. The authors found the tetraquark nonet to have masses below  $1\text{ GeV}$  whereas the  $\bar{q}q$  nonet featured masses well above  $1\text{ GeV}$ . A similar result that identifies the low-lying scalars with tetraquarks and finds the scalar  $\bar{q}q$  nonet to be much heavier was obtained in ref. [34] using a linear  $\sigma$ -model. Also in a relativistic diquark-diquark model, see ref. [35], the scalar tetraquark nonet was found to be light.

The situation on the lattice is still inconclusive. The authors in [36] found a non-zero  $\bar{q}\bar{q}qq$  contribution for the  $\sigma$  and  $\kappa$ , whereas an earlier calculation from the same group did not show such a contribution [37]. A recent study [38] investigated the influence of disconnected diagrams and found that the  $\sigma$  is maybe a molecular  $\pi\pi$ -state.

The  $\kappa$  and  $a_0$  were also investigated in ref. [39] and in contrast to [36], the  $\kappa$  was found to have no tetraquark component. In summary, a final answer from the lattice on the nature of the light scalars and their tetraquark contributions is not available yet, but there exist hints that non  $\bar{q}q$  parts are present.

**Heavy tetraquarks** Because of technical limitations, this work will focus on the  $0^{++}$  quantum numbers with equal mass quarks and we will mention the case of heavy-light tetraquarks only briefly. The most prominent examples of charmonia that show a behavior that is difficult to understand in the usual  $\bar{q}q$ -picture are the  $XYZ$ -states. The forerunner of the so called  $XYZ$ -states is the  $X(3872)$  discovered by Belle [40], an extremely narrow resonance at the  $D^{*0}\bar{D}^{*0}$  threshold. The closeness to the threshold, coupled to a small width and its puzzling decay patterns make it a potential candidate for a tetraquark. Some recent lattice calculations [41] find the tetraquark contribution to be small, but a definite answer to the nature of the  $X(3872)$  is still missing. Another interesting charmonium state is the  $Z_c^+(3900)$  that was discovered at Bell [42]. This state cannot be a pure  $\bar{q}q$  state because of its charge, and therefore is most likely a tetraquark. A compilation and discussion of the various other  $XYZ$ -states can be found in refs. [43, 44].

## 2. Theoretical framework

In this chapter we will give the basic concepts and tools used to describe and calculate Green functions and bound-states in a non-perturbative framework. First we will introduce the Lagrangian of quantum chromodynamics (QCD) and provide a glimpse of effective action techniques to derive the equation of motions (EOM). Then we will introduce two-body and four-body bound-state equations. In the last part, we discuss the details of the truncation and the results for the quark-propagator.

### 2.1. Green functions and the generating functional

The starting point of quantum field theory (QFT) is the generating functional in the path integral formulation, see the textbooks [45, 46] for a pedagogical introduction. The generating functional in euclidean space time  $Z_E$  can be written in a shorthand notation as

$$Z_E[J] = \int \mathcal{D}[\Phi] \exp(-S[\Phi] + \langle J, \Phi \rangle). \quad (2.1.1)$$

Here the super field  $\Phi$  includes all elementary particles of the theory. In QCD these fields are quarks ( $\Psi, \bar{\Psi}$ ), gluons ( $A^{a,\mu}$ ) and ghosts ( $c^a, \bar{c}^a$ ). In the same way  $J = \{\eta, \bar{\eta}, j^{a,\mu}, \sigma^a, \bar{\sigma}^a\}$  is a super source of the field  $\Phi$ . The scalar product  $\langle J, \Phi \rangle$  is understood as integration  $\int dx J(x)\Phi(x)$  over the space time point  $x \in \mathbb{R}^4$  and summation over all other quantum numbers as colour and flavour. Whenever understandable from the context, the brackets will be omitted and we write  $J\Phi$ . The path integration measure  $\mathcal{D}$  is the usual integration over all fields at all space times:

$$\int \mathcal{D}[\Phi] = \lim_{N \rightarrow \infty} \int \prod_{i \in N} d\Phi(x_i). \quad (2.1.2)$$

Besides the generating functional  $Z[J]$ , the generating functional of the connected Green functions plays an important role. It is defined as

$$W[J] = \ln Z[J]. \quad (2.1.3)$$

Physical observables can be extracted from the correlation functions of the theory also called Green functions. These Green functions are defined as vacuum expectation values of the time ordered product of the various fields. Abbreviating a product of operators  $\mathcal{O}$  as  $\mathcal{P}[\mathcal{O}]$ , the Green function of  $n$  fields can be written as

$$\begin{aligned}
G_{n,\mathcal{P}[\Phi]}(x_1, \dots, x_n) &:= \langle 0|T[\mathcal{P}[\Phi(x)]]|0\rangle = \\
&= \frac{\int \mathcal{D}[\Phi] \Phi(x_1) \dots \Phi_n(x_n) \exp(-S[\Phi])}{\int \mathcal{D}\Phi \exp(-S[\Phi])} \\
&= \frac{1}{Z[0]} \mathcal{P} \left[ \frac{\delta}{\delta J} \right]_{J=0} Z[J] \\
&=: \langle \mathcal{P}[\Phi(x)] \rangle_{J=0}, \tag{2.1.4}
\end{aligned}$$

with  $\delta/\delta J$  the functional derivative in respect of the various sources.

To calculate the Green functions we follow a functional approach which establishes relations between *all* Green functions present in the theory and truncates the ensuing tower of equations to a tractable form.

## 2.2. The QCD-Lagrangian

In order to utilize the generating functional, we need the Lagrangian of the investigated theory. The euclidean QCD Lagrangian reads in short hand notation

$$\mathcal{L}[\Psi, \bar{\Psi}, A] = \bar{\psi}(\not{D} + m)\Psi + \frac{1}{4}F^{a,\mu\nu}F^{a,\mu\nu}, \tag{2.2.1}$$

Here  $\not{D} = (\partial^\mu - igA^{a,\mu}t^a)\gamma^\mu$  denotes the covariant derivative acting on the quark spinor  $\Psi$ ,  $F^{a,\mu\nu}$  is the field tensor

$$F^{a,\mu\nu} = \partial^\mu A^{a,\nu} - \partial^\nu A^{a,\mu} + gf^{abc}A^{b,\mu}A^{c,\nu} \tag{2.2.2}$$

and  $A^{a,\mu}$  is the gauge field of the gluon. The generators  $t^a$  of the Lie algebra  $su(3)$  in the fundamental representation can be written in terms of the Gell-Mann matrices  $t^a = \frac{\lambda^a}{2}$ . The algebra is given by the Lie bracket  $[t^a, t^b] = if^{abc}t^c$  and the total antisymmetric structure constants  $f^{abc}$ . The coupling is denoted by  $g$ . The Lie-bracket in the field tensor introduces quartic and cubic self-interactions of the gauge-field, rendering the theory non-abelian and leading to phenomena as anti-screening which are absent in an abelian theory such as quantum electrodynamic (QED).

In order to have a uniquely defined theory, the gauge degree of freedom has to be fixed. This can be done by the standard Fadeev-Popov mechanism [47] that introduces auxiliary fields called ghosts ( $c, \bar{c}$ ) that are not part of any physical observable.

Furthermore QCD is a renormalizable theory. This means that the fields and vertices appearing in 2.2.2 develop divergences which can be captured by a finite number of counter-terms and therefore lead to a finite number of renormalization constants.

The full gauge fixed Lagrangian of QCD can now be written as

$$\begin{aligned}
S_{QCD} = & \int_x Z_\Psi \bar{\Psi} (\not{\partial} + Z_m m) \Psi + \frac{Z_A}{2} A^{a,\mu} [-\partial^2 \delta_{\mu\nu} + (1 - \frac{1}{\xi}) \partial^\mu \partial^\nu] A^{a,\nu} + Z_c \bar{c} \partial^2 c - \\
& - i Z_{\Psi A} g \bar{\Psi} \not{A} \Psi + g Z_{cA} f^{abc} \bar{c}^a \partial^\mu (A^{c,\mu} c^b) + \\
& + g Z_{3A} f^{abc} (\partial^\mu A^{a,\nu}) + \frac{g^2}{4} Z_{4A} f^{abc} f^{ade} A^{b,\mu} A^{c,\nu} A^{d,\mu} A^{e,\nu}, \tag{2.2.3}
\end{aligned}$$

with  $Z_\Psi$  the quark wave function,  $Z_m$  the quark mass,  $Z_A$  the gluon wave function,  $Z_c$  the ghost wave function,  $Z_{cA}$  the ghost-gluon vertex,  $Z_{\Psi A}$  the quark-gluon vertex and  $Z_{3/4A}$  the four- and three gluon-vertex renormalization constant. The vertex renormalization constants are defined in such a way that they are the product of the wave function renormalization constants and the charge renormalization constant  $Z_g$ . The last one is necessary because the charge or coupling  $g$  has also to be renormalized. Each constant for each field comes with a power of 1/2. This gives the relations

$$Z_{cA} = Z_g^2 Z_A^2 \quad Z_{\Psi A} = Z_g Z_\Psi Z_A^{1/2} \quad Z_{4A} = z_g^2 Z_A^2 \quad Z_{3A} = Z_g Z_A^{3/2}. \tag{2.2.4}$$

Additionally the renormalization constants are related by the so called Slavnov-Taylor identities (STI) [48, 49] which follow from a residual symmetry after gauge fixing, called Becchi-Rouet-Stora-Tyutin symmetry (BRST)[50]:

$$\frac{Z_{4A}}{Z_{3A}} = \frac{Z_{3A}}{Z_A} = \frac{Z_{cA}}{Z_c} = \frac{Z_{\Psi A}}{Z_\Psi}. \tag{2.2.5}$$

Additionally, we work in Landau gauge ( $\xi = 0$ ) which gives rise to the condition

$$Z_{cA} = 1. \tag{2.2.6}$$

### 2.3. Effective action and Dyson-Schwinger equations

In order to arrive at the equation of motions for the Green functions, we introduce the so called 1PI-effective action. This object can be deduced from the generating functional for the connected Green functions by Legendre transformation:

$$\Gamma[\tilde{\phi}] := W[J] + \int dx J(x) \tilde{\phi}(x) \Rightarrow W[J] = \Gamma[\tilde{\phi}] - \int dx J(x) \tilde{\phi}(x). \tag{2.3.1}$$

Note that the source  $J$  is not set to zero yet. The ‘new’ field  $\tilde{\phi}$  is the so called *averaged* field in the presence of a source  $J$ . This can be seen by expressing  $\tilde{\phi}$  in terms of a derivative in respect of  $J$  and using eq. (2.1.3):

$$\tilde{\phi} = -\frac{\delta W[J]}{\delta J(x)} = \frac{1}{Z[J]} \frac{\delta Z[J]}{\delta J(x)} \stackrel{(2.1.4)}{=} G_{1,\mathcal{P}[\tilde{\phi}]}(x). \tag{2.3.2}$$

To derive the Dyson-Schwinger equations we assume that the generating functional falls off quickly enough for large space-time points:

$$\int \mathcal{D}[\Phi] \frac{\delta}{\delta \Phi} \exp(-S + J\Phi) = \text{Surface} [\exp(-S + J\Phi)] = 0. \tag{2.3.3}$$

We can now perform the derivative on the left hand side in eq. (2.3.3)

$$0 = \int \mathcal{D}[\Phi] \left( -\frac{\delta S}{\delta \Phi} \Big|_{\Phi=\delta/\delta J} + J \right) \exp(-S + J\Phi) = \left( -\frac{\delta S}{\delta \Phi} \Big|_{\Phi=\delta/\delta J} + J \right) Z[J]. \quad (2.3.4)$$

We made use of the fact that  $S$  is polynomial in the fields and  $\Phi = \delta_J \exp(-S + J\Phi)$ . Employing the identities

$$\exp(-W[J]) \frac{\delta}{\delta J} \exp(-W[J]) = \frac{\delta W[J]}{\delta J} + \frac{\delta}{\delta J} \quad (2.3.5)$$

$$\frac{\delta}{\delta J} = \frac{\delta^2 W}{\delta J \delta J} \frac{\delta}{\delta \tilde{\phi}} \quad (2.3.6)$$

one arrives at the master equation of all Dyson-Schwinger (DSE) equations:

$$-\frac{\delta S}{\delta \Phi} \Big|_{\Phi=\tilde{\phi}+\Delta^J \delta/\delta \tilde{\phi}} + \frac{\Gamma}{\delta \tilde{\phi}} = 0 \quad (2.3.7)$$

The object  $\Delta^J$  is in this case the full two-point Green function (Propagator) in presence of a source. To translate this compact notation into equations, one performs the derivative of  $S$ . The resulting equation is the generating DSE for the 1PI Green function  $\delta\Gamma/\delta\tilde{\Phi}$ . By performing derivatives in respect of  $\tilde{\phi}$  one can generate equations for all Green functions, which will depend on each other. This will yield the afore time mentioned infinite tower of coupled integral equations. A detailed algorithm using mathematica to derive the DSEs can be found in ref. [51]. For a general overview of DSEs in hadron physics see also refs. [52, 53]. An very pedagogical introduction to functional methods and DSEs can be found in ref. [54].

The usual procedure to deal with an infinite tower of equations is to truncate them. This is usually done by using ansätze for some Green functions except the ones that are solved self consistently. This ansätze are guided by symmetries that have to be fulfilled and by phenomenological observables and perturbative results that have to be reproduced.

## 2.4. The quark DSE

The quark propagator in momentum space reads:

$$S(p) = \frac{B(p^2, \mu^2) - i\not{p}A(p^2, \mu^2)}{A^2(p^2, \mu^2)p^2 + B^2(p^2, \mu^2)} \quad (2.4.1)$$

Here  $A, B$  are momentum dependent dressing functions and  $\mu$  is the renormalization scale. The Dyson-Schwinger equation for the quark reads in an explicit form:

$$S^{-1}(p, \mu) = Z_\Psi(\Lambda, \mu)(-i\not{p} + M(\Lambda)) + g^2(\Lambda, \mu)Z_{\Psi A}(\Lambda, \mu)C_f \int_0^\Lambda dq D^{\mu\nu}(q, \mu)\Gamma^\mu(p+q, p, \mu)S(p+q, \mu). \quad (2.4.2)$$

The Casimir  $C_f$  stems from the implicit colour trace and evaluates to  $4/3$  for  $SU(3)$ . The objects  $D^{\mu\nu}, \Gamma^\mu$  are the fully dressed gluon propagator and quark-quark-gluon vertex which in principle have their own DSE equations. Their tensor decomposition reads

$$D^{\mu\nu} = \left( \delta^{\mu\nu} - \frac{k^\mu k^\nu}{k^2} \right) \frac{Z(k^2)}{k^2} =: T^{\mu\nu} \frac{Z(k^2)}{k^2}$$

$$\Gamma^\mu(p, k) = \sum_{i=1}^{12} f_i(p, k) T_i^\mu. \quad (2.4.3)$$

and the tensor structure of the vertex can be written as

$$T^\mu \in \{\gamma^\mu, p^\mu, k^\mu\} \otimes \{\mathbb{1}, \not{p}, \not{k}, [\not{p}, \not{k}]\}. \quad (2.4.4)$$

The parameter  $\Lambda$  is the cutoff parameter that renders the divergent integrals finite. To properly renormalize, we use the renormalization conditions

$$A(\mu) = 1 \quad M(\mu) = m_q, \quad (2.4.5)$$

where  $m_q$  is the current mass of the quark at a scale  $\mu$ . In principle, a similar procedure has to be carried out for the vertex and the gluon. We will see in the following chapter that in our model, only the quark is determined dynamically and the gluon and the vertex are treated as given, modeled quantities, and therefore we only have to solve the quark DSE of eq. (2.4.2).

## 2.5. Bound state equations in QCD

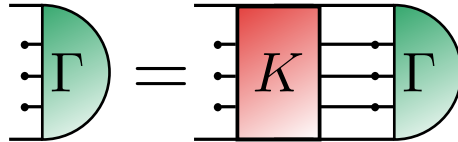


**Figure 2.1.:** General homogeneous n-body BSE. The dots stand for the  $(n-2)$  legs of a n-body equation. Note that the lines between  $K$  and  $\Gamma$  are fully dressed propagators ( $G_0$ ).

The bound-state equation in relativistic theories can be calculated by solving the Bethe-Salpeter equation (BSE) [55]. The general form of an n-body bound-state equation reads

$$\Gamma(P^2) = \lambda(P^2) K G_0 \Gamma(P^2), \quad (2.5.1)$$

where  $P^2$  is the mass of the bound-state,  $K$  is the interaction kernel,  $G_0$  is the product of  $n$  fully dressed propagators, in our case quarks, and  $\Gamma$  is the amplitude of the bound-state. The parameter  $\lambda(P^2)$  is artificial and evaluates to 1, but will play an important role in the numerical treatment of the equations.

The homogeneous bound-state equation, depicted in figure 2.1, can be derived from the scattering equation ( $T$ -matrix equation)

$$T = K' + K G_0 T, \quad (2.5.2)$$

shown in figure 2.2. This T-matrix itself is defined as the connected part of the general  $2n$ -point Green function  $G$ :

$$G = G_0 + G_0 T G_0. \quad (2.5.3)$$

To derive the homogeneous equation we note that the T-matrix can exhibit poles at  $P^2 = -M^2$  where  $P$  is the sum of all external incoming momenta  $p_i$  and  $M$  is the bound state mass.

**Figure 2.2.:** *Upper panel:* General inhomogeneous  $n$ -body scattering equation. *Lower panel:* Decomposition of the T-matrix into a singular part and a regular part. Insertion into the inhomogeneous equation yields the homogeneous equation depicted in figure 2.1.

Following the prescription in ref. [56], a projection on the pole at  $P^2 = -M^2$  via the Cauchy residue theorem yields the homogeneous equation of eq. (2.5.1). This can be easily seen by decomposing the T-matrix into a regular and singular part (lower panel in figure 2.2) and inserting this decomposition into the equation on the upper panel of figure 2.2. Subsequently, identifying the singular part on the left and right hand side of the T-matrix equation yields the homogeneous bound state equation. A solution to this homogeneous equation corresponds to a bound state if  $P^2$  is purely real or a resonance if  $P^2$  develops a imaginary part [57]. All scattering states get eliminated by the projection procedure and cannot spoil the calculation. This distinguishes the DSE/BSE framework from other approaches, such as lattice QCD or sum rule approaches, where both scattering states and bound states appear in the calculation.

The interaction kernel  $K$  is not arbitrary but has a close connection to the effective action. Form the 2PI-effective action, the kernel for the quark-antiquark bound-state can be calculated from the interacting part of the effective action:

$$K_2^{(2)} = -\frac{\delta^2 \Gamma_{int}^{(2)}}{\delta S \delta S}, \quad (2.5.4)$$

see ref. [58] for details. The subscript *int* below  $\Gamma$  denotes the interaction part of the effective action and the superscript denotes the  $n$  of the effective action. The subscript of  $K$  specifies that  $K$  is a two-body kernel. If the effective action is not known then a derivative of the quark-self-energy  $\Sigma$  is also an option to obtain an interaction [59]:

$$\Sigma = \frac{\delta\Gamma_{int}^{(2)}}{\delta S} \quad (2.5.5)$$

$$K_2^{(2)} = -\frac{\Sigma}{\delta S}. \quad (2.5.6)$$

### 2.5.1. Tetraquark bound-state equation

Omitting an explicit derivation of the four-body bound state equation, we refer to refs. [60, 61, 62, 63] for the computational details and will present the final result only.

The general four-body interaction kernel  $K$  has the following form

$$\begin{aligned} K = & K_{12}S_3^{-1}S_4^{-1} + K_{34}S_1^{-1}S_2^{-1} - K_{12}K_{34} + K_{13}S_2^{-1}S_4^{-1} + K_{24}S_1^{-1}S_3^{-1} - K_{13}K_{24} \\ & + K_{14}S_2^{-1}S_3^{-1} + K_{23}S_1^{-1}S_4^{-1} - K_{14}K_{23} \\ & + K_{123}S_4^{-1} + K_{124}S_3^{-1} + K_{234}S_1^{-1} + K_{134}S_2^{-1} + K_{1234}. \end{aligned} \quad (2.5.7)$$

The subscripts represent the legs that the object is attached to. Here the  $K_{ij}$  are the two-body irreducible, the  $K_{ijk}$  are the three-body irreducible and the  $K_{ijkl}$  are the four-body irreducible kernel.  $S^{-1}$  is the fully dressed inverse quark propagator. A more easy to read graphical form is given in figure 2.3.

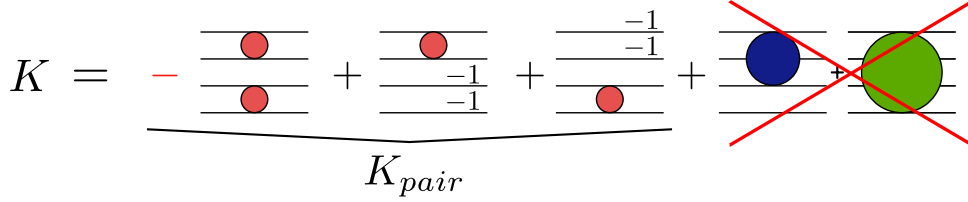


**Figure 2.3.:** Four-body interaction kernel. Three- and four-body forces are neglected. Note the compensation diagram that comes with a minus sign. Permutations are suppressed.

The term  $K_{pair}$  in figure 2.3 contains all irreducible two-body interactions. Because our model does not contain genuine three and four body forces, we will drop them from the equation. A graphical representation of the final equation that is solved in this thesis is shown in figure 2.4. The spirals connecting the quark lines are the effective gluons introduced in chapter 2.9.

It is interesting to note that the four-body kernel has terms that are of the form  $-K_{ij}K_{kl}$ ,  $i \neq j \neq k \neq l$ . These terms are necessary to prevent double counting in the  $T$ -matrix equation. For example, take a simple  $T$ -matrix equation of the form

$$T = K_{12} + K_{34} + K_{12}T + K_{34}T, \quad [K_{12}, K_{34}] = 0. \quad (2.5.8)$$

Because  $K_{12}$  and  $K_{34}$  commute, an iteration of this equation will produce double counting. By adding a term of the form  $-K_{12}K_{34}$ , called compensation term, the double counting can be removed order by order.

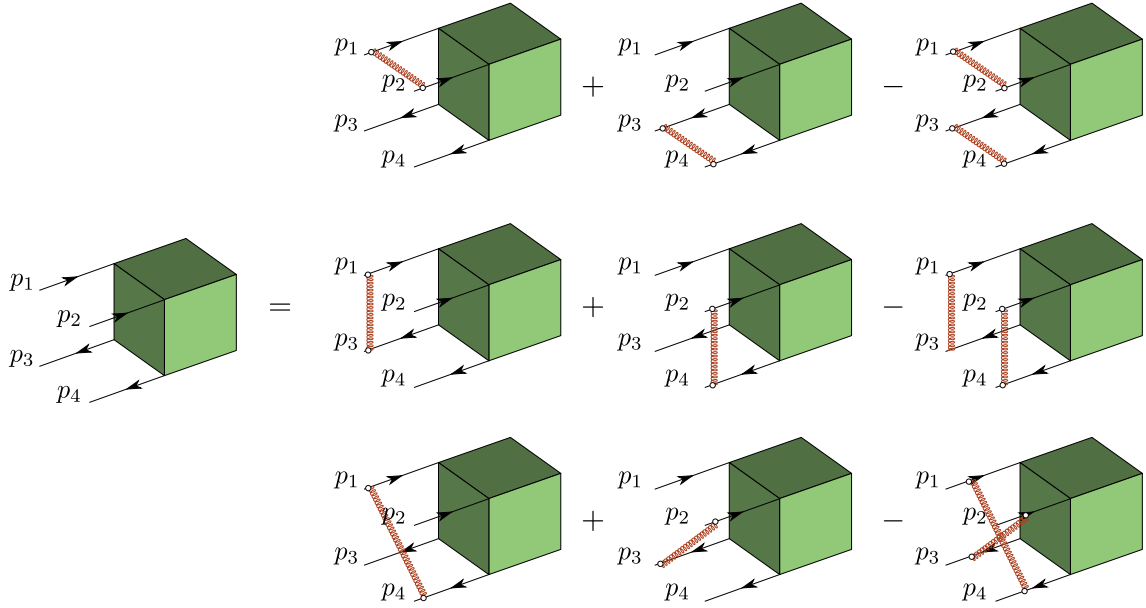


**Figure 2.4.:** Tetraquark BSE in the rainbow ladder truncation.

We want to make an additional comment concerning the derivation of the tetraquark bound state equation from an effective action. In ref. [64] a four-body BSE is derived for a  $\Phi^4$ -theory starting from a five-loop 4PI effective action. The resulting BSE features structurally similar compensation terms than the ones given in eq. (2.5.7) and additionally contains expressions that mix the four-body with the two-body bound states. So in principle, a mixing between tetraquarks, ordinary  $\bar{q}q$  mesons and glueballs can be derived in a canonical way with a suitable loop-truncated 4PI (or higher) effective action. Well beyond the scope of this work, such an approach points the direction of how to include mixing of the different states in future works. A similar discussion of how to mix glueballs and  $\bar{q}q$  mesons can already found in ref. [65].

## 2.6. Normalization of the homogeneous BSE

As in any eigenvalue problem, the normalization, or better the phase of the BSE-eigenvector, is not fixed and one needs an additional condition to also fix the normalization. In the case of the homogeneous BSE, the normalization of the eigenvectors can be fixed by the condition [66]

$$\left( \frac{d \ln(\lambda(P^2))}{dP^2} \right)^{-1} \Big|_{P^2=-M^2} \stackrel{!}{=} \bar{\Gamma} G_0 \Gamma \quad (2.6.1)$$

Here  $\lambda$  is the eigenvalue (curve) of the bound-state problem. The object  $\bar{\Gamma}$  represents the charge conjugated amplitude. The product on the right side is understood as integral over all relative momenta and sum over all colour and flavour indices. This normalization condition holds for any BSE, regardless of the number of particles.

## 2.7. Solving strategies - Quark-DSE

In order to solve the Quark DSE, one can directly start with eq. (2.4.2). After projection on the Dirac structures  $\mathbb{1}$  and  $\not{p}$ , the equation can be solved by standard non-linear solvers. In the case of the Quark-DSE even a naive fixed point iteration is sufficient to obtain a solution. Renormalization is achieved by simultaneously solving eq. (2.4.5). For later application to the BSE, the quarks have to be continued into the complex plane. The reason for the complex continuation is caused by the momentum routing in the BSEs. The total momentum  $P$  reads in the rest frame of the bound state

$$P = (0, 0, 0, iM), \quad (2.7.1)$$

with  $M$  the mass of the bound state. Generically, the momentum that flows through a quark in a BSE reads

$$p_q = p + P \quad (2.7.2)$$

with  $p$  a real, euclidean vector. Upon squaring  $p_q^2$  becomes complex, necessitating a complex continuation of the quark propagator which has to be evaluated at  $p_q^2$ . As can be seen in figure 3.2 and eq. (3.2.3), in the case of the tetraquark there are three relative momenta flowing through each quark line. This will change the momentum routing compared to eq. (2.7.2), but it will be still necessary to know the quark propagator in the complex plane.

To perform the complex continuation we follow a technique first used in the context of bound states in ref. [67], based on the method of ref. [68]. The key idea is a momentum routing for the DSE with the external momentum  $p$  flowing through the quark, as shown explicitly in eq. (2.4.2). After squaring, the momentum  $p_q$  at which the quark inside the self energy is evaluated, reads

$$p_q^2 = p^2 + q^2 + 2p \cdot q, \quad (2.7.3)$$

where the momentum  $q$  denotes the loop momentum. For fixed  $p$ , the square  $p_q^2$  constitutes a parabolic shaped object. It can be shown that for all  $p^2$  that itself lay on a (closed) parabola  $\mathcal{C}$ , parametrized as

$$p^2 = x - \frac{1}{4}M^2 \pm iM\sqrt{x} \quad x \in \{0, \Lambda^2 + \frac{1}{4}M^2\}, \quad (2.7.4)$$

the momenta  $p_q^2$  lay inside this parabola if  $Re(p_q^2) < \Lambda^2 + \frac{1}{4}M^2 =: \tilde{\Lambda}^2$ . Here  $M$  parametrizes the apex of the parabola and  $\Lambda$  is the cutoff that was used to regularize the quark self energy. The parabola is closed by connecting the two branches at  $x = \tilde{\Lambda}^2$  with a vertical line. Defining the dressing function on such a contour makes it possible to use Cauchy's integral theorem

$$f(p^2) = \frac{1}{2\pi i} \oint_C \frac{f(q^2)}{q^2 - p^2} dq^2, \quad (2.7.5)$$

to determine the quark dressing function on the inside of the closed parabola  $\mathcal{C}$ .

By picking appropriate weights  $w_j$  and nodes  $p_j^2$  that correspond to a quadrature along the contour  $\mathcal{C}$ , the formula

$$f(p^2) = \frac{\sum_j \frac{w_j f(q_j^2)}{q_j^2 - p^2}}{\sum_j \frac{w_j}{q_j^2 - p^2}}, \quad (2.7.6)$$

is the discretized version of the Cauchy representation in eq. (2.7.5). The most important point in this representation is the denominator, which evaluates to  $2\pi i$ . Writing the denominator in this elaborate form has the advantage that numerical errors that occur for interpolations close to the nodes  $q_j^2$  cancel out [68]. This method is particularly valuable when dealing with vertex models that depend explicitly on the quark, as is the case in the second part of this work. In this case one cannot solve the DSE in the complex plane by continuing the gluon instead of the quark and one has to use a complex continuation of the quark dressing function.

As a side remark, we mention that this method to represent a function in the complex plane is closely connected to the barycentric interpolation formulas on the real line, see refs. [69, 70, 71]. Throughout this work we used these barycentric interpolation rules on the real line to interpolate the dressing functions of the tetraquarks.

In the Maris-Tandy model, the quark propagator exhibits complex poles [72] which is, corresponding to ref. [73], consistent with the confinement of quarks. The parameter  $M$  is chosen such that the poles are outside of the contour. The apex of the parabola ( $\frac{1}{4}M^2$ ) restricts the calculation of the BSE to masses below  $M$ , at least for the two-body BSE. In the four-body BSE we can go up to  $2M$ . In principle this restriction can be lifted by a proper treatment of the poles and the use of contour deformation techniques, see ref. [74], but such a treatment is technically involved and demands an analytical continuation of the bound state amplitude itself which is beyond the scope of this work.

The quark will be probed outside of the contour on the right side of the parabola because the parabola is closed at  $x = \tilde{\Lambda}^2$ . In principle one should extrapolate the dressing functions beyond the contour. To avoid an explicit numeric extrapolation, we interpolate

$$\sigma_s = \frac{B(p^2)}{A^2(p^2)p^2 + B(p^2)} \quad \sigma_v = \frac{A(p^2)}{A^2(p^2)p^2 + B(p^2)} \quad (2.7.7)$$

instead of  $A$  and  $B$ . These functions decay with  $1/p^2$ , so that we extrapolate them by 0 whenever probed outside of the contour on the *right*-side of the parabola, see figure 2.5. Because this extrapolation happens at large momenta, namely whenever  $Re(p_q^2) > \tilde{\Lambda}^2 \approx 10^4 GeV^2$  holds, such an extrapolation introduces only a tiny error. We tested this by using different extrapolation methods and found the results to change only on the sub-promille level.

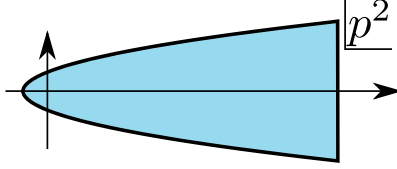


**Figure 2.5.:** Contour of Cauchy interpolation. The shaded area is the region that can be interpolated by the Cauchy-formula. The vertical line on the right side of the parabola closes the contour.

## 2.8. Solving strategies - BSE

The solution strategy for the BSE is straightforward. The homogeneous bound state equation of eq. (2.5.1) reads

$$\Gamma(P^2) = \lambda(P^2)KG_0\Gamma(P^2), . \quad (2.8.1)$$

After discretized the amplitude by choosing a suitable functional basis, the amplitude can be indexed by the super index

$$I = (p_i, T_i, C_i, F_i). \quad (2.8.2)$$

Here  $p_i$  indexes the functional basis,  $T_i$  indexes the tensor structures,  $C_i$  is doing the same for the colour and  $F_i$  for the flavour structure. The multiplication in eq (2.8.1) involves an integral which is a linear operation and can also be discretized, for example by a Gauss-Legendre quadrature rule. Thus the whole equation can be written as

$$\Gamma_I(P^2) = K_{I,J}\Gamma_J(P^2), \quad (2.8.3)$$

which is now an ordinary eigenvalue equation. Because this matrices are sparse but can get large for the tetraquark (beyond  $10^6 \times 10^6$ ) we use the library SLEPc [75], which facilitates matrix free algorithms. We strongly advise the use of an external library for the solution for standard eigenvalue problems because of the plethora of well implemented methods and the overall much better performance and usability compared to hand-crafted methods.

To determine the mass and the amplitude we solve eq. 2.8.3 for different  $P^2$  until the largest eigenvalue becomes 1. The corresponding  $P^2$  is identified with the mass and the corresponding eigenvector with the amplitude of the tetraquark bound state.

**Extrapolation** For the case that there is a threshold, caused by a pion or quark pole, that prevents us from directly solving the BSE at some  $P^2$ , we linearly extrapolate the function

$$f_\lambda(P^2) := \frac{1}{\lambda(P^2)} - 1, \quad (2.8.4)$$

and search for the zero crossing of the extrapolant. The function  $\lambda$  is the eigenvalue curve *up to* the threshold. The justification for this method is given in [76]. Therein the author shows for a two-body bound-state equation, that close to pole the following relation holds:

$$f_\lambda(P^2) \approx (P^2 - M^2), \quad (2.8.5)$$



in figure 2.6. The guiding principle for the Maris-Tandy interaction are the recovery of the perturbative running coupling, the provision of ‘enough’ strength in the mid-momentum range to facilitate dynamical chiral symmetry breaking (DCSB) and multiplicative renormalizability. This is achieved by the following expression [77]:

$$k^2 G(k^2) := \frac{g^2 Z(k^2) \Gamma_{MT}(k^2)}{Z_c Z_\Psi} = 4\pi \left( \frac{\pi}{\omega^6} D k^2 \exp(-k^2/\omega^2) + \frac{2\pi\gamma_m(1 - \exp(-k^2/(4m_t^2)))}{\ln(e^2 - 1 + (1 + k^2/\Lambda_{QCD}^2))} \right). \quad (2.9.1)$$

The parameters read:  $m_t = 0.5 \text{ GeV}$ ,  $\gamma_m = 12/(33 - 2N_f)$ ,  $\Lambda_{QCD} = 0.234 \text{ GeV}$ ,  $\omega = 0.4 \text{ GeV}$ ,  $D = 0.93 \text{ GeV}^2$ . The second term of the interaction provides logarithmic running for large momenta  $k^2 \gg \Lambda_{QCD}^2$

$$g^2 Z(k^2) \Gamma^\mu(k^2) \longrightarrow 4\pi \frac{\pi\gamma_m}{\ln(k^2/\Lambda_{QCD}^2)} = 4\pi\alpha_s(k^2) \quad (2.9.2)$$

with  $\alpha_s$  the strong running coupling. The parameter  $\gamma_m$  is the anomalous dimension of the quark mass, important in the perturbative regime, where the mass runs as

$$m(k^2) = \left( \frac{\alpha_s(k^2)}{\alpha_s(\mu^2)} \right)^{\gamma_m} m(\mu) \quad (2.9.3)$$

for some scale  $\mu$  [78, 79].

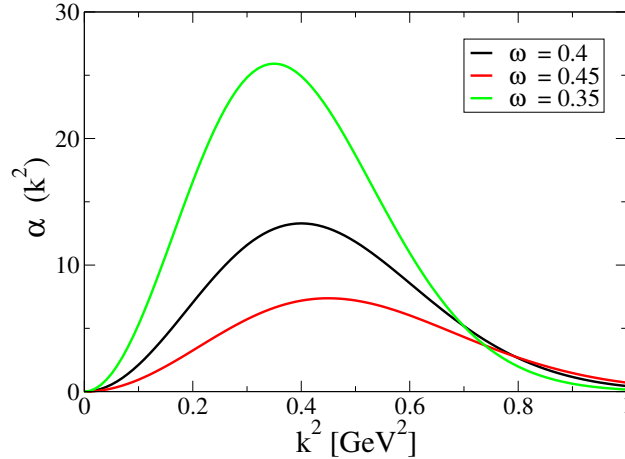


**Figure 2.7.:** Maris-Tandy coupling, eq. (2.9.1), for different  $\omega$  values. The enhancement in the mid-momentum regime is responsible for dynamical chiral symmetry breaking. The shape of the enhancement has a strong influence on the excited meson spectrum, but is not so important for ground state properties. The parameters  $D$  and  $\omega$  are fixed to reproduce the pion decay constant  $f_\pi = 0.131 \text{ GeV}$  and the pion mass  $m_\pi = 0.138 \text{ GeV}$ .

The functional form of the Maris-Tandy interaction is shown in figure 2.7. The shape is strongly dependent on  $\omega$ , but the influence of  $\omega$  on ground state properties is small [67, 80]. The interaction vanishes in the infrared. Besides a numerical simplification, the influence of the deep infrared properties of the interaction on meson observables is mild

[81]. The renormalization constants in front of eq. (2.9.1) are necessary to give the correct renormalization properties. Starting from the identities in eq. (2.2.4), one finds

$$Z_{\Psi A} = Z_{\Psi} \frac{1}{Z_{\Psi} Z_c}. \quad (2.9.4)$$

This property has two consequences. First, we immediately see that the self-energy behaves as  $Z_{\psi}^2$ , and second, the expression on the left hand side in eq. (2.9.1) is seen to be renormalization group independent, by using eq. (2.9.4) and eq. (2.2.4):

$$\frac{g^2 Z(k^2) \Gamma_{MT}(k^2)}{Z_c Z_{\Psi}} \approx \frac{1/Z_g^2 Z/Z_A Z_{\Psi A}}{Z_c Z_{\Psi}} = 1. \quad (2.9.5)$$

This is the reason for the ghost renormalization in eq. (2.9.1), which by itself is not obtainable in this model, but necessary to preserve renormalization group properties. Inserting the Maris-Tandy of eq. (2.9.1) into eq. (2.4.2), one arrives at the following form of the DSE

$$S^{-1}(p, \mu) = Z_{\Psi}(\Lambda, \mu)(-i\not{p} + M(\Lambda)) + Z_{\Psi}^2 C_f \int_0^{\Lambda} dq T^{\mu\nu}(q) G(q^2) \gamma^{\mu} S(p+q, \mu). \quad (2.9.6)$$

We use a typical scale  $\mu$  of  $19 \text{ GeV}$  [77] and a  $\Lambda^2 = 10^4 \text{ GeV}^2$ . With the renormalization conditions

$$A(\mu) = 1 \quad M(\mu) = m_q, \quad (2.9.7)$$

and the complex continuation in chapter 2.7, the quark can be calculated self consistently.

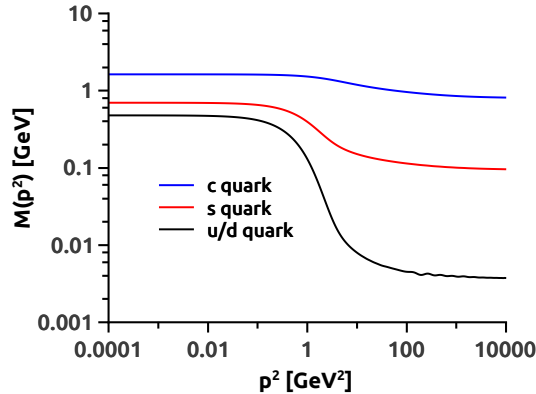


**Figure 2.8.:** The quark mass functions  $M(p^2)$  in the Maris-Tandy model. The lines represent (from top to bottom)  $c$ ,  $s$ ,  $u/d$  quarks respectively.

The solution for the quark mass functions  $M(p^2)$  can be seen in figure 2.8. The dominant feature is the dynamical chiral symmetry breaking, visible by the acquisition of mass in the infrared. The  $UV$ -behavior is logarithmic, as could be expected from the logarithmic tail in eq. (2.9.1).

Using a different momentum routing than in eq. (2.9.6), by sending the complex momentum  $p$  through the gluon, the quark propagator can also be calculated in the whole

$q$	$m_q$	condition
$u$	$0.00405 \text{ GeV}$	$m_\pi = 0.138 \text{ GeV}$
$s$	$0.0105 \text{ GeV}$	$m_K = 0.495 \text{ GeV}$
$c$	$0.89 \text{ GeV}$	$\eta_c = 2.95 \text{ GeV}$

**Table 2.1.:** Quark masses used in this work. The masses are fixed to reproduce the mesons given in the table. The Maris-Tandy parameters ( $D, \omega$ ) are fixed to reproduce the pion mass and decay constant.

complex plane. This continuation leads to problems further away from the real axis, because the exponential in the Maris-Tandy coupling diverges and the logarithms introduce spurious cuts for complex momenta, see eq. (2.9.1). Nonetheless this momentum routing can be used to investigate the analytical structure of the quark not too far away from the real axis.

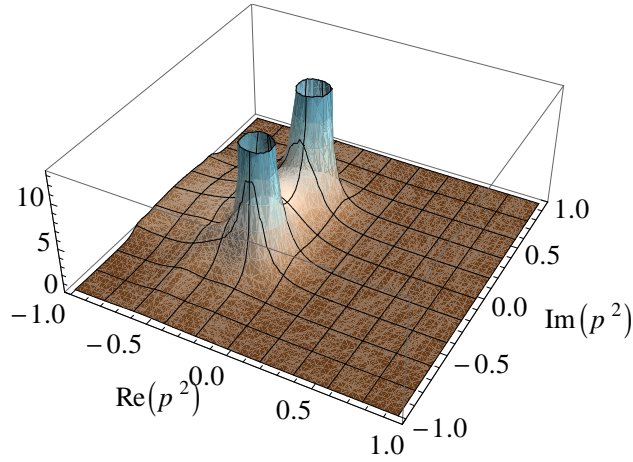


**Figure 2.9.:** The absolute value of the quark dressing function  $\sigma_s$  in the complex plane of  $p^2$ .

In figure 2.9 the result for the absolute value of the scalar dressing function  $\sigma_s$  can be seen. The two poles emerging in the complex plane are responsible for DCSB by causing the raise of the mass function on the real axis. A thorough review of the analytical properties of quarks within different vertex models can be found in ref. [72].

### 2.9.2. Rainbow ladder truncation - Two-body kernel

The kernel of the two-body bound-state is derived via a functional derivative of the quark self-energy by ‘cutting’ a quark line, see figure 2.6. Performing such a derivative, the expression of the two-body kernel in the Maris-Tandy reads

$$K_{ab,cd}(q) = G(q^2) \left( \frac{\lambda^i}{2} \right)_{AB} \left( \frac{\lambda^i}{2} \right)_{CD} (i\gamma_{cd}^\mu) T^{\mu\nu} (i\gamma_{ab}^\nu). \quad (2.9.8)$$

Here we distinguish between Dirac indices denoted by  $a, b, c, d$  and colour indices  $A, B, C, D$ ; The momentum  $q$  is the momentum of the gluon.

Because the kernel is derived by taking a functional derivative of the self-energy in respect of the quark, the axial Ward-Takahashi identity (AXWTI)[82] is preserved [83]. The AXWTI relates the interaction kernel to the quark self-energy, stressing the close connection of the kernel and the quark self-energy. The diagrammatic and analytical form of the AXWTI reads [84]:

$$\gamma_5 \Sigma(-p_-) + \Sigma(p_+) \gamma_5 = - \int K(q) (\gamma_5 S(-q_-) + S(q_+) \gamma_5), \quad (2.9.9)$$

$$\text{Diagrammatic representation of the AXWTI.} \quad (2.9.10)$$

The subscripts  $+$ ,  $-$  on the momenta are to be understood as addition or subtraction of  $\frac{1}{2}P$  with  $P$  the momentum of the bound-state.

This rather simple model has been successfully applied to calculate various hadron observables. Light quark meson masses with  $J$  up to three [78, 85, 77, 67], charmonium and bottomonium spectra [85, 86, 87], strong decays [88],  $\pi\pi\gamma$  transition form factors [89], weak decays [89] and scattering lengths [90]. The same model was also applied to the nucleon properties, as the nucleon spectrum [91, 92], the masses of the  $\Omega$  and  $\Delta$  [93], the octet and decuplet masses of the nucleon [94], the electromagnetic form factors of the baryons [95, 96] and nucleon-compton scattering [97].

Besides the physical  $q\bar{q}$  mesons, the Maris-Tandy interaction also produces  $qq$  bound-states in the colour triplet channel (diquarks). These unphysical bound-states are associated with truncation artifacts that are resolved by inclusion of beyond rainbow-ladder corrections, namely the crossed ladder contributions, as the investigation of the authors in ref. [98] has shown. Besides the unphysical nature of the diquarks, their emergence as bound-states made it possible to include diquarks explicitly in a two-body approach [99], a previous work of the author of this thesis.

**Beyond Rainbow ladder - comments** At this point we want to make a few comments regarding beyond simple rainbow-ladder truncations.

Normally, any approach beyond rainbow ladder dresses the quark-quark-gluon vertex in some way.

One approach is, to directly use a vertex model for the quark DSE. In this case, the corresponding effective action is unknown. If one uses such an explicit model for the vertex, there is one caveat. The vertex (model) *has* to transform in the same way as the quark. Especially it has to chirally transform in the same way, see ref. [59]. Violating the transformation properties will break the Axial-Ward-Takahashi identity (AXWTI) and therefore never yield a light pion. This is especially important if the vertex model depends explicitly on the quark. The collaborators in ref. [100] resolved the problem by solving the quark DSE and some vertex equations with the AXWTI as explicit constraint. The

authors in ref. [1] solved the problem for a related vertex model, based on ref. [59], by employing a vertex that already fulfills all transformation properties. The details and all results of the latter approach are provided in the second part of this work. In yet another approach in refs. [101, 102, 103], certain diagrammatic unquenching effects for the vertex were taken into account in an AXWTI preserving fashion.

A different way to tackle the problem would start with a truncated effective action and derive all DSEs and BSE-kernels from this effective action. All global symmetries would then be fulfilled by construction [58]. Some details connected with this idea and how to use them in the meson and baryon sector are outlined in [104].

### 3. Constructing a symmetric amplitude for tetraquarks

The tetraquark amplitude is subject to various symmetries. Two of them, the Pauli principle and charge conjugation, are manifest as permutations of the quark- and antiquark-legs of the tetraquark amplitude and their corresponding quantum numbers. The underlying symmetry group for these permutations is the  $S_4$  permutation group, see ref. [105] for a concise overview of the  $S_4$  symmetry. It is therefore useful to formulate the problem and more precisely the amplitude, in terms of objects that respect this symmetry. The tetraquark amplitude consists of:

- Dirac matrices, called the spin-part.
- Lorentz-vectors, which form the orbital-angular-momentum part.
- Scalar dressing functions, dependent on all Lorentz invariant scalars that are present in the tetraquark.
- A colour-indexed object, which is a singlet.
- A flavour-indexed object.

Each part has to transform in such a way that the entire amplitude respects the desired permutation symmetries. When constructing the colour and flavour part of the amplitude in the corresponding sections, we will see that the  $SU(3)$ -multiplets already transform symmetric or antisymmetric under the relevant  $S_4$ -permutations. Therefore the symmetry of the spin-orbit part and the scalar dressing functions is fixed. In order to construct these parts we will heavily use the tools and notations developed in ref. [106] which will soon be published. Parts of the tools can already be found in ref. [107]. First we will give a short summary of the key-points and tools of ref. [106] and then use them in the subsequent sections to construct the necessary parts of the amplitude.

#### 3.1. General considerations

The  $S_4$  symmetry group has 24 members that can be grouped into two singlets ( $\mathcal{S}, \mathcal{A}$ ), a doublet  $\mathcal{D}_j$  and two triplets ( $\mathcal{T}_i^+, \mathcal{T}_i^-, i \in \{1, 2, 3\}$ ). The corresponding Young-diagrams read:

The doublet  $\mathcal{D}_j$  with  $j \in \{1, 2\}$  and the two triplets ( $\mathcal{T}_i^+, \mathcal{T}_i^-$ ) with  $i \in \{1, 2, 3\}$  transform under different irreducible representations. The singlets fall into two classes.  $\mathcal{S}$  is totally

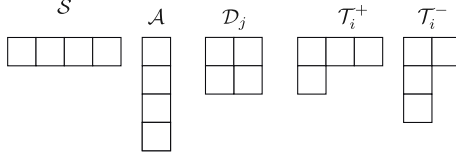


**Figure 3.1.:** Young diagrams of the  $S_4$  permutation group.

symmetric and  $\mathcal{A}$  is totally antisymmetric. Given the elements of a set that the  $S_4$ -group acts on, the corresponding multiplets can be constructed following the construction principals in ref. [106]. To close this brief overview we provide the irreducible representation matrices and there action on the multiplets. The transpositions, or permutations, of two indices will be denoted as  $P_{ij}$ . Usually the transpositions  $P_{12}$ ,  $P_{23}$ ,  $P_{34}$  are used to span the  $S_4$  group. Any other element of the group can be represented by chaining these three group elements.

$$M = \begin{pmatrix} -1 & 0 \\ 0 & 1 \end{pmatrix} \quad M' = \frac{1}{2} \begin{pmatrix} 1 & -\sqrt{3} \\ \sqrt{3} & 1 \end{pmatrix} \quad (3.1.1)$$

$$H = \begin{pmatrix} 1 & 0 & 0 \\ 0 & 1 & 0 \\ 0 & 0 & 1 \end{pmatrix} \quad H' = \frac{1}{2} \begin{pmatrix} 1 & 0 & 0 \\ 0 & -1 & -\sqrt{3} \\ 0 & -\sqrt{3} & 1 \end{pmatrix} \quad H'' = \frac{1}{2} \begin{pmatrix} -1 & -\sqrt{8} & 0 \\ -\sqrt{8} & 1 & 0 \\ 0 & 0 & 3 \end{pmatrix} \quad (3.1.2)$$

$$\begin{aligned} P_{12}\mathcal{D}_i &= M\mathcal{D}_i & P_{12}\mathcal{T}_i^\pm &= \pm H\mathcal{T}_i^\pm \\ P_{23}\mathcal{D}_i &= M'\mathcal{D}_i & P_{23}\mathcal{T}_i^\pm &= \pm H'\mathcal{T}_i^\pm \\ P_{34}\mathcal{D}_i &= M\mathcal{D}_i & P_{34}\mathcal{T}_i^\pm &= \pm H''\mathcal{T}_i^\pm \end{aligned} \quad (3.1.3)$$

## 3.2. Phase space

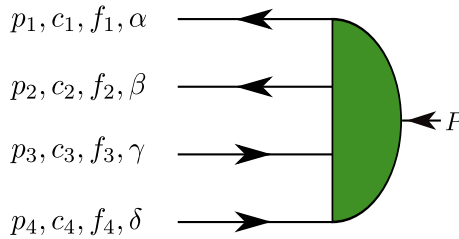


**Figure 3.2.:** Tetraquark amplitude. The  $p_i$  represent the momenta, the  $c_i$  and  $f_i$  are colour and flavour indices respectively and the Greek indices stand for Dirac-indices. The black arrow specifies the direction of the spin line.

Equipped with construction principals of  $S_4$ , we will start to investigate the phase space. We chose to define the relative momenta  $(p, q, k)$  and the total momenta  $(P)$  in the following way:

$$\begin{aligned}
p &= \frac{(p_1 + p_4) - (p_2 + p_3)}{2} \\
q &= \frac{(p_1 + p_3) - (p_2 + p_4)}{2} \\
k &= \frac{(p_1 + p_2) - (p_3 + p_4)}{2} \\
P &= p_1 + p_2 + p_3 + p_4.
\end{aligned} \tag{3.2.1}$$

The inversion of the momenta reads:

$$\begin{aligned}
p_1 &= \frac{-p + q + k}{2} + \frac{1}{4}P \\
p_2 &= \frac{p - q + k}{2} + \frac{1}{4}P \\
p_3 &= \frac{p + q - k}{2} + \frac{1}{4}P \\
p_4 &= \frac{-p - q - k}{2} + \frac{1}{4}P.
\end{aligned} \tag{3.2.2}$$

For future reference the momenta  $p_1, p_2, p_3, p_4$  are attached to the tetraquark amplitude as depicted in figure 3.2. We want to point out that the relative momenta  $p, q, k$  contain the total momenta of the sub-cluster. With sub-cluster we mean any combination of two quark lines. The physical implication of the appearance of this sub-cluster will be investigated in chapter 4.

Because it will play an important role later on, we also give the permutation properties of the relative momenta and their scalar products, see table 3.1. Additionally we provide some notation and definitions concerning the momenta.

	$P_{12}$	$P_{34}$	$P_{13}$	$P_{24}$	$P_{14}$	$P_{23}$	$P_{12,34}$	$P_{13,24}$	$P_{14,23}$
p	q	-q	k	-k	p	p	-p	-p	p
q	p	-p	q	q	-k	k	-q	q	-q
k	k	k	p	-p	-q	q	k	-k	-k
$p \cdot q$	$p \cdot q$	$p \cdot q$	$q \cdot k$	$-q \cdot k$	$-p \cdot k$	$p \cdot k$	$p \cdot q$	$-p \cdot q$	$-p \cdot q$
$p \cdot k$	$q \cdot k$	$-q \cdot k$	$p \cdot k$	$p \cdot k$	$-p \cdot q$	$p \cdot q$	$-p \cdot k$	$p \cdot k$	$-p \cdot k$
$q \cdot k$	$p \cdot k$	$-p \cdot k$	$p \cdot q$	$-p \cdot q$	$q \cdot k$	$q \cdot k$	$-q \cdot k$	$-q \cdot k$	$q \cdot k$

**Table 3.1.:** Permutation properties of the relative momenta and their scalar products.

**Notation** For the angles we use the notation:

$$\begin{aligned}
\omega_1 &= q \cdot k & \omega_2 &= p \cdot k & \omega_3 &= p \cdot q \\
\eta_1 &= P \cdot p & \eta_2 &= P \cdot q & \eta_3 &= P \cdot k
\end{aligned} \tag{3.2.3}$$

A quantity with a hat denotes that the vector is normalized and a subscript  $T$  that the vector is transversal to  $P$ :

$$\begin{aligned} p_T &= p - (p \cdot P) \frac{P}{P^2} & \omega'_1 &= q_T \cdot k_T \\ q_T &= q - (q \cdot P) \frac{P}{P^2} & \omega'_2 &= p_T \cdot k_T \\ k_T &= k - (k \cdot P) \frac{P}{P^2} & \omega'_3 &= p_T \cdot q_T \end{aligned} \quad (3.2.4)$$

The tetraquark depends on ten independent Lorentz invariants. One of them is the mass of the tetraquark, leaving nine unfixed. The set of Lorentz invariants will be denoted by  $\Omega$ :

$$\Omega = \{k^2, p^2, q^2, \omega_1, \omega_2, \omega_3, \eta_1, \eta_2, \eta_3\}. \quad (3.2.5)$$

For practical calculations we also need the relative momenta expressed via hyper-spherical coordinates:

$$\begin{aligned} P &= \sqrt{P^2} \begin{pmatrix} 0 \\ 0 \\ 0 \\ 1 \end{pmatrix} & k &= \sqrt{k^2} \begin{pmatrix} 0 \\ 0 \\ \bar{c}_3 \\ c_3 \end{pmatrix} \\ p &= \sqrt{p^2} \begin{pmatrix} 0 \\ \bar{c}_1 \bar{z} \\ \bar{c}_1 z \\ c_1 \end{pmatrix} & q &= \sqrt{q^2} \begin{pmatrix} \bar{c}_2 \bar{z}' \sin \alpha \\ \bar{c}_2 \bar{z}' \cos \alpha \\ \bar{c}_2 z' \\ c_2 \end{pmatrix}. \end{aligned} \quad (3.2.6)$$

The radial variables  $k^2, p^2, q^2$  are real and positive and the variables  $c_1, c_2, c_3, z, z', \alpha$  are hyper-spherical angles or their cosines:

$$k^2, p^2, q^2 \in \mathbb{R}_+, \quad \{c_1, c_2, c_3, z, z'\} \in [-1, 1] \quad \alpha \in [0, 2\pi]. \quad (3.2.7)$$

Quantities with a  $\bar{(\cdot)}$  are defined as

$$\bar{(\cdot)} := +\sqrt{1 - (\cdot)^2}, \quad (3.2.8)$$

such that, for example,  $\bar{z} = \sqrt{1 - z^2}$ .

**Phase space multiplets** First we construct the following  $S_4$  triplets:

$$\mathcal{T}_{LV}^+ = \frac{1}{2} \begin{pmatrix} \frac{1}{\sqrt{3}}(p + q + k) \\ \frac{1}{\sqrt{6}}(p + q - 2k) \\ \frac{1}{\sqrt{2}}(q - p) \end{pmatrix} \quad \mathcal{T}_1^+ = \frac{1}{2} \begin{pmatrix} \frac{1}{\sqrt{3}}(\eta_1 + \eta_2 + \eta_3) \\ \frac{1}{\sqrt{6}}(\eta_1 + \eta_2 - 2\eta_3) \\ \frac{1}{\sqrt{2}}(\eta_2 - \eta_1) \end{pmatrix}. \quad (3.2.9)$$

The triplet  $\mathcal{T}_{LV}^+$  still contains Lorentz-vectors whereas the triplet  $\mathcal{T}_1^+$  is build up by Lorentz scalars. By using  $S_4$ -multiplications of appendix A.5, the triplet  $\mathcal{T}_{LV}^+$  can be transformed into a triplet, a doublet and a singlet that contain Lorentz-scalars only:

$$\mathcal{S}_0 := \mathcal{T}_{LV}^+ \cdot \mathcal{T}_{LV}^+ = \frac{p^2 + q^2 + k^2}{4} \quad (3.2.10)$$

$$\mathcal{D}_0 := \mathcal{T}_{LV}^+ * \mathcal{T}_{LV}^+ = \mathcal{S}_0 \begin{pmatrix} a \\ s \end{pmatrix}$$

$$\mathcal{T}_0 := \mathcal{T}_{LV}^+ \vee \mathcal{T}_{LV}^+ = \mathcal{S}_0 \begin{pmatrix} u \\ v \\ w \end{pmatrix}$$

$$\mathcal{T}_1 := \mathcal{T}_1^+ = \sqrt{\mathcal{S}_0 P^2} \begin{pmatrix} u' \\ v' \\ w' \end{pmatrix}.$$

The doublet variables are related to the set  $\Omega$  by,

$$a = \sqrt{3} \frac{q^2 - p^2}{4\mathcal{S}_0}, \quad s = \frac{p^2 + q^2 - 2k^2}{4\mathcal{S}_0}, \quad (3.2.11)$$

the variables in  $\mathcal{T}_0$  read

$$u = -\frac{\omega_1 + \omega_2 + \omega_3}{4\mathcal{S}_0} \quad v = -\sqrt{2} \frac{\omega_1 + \omega_2 - 2\omega_3}{4\mathcal{S}_0} \quad w = \sqrt{6} \frac{\omega_1 - \omega_2}{4\mathcal{S}_0}, \quad (3.2.12)$$

and the variables in  $\mathcal{T}_1$  have a similar form

$$u' = -\frac{\eta_1 + \eta_2 + \eta_3}{\sqrt{12}\sqrt{\mathcal{S}_0 P^2}} \quad v' = -\frac{\eta_1 + \eta_2 - 2\eta_3}{\sqrt{24}\sqrt{\mathcal{S}_0 P^2}} \quad w' = \frac{\eta_1 - \eta_2}{\sqrt{8}\sqrt{\mathcal{S}_0 P^2}}. \quad (3.2.13)$$

In the doublet and the triplets we factored out the singlet  $\mathcal{S}_0$  and  $\sqrt{\mathcal{S}_0 P^2}$  to render these multiplets dimensionless. The only dimensionfull variable is therefore  $\mathcal{S}_0$ . In the following short sections we give more details concerning the properties of the phase-space multiplets.

### 3.2.1. Doublet

Defining the doublet variables as in eq. (3.2.11), the corresponding geometrical object in the  $a - s$  plane is a equilateral triangle with a side of length  $2\sqrt{3}$ , see figure 3.3.

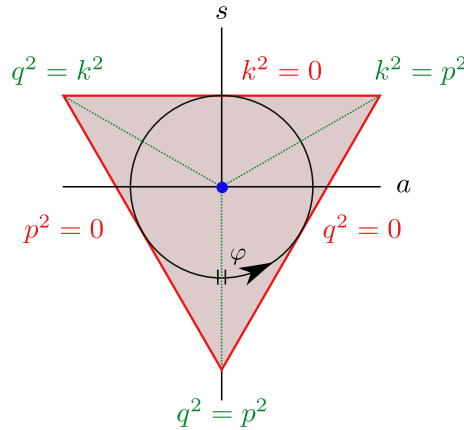


**Figure 3.3.:** Doublet triangle. The shaded area specifies the physical, space-like region.

The corners, the sides and the middle of the triangle correspond to special momentum configurations.

The sides are sampled if the magnitude of one of the relative momenta is zero:

$$p^2 = 0 \quad q^2 = 0 \quad k^2 = 0. \quad (3.2.14)$$

Along the lines connecting the corners with the center of the triangle, the modulus of two of the relative momenta are equal:

$$p^2 = q^2 \quad p^2 = k^2 \quad k^2 = q^2. \quad (3.2.15)$$

Therefore in the center all momenta are equal and have the length

$$p^2 = q^2 = k^2 = \frac{4\mathcal{S}_0}{3}. \quad (3.2.16)$$

In general  $p^2, q^2, k^2 \geq 0$  holds in the inside of the triangle, whereas on the outside of the triangle, some of the momenta are negative.

In order to parametrize this triangle we choose a mapping to a circle

$$\mathcal{D}_0 = \mathcal{S}_0 r(\varphi)_{max} \hat{r} \begin{pmatrix} \sin \varphi \\ -\cos \varphi \end{pmatrix} \quad (3.2.17)$$

$$\varphi \in [0, 2\pi] \quad \hat{r} \in [0, 1] \quad (3.2.18)$$

$$r(\varphi)_{max} = \frac{1}{\sin \left[ \varphi + \frac{\pi}{6} \left( 1 - 4 \lfloor \frac{3\varphi}{2\pi} \rfloor \right) \right]}. \quad (3.2.19)$$

The function  $r_{max}(\varphi)$  represents the boundary of the triangle and is invariant under  $S_4$  transformations. Also the variable  $\hat{r}$  is invariant under  $S_4$  transpositions. The only variable affected by a permutation is therefore the angle  $\varphi$ . In geometrical terms, a  $S_4$  operation rotates the triangle by  $\frac{n \cdot 2\pi}{3}$ ,  $n \in \mathbb{N}$  and therefore exchanges the sides of the triangle.

In anticipation of chapter 4 we draw the attention to the boundary of the triangle that is defined when any of the relative momenta is zero:  $p^2 = 0, q^2 = 0, k^2 = 0$ . For example, if  $P \cdot p = P \cdot q = P \cdot k = 0$ , possible two-body bound-states with mass  $m_{p,q,k}$  can appear on any of the sites at

$$p^2 = -\frac{1}{4}P^2 - m_p^2 \quad q^2 = -\frac{1}{4}P^2 - m_q^2 \quad k^2 = -\frac{1}{4}P^2 - m_k^2, \quad (3.2.20)$$

see eq. (4.1.1) in chapter (4). If  $m_{p,q,k}^2 + \frac{1}{4}P^2$  is sufficiently small, the poles will be close to the boundary that is defined by  $p^2 = 0, q^2 = 0, k^2 = 0$  and cause the amplitude to rise considerably. Additionally, the poles can even appear inside the triangle for large enough tetraquark mass  $M_T$  if  $P^2 + m_{p,q,k}^2 = -M_T^2 + m_{p,q,k}^2 < 0$  holds.

Because the triangle is scaled by  $1/\mathcal{S}_0$ , the two-body poles will come closer to the boundary for larger  $\mathcal{S}_0$ , so that we expect these effects to not show up in the infrared region of  $\mathcal{S}_0$  but for larger values, depending on the mass of the two-body bound-state. A detailed analysis of this feature and its physical and numerical implications on the tetraquark are discussed in chapter 4. Finally we give the connection between  $\hat{r}, \varphi$  and  $p^2, q^2, k^2$ :

$$\begin{aligned}
p^2 &= \frac{4\mathcal{S}_0}{3} \left( 1 + r(\varphi)_{max} \hat{r} \cos \left( \varphi + \frac{2\pi}{3} \right) \right) \\
q^2 &= \frac{4\mathcal{S}_0}{3} \left( 1 + r(\varphi)_{max} \hat{r} \cos \left( \varphi - \frac{2\pi}{3} \right) \right) \\
k^2 &= \frac{4\mathcal{S}_0}{3} (1 + r(\varphi)_{max} \hat{r} \cos(\varphi))
\end{aligned} \tag{3.2.21}$$

### 3.2.2. Triplet $\mathcal{T}_0$

According to ref. [106], the triplet  $\mathcal{T}_0$  has the geometrical form of a tetrahedron, see figure 3.4.

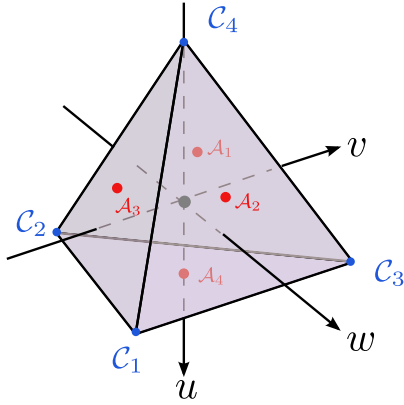


**Figure 3.4.:** Triplet tetrahedron. The shaded area specifies the physical, space-like region.

This can be seen by rewriting the triplet  $\mathcal{T}_0$ :

$$\mathcal{T}_0 = \frac{1}{4} \begin{pmatrix} x_1 + x_2 + x_3 - 3x_4 \\ -\sqrt{2}(x_1 + x_2 - 2x_3) \\ \sqrt{6}(x_1 - x_2) \end{pmatrix} \tag{3.2.22}$$

$$x_i = (p_i - \frac{1}{4}P)^2 \quad i \in \{1, 2, 3, 4\}. \tag{3.2.23}$$

If allowing all space-like  $x_i \geq 0$ , the object is a full tetrahedron. The four corners of the tetrahedron are given by

$$\begin{aligned}
\mathcal{C}_1 &= (1, -\sqrt{2}, \sqrt{6}) & \mathcal{C}_2 &= (1, -\sqrt{2}, -\sqrt{6}) \\
\mathcal{C}_3 &= (1, 2\sqrt{2}, 0) & \mathcal{C}_4 &= (-3, 0, 0)
\end{aligned} \tag{3.2.24}$$

with  $x_i = 4\mathcal{S}_0$  and  $x_{j \neq i} = 0$ . The four faces  $\mathcal{A}_i$  have the property that  $x_i = 0$  holds. In the center of the tetrahedron all  $x_i$  have the same value  $x_i = \mathcal{S}_0$ .

Similar to the doublet triangle, we could expect effects of poles with mass  $m$  located at

$$x_i = -m^2, \tag{3.2.25}$$

influencing the amplitude at the boundary of the tetrahedron for large  $\mathcal{S}_0$ . Because the quark in the Maris-Tandy model has complex-conjugated poles [108] which are far away from the real axis, this effect is suppressed and we expect the overall dependence of the tetraquark on this triplet to be rather weak. Different to the doublet-triangle, these poles stay outside of the tetrahedron for all  $P$  used in our calculation, and so do not produce any threshold effects.

Similar to the doublet we parametrize the triplet in spherical coordinates:

$$\mathcal{T}_0 = \mathcal{S}_0 R(\Omega)_{max} \hat{R} \begin{pmatrix} -\cos \theta \\ \sin \theta \cos \phi \\ -\sin \theta \sin \phi \end{pmatrix} = \mathcal{S}_0 R(\Omega)_{max} \hat{R} \begin{pmatrix} \frac{\cos \alpha_r \cos \Phi_R \bar{z}_R - \sin \alpha_r z_R}{Z_R} \\ \frac{\sin \alpha_r \cos \Phi_R \bar{z}_R + \cos \alpha_r z_R}{Z_R} \\ \frac{\sin \Phi_R}{Z_R} \end{pmatrix}$$

$$Z_R = \sqrt{1 + \frac{1}{2} z_R^2 (1 - \cos 2\Phi_R)} \quad (3.2.26)$$

$$\hat{R} \in [0, 1], \theta \in \{0, \pi\}, \phi \in \{0, 2\pi\} \quad (3.2.27)$$

$$\Phi_R \in \{-\pi, \pi\}, z_R \in \{-1, 1\} \quad (3.2.28)$$

$$\alpha_r = \frac{\cos^{-1}(1/3)}{2} \approx 0.615 \pi. \quad (3.2.29)$$

The angle  $2\alpha_r$  is the ‘tetrahedral angle’ and the variable  $R_{max}$  is similar to  $r_{max}$  in the doublet, providing the mapping from a sphere to a more complicated object.

We use the rather complicated Lorentz-invariants  $\hat{R}, z_R, \Phi_R$  to describe and interpolate the dressing functions. The reason is the nice  $S_4$  transformation property of these variables:

$$P_{12}(\Phi_R) = -\Phi_R \quad (3.2.30)$$

$$P_{34}(\Phi_R) = -\Phi_R + \pi$$

$$P_{34}(z_R) = P_{12}(z_R) = z_R.$$

A grid defined on these variables is much easier to symmetrize than a grid defined on the spherical coordinates  $\theta, \phi$ . The only symmetry transformation that is ‘difficult’, even in this parametrization, is the charge-conjugation operations  $P_{13,24}$  and  $P_{14,23}$  which rotate the triplet variables in a non-trivial way.

In geometrical terms, any  $S_4$ -permutations exchange the faces of the tetrahedron. In future works, this feature could be exploited by replacing the spherical parametrization with a definition on a triangulated sphere, with the vertices defined in such a way that either the vertices or the faces, defined by the vertices, are permuted when performing an  $S_4$  operation. Natural candidates would be the spherical polyhedra of the tetrahedral group and their duals with a spherical barycentric interpolator defined on the vertices [109].

There is another complication present in the triplet variables that is absent in the doublet. In order to fill a complete tetrahedron, the variables  $x_i$  have to be independent. This is not the case because of the condition:

$$\sum_{i=1}^4 x_i = 0. \quad (3.2.31)$$

Geometrically, this restriction can be deduced from the Lorentz-vectors in eq. (3.2.6). The three angular variables  $z, z', \alpha$  are restricted to the interval  $[-1, 1]$ . Setting one of them to the maximal or minimal value and letting the other two vary in the interval  $[-1, 1]$  will define a surface in the three-dimensional space spanned by  $u, v, w$ . We found this surface to be defined by the  $S_4$  invariant condition:

$$\begin{aligned} k^2 p^2 k^2 P^2 &= P^2(p^2 \omega_1^2 + k^2 \omega_3^2 + q^2 \omega_2^2) - 2P^2 \omega_1 \omega_2 \omega_3 \\ &+ (k^2 q^2 \eta_1^2 + k^2 p^2 \eta_2^2 + p^2 q^2 \eta_3^2) \\ &+ 2(\omega_1 \omega_2 \eta_1 \eta_2 + \omega_3 \omega_2 \eta_1 \eta_3 + \omega_2 \omega_3 \eta_2 \eta_3) \\ &- (\omega_1^2 \eta_1^2 + \omega_2^2 \eta_2^2 + \omega_3^2 \eta_3^2) \\ &- 2(k^2 \omega_3 \eta_1 \eta_2 + p^2 \omega_1 \eta_2 \eta_3 + q^2 \omega_2 \eta_1 \eta_3). \end{aligned} \quad (3.2.32)$$

The such defined geometrical object is a complicated structure contained in the full tetrahedron spanned by the  $x_i$ . Finally, we provide the relation between  $\omega_i$  and the spherical triplet variables  $\hat{R}, \theta, \phi$ :

$$\begin{aligned} \omega_1 &= \frac{2\mathcal{S}_0}{3} \hat{R} R_{max}(\Omega) \left( \cos \theta + \sqrt{2} \sin \theta \cos \left( \phi + \frac{2\pi}{3} \right) \right) \\ \omega_2 &= \frac{2\mathcal{S}_0}{3} \hat{R} R_{max}(\Omega) \left( \cos \theta + \sqrt{2} \sin \theta \cos \left( \phi - \frac{2\pi}{3} \right) \right) \\ \omega_3 &= \frac{2\mathcal{S}_0}{3} \hat{R} R_{max}(\Omega) \left( \cos \theta + \sqrt{2} \sin \theta \cos \phi \right). \end{aligned} \quad (3.2.33)$$

Inserting eq. (3.2.34), eq. (3.2.21) and eq. (3.2.39) into eq. (3.2.32), a cubic equation for  $R_{max}(\Omega)$  can be derived. In the appendix A.2 we give a more detailed account of how to solve the cubic equation encountered in the calculation of  $R_{max}$ .

### 3.2.3. Triplet $\mathcal{T}_1$

The phase space of the  $\mathcal{T}_1$  triplet forms a cuboid with vertices at (see figure 3.5)

$$\begin{aligned} \mathcal{C}_{1,2} &= \left( \mp \frac{\sqrt{2}}{3}, 0, 0 \right) & \mathcal{C}_{3,4} &= \left( \mp \frac{2}{3\sqrt{3}}, \mp \frac{4}{3} \sqrt{\frac{2}{3}}, 0 \right) \\ \mathcal{C}_{5,6} &= \left( \mp \frac{2}{3\sqrt{3}}, \mp \frac{2}{3} \sqrt{\frac{2}{3}}, \frac{2\sqrt{2}}{3} \right) & \mathcal{C}_{7,8} &= \left( \mp \frac{2}{3\sqrt{3}}, \mp \frac{2}{3} \sqrt{\frac{2}{3}}, -\frac{2\sqrt{2}}{3} \right). \end{aligned} \quad (3.2.34)$$

The vertices correspond to the limits

$$\eta_1 = \pm \frac{4}{3} \sqrt{\mathcal{S}_0 P^2} \quad \eta_2 = \pm \frac{4}{3} \sqrt{\mathcal{S}_0 P^2} \quad \eta_3 = \pm \frac{4}{3} \sqrt{\mathcal{S}_0 P^2}, \quad (3.2.35)$$

and the symmetric point in the center of the cube is sampled when all relative momenta are orthogonal to  $P$ .

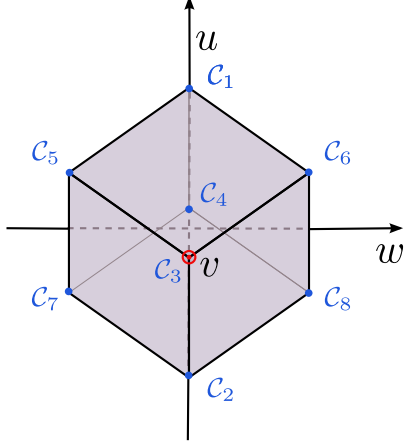


**Figure 3.5.:** Triplet cuboid. The shaded area specifies the physical, space-like region.

In contrast to the tetrahedron and the triangle, we do not expect poles outside of the space-like cuboid, because the variables  $\eta_i$  are not connected to the *square* of any momenta. Thus we assume a weak dependence on this triplet, at least for the tetraquark ground states.

Similar to the triplet  $\mathcal{T}_0$ , we can parametrize the triplet in spherical variables  $\mathcal{T}_1$ ,

$$\mathcal{T}_1 = \sqrt{\mathcal{S}_0 P^2} \rho \rho_{max}(\Omega) \begin{pmatrix} -\cos \vartheta \\ \sin \vartheta \cos \xi \\ -\sin \vartheta \sin \xi \end{pmatrix} = \sqrt{\mathcal{S}_0 P^2} \rho \rho_{max}(\Omega) \begin{pmatrix} \frac{\cos \alpha_r \cos \Phi_\rho \bar{z}_\rho - \sin \alpha_r z_\rho}{Z_\rho} \\ \frac{\sin \alpha_r \cos \Phi_\rho \bar{z}_\rho + \cos \alpha_r z_\rho}{Z_\rho} \\ \frac{\sin \Phi_\rho}{Z_\rho} \end{pmatrix}$$

$$Z_\rho = \sqrt{1 + \frac{1}{2} z_\rho^2 (1 - \cos 2\Phi_\rho)} \quad (3.2.36)$$

$$\hat{\rho} \in [0, 1], \vartheta \in \{0, \pi\}, \xi \in \{0, 2\pi\} \quad (3.2.37)$$

$$\Phi_\rho \in \{-\pi, \pi\}, z_\rho \in \{-1, 1\} \quad (3.2.38)$$

As in the case of  $\mathcal{T}_0$ , we map the triplet variables on a sphere and subsequently use  $\rho_{max}(\Omega)$  to map this sphere on the cube. We also remark that the phase space of the cuboid is not restricted as the tetrahedron in the case of  $\mathcal{T}_0$ .

As long as  $P = (0, 0, 0, iM)$ , the phase space variables  $\eta_i$  are purely imaginary, and  $\rho$  can be rendered purely real by factoring out an  $i$ . When one introduces a width  $P = (0, 0, 0, iM + \Gamma)$ , the phase space gets truly complex. In that case, it is sufficient to define just  $\rho$  to be complex, whereas the singlet  $\mathcal{S}_0$ , doublet  $\mathcal{D}_0$  and the triplet  $\mathcal{T}_0$  can be rendered purely real by replacing  $p, q, k$  with  $p_T, q_T, k_T$ .

Finally, the relations between  $\eta_i$  and  $\rho, \xi, \vartheta$  are provided:

$$\begin{aligned}
\eta_1 &= \frac{2}{\sqrt{3}} i \rho \rho_{max} \sqrt{\mathcal{S}_0 P^2} \left( \cos \vartheta + \sqrt{2} \sin \vartheta \cos \left( \xi + \frac{2\pi}{3} \right) \right) \\
\eta_2 &= \frac{2}{\sqrt{3}} i \rho \rho_{max} \sqrt{\mathcal{S}_0 P^2} \left( \cos \vartheta + \sqrt{2} \sin \vartheta \cos \left( \xi - \frac{2\pi}{3} \right) \right) \\
\eta_3 &= \frac{2}{\sqrt{3}} i \rho \rho_{max} \sqrt{\mathcal{S}_0 P^2} \left( \cos \vartheta + \sqrt{2} \sin \vartheta \cos \xi \right).
\end{aligned} \tag{3.2.39}$$

### 3.3. Flavor structure

We investigate the tetraquarks for quarks in the  $SU(3)$  flavour representation. Quarks with charm quantum number are treated as flavour singlets. The tetraquark consists of two quarks and two antiquarks, which have to be coupled to form flavour multiplets:

$$\bar{\mathbf{3}}_f \otimes \bar{\mathbf{3}}_f \otimes \mathbf{3}_f \otimes \mathbf{3}_f = \mathbf{1}_f \oplus \mathbf{8}_f \oplus \mathbf{10}_f \oplus \bar{\mathbf{10}}_f \oplus \mathbf{27}_f. \tag{3.3.1}$$

To perform the  $SU(3)$  coupling and to obtain the Clebsch-Gordon coefficients one can use the tables found in refs. [110, 111]. A very nice overview of the tetraquark structure, including the tetraquark flavour amplitude, is provided in ref. [8]. We also want to mention the program based on ref. [112], which is capable of performing  $SU(N)$  Clebsch-Gordon decompositions. We assume that the tetraquarks obey the ideal mixing hypothesis, which means that the mesons have a defined  $s$ -Quantum number.

Because our interaction is isospin- and flavour-blind, we restrict our focus on the neutral particles of the light scalar nonet. There are four different kinds of particles, with different symmetries:

**$f_0(500)$**  The  $f_0(500)$  has two flavour components, stemming from a singlet in the  $\bar{\mathbf{3}} \otimes \mathbf{3}$  and  $\bar{\mathbf{6}} \otimes \mathbf{6}$  flavour channel:

$$\begin{aligned}
f_0(500)_{\bar{\mathbf{3}} \otimes \mathbf{3}} &= \frac{1}{2} (\bar{u} \bar{d} u d - \bar{d} \bar{u} u d + \bar{u} d d u + \bar{d} u d u) \\
f_0(500)_{\bar{\mathbf{6}} \otimes \mathbf{6}} &= \frac{1}{2\sqrt{3}} (\bar{u} \bar{d} u d + \bar{u} \bar{d} d u + \bar{u} d d u + \bar{d} u u d - 2\bar{u} \bar{u} u u - 2\bar{d} \bar{d} d d).
\end{aligned} \tag{3.3.2}$$

The symmetry of both amplitudes can be summarized as seen in fig 3.2

State	$P_{12}$	$P_{34}$	$P_{13,24}$	$P_{14,23}$
$f_0(500)_{\bar{\mathbf{3}} \otimes \mathbf{3}}$	-	-	+	+
$f_0(500)_{\bar{\mathbf{6}} \otimes \mathbf{6}}$	+	+	+	+

**Table 3.2.:** Symmetry of the different flavour components of the  $f_0(500)$ .

Both amplitudes are orthogonal to each other. Because our model is flavour-blind, the interaction cannot mix these two states, and we obtain actually two different  $f_0(500)$ . These two states will form one state if one allows flavour changing contributions.

In the case, where all quarks are of the same flavour

$$\bar{c}ccc \quad \bar{s}sss \quad (3.3.3)$$

the flavour amplitude is a singlet under any permutation. In this case there is only one state with a defined symmetry.

**$K_0^*(800)$**  This particle is the equivalent to the Kaon in the pseudo-scalar  $\bar{q}q$  nonet. As the neutral Kaon, the  $K_0^*(800)$  and the  $\bar{K}_0^*(800)$  have no defined charge conjugation quantum number. This problem can be alleviated by forming linear combinations, denoted as  $K_L^*(800)$  and  $K_S^*(800)$ , which resembles the famous ‘K long’ and ‘K short’ in the pseudo-scalar nonet:

$$\begin{aligned} K_S^*(800) &= \frac{1}{2\sqrt{2}}(\bar{u}\bar{s}ud - \bar{u}\bar{s}du + \bar{s}\bar{u}ud - \bar{s}\bar{u}du + \bar{d}\bar{u}su - \bar{u}\bar{d}su + \bar{d}\bar{u}us - \bar{u}\bar{d}us) \\ K_L^*(800) &= \frac{1}{2\sqrt{2}}(\bar{u}\bar{s}ud - \bar{u}\bar{s}du + \bar{s}\bar{u}ud - \bar{s}\bar{u}du - \bar{d}\bar{u}su + \bar{u}\bar{d}su - \bar{d}\bar{u}us + \bar{u}\bar{d}us) \end{aligned} \quad (3.3.4)$$

The symmetries are given in figure 3.3. Different to the  $\sigma$ , the  $K_L^*(800)$  and  $K_S^*(800)$  do not transform with a global sign change under  $P_{12}$  and  $P_{34}$ . We denote this behaviour by  $\pm$  in the table 3.3.

State	$P_{12}$	$P_{34}$	$P_{13,24}$	$P_{14,23}$
$K_S^*(800)$	$\pm$	$\pm$	$-$	$+$
$K_L^*(800)$	$\pm$	$\pm$	$+$	$-$

**Table 3.3.:** Symmetry of the different flavour components of the  $K^*(800)$ .

State	$P_{12}$	$P_{34}$	$P_{13,24}$	$P_{14,23}$
$a_0(980)_{\bar{3}\otimes\bar{6}}$	$+$	$-$	mixed	mixed
$a_0(980)_{6\otimes 3}$	$-$	$+$	mixed	mixed

**Table 3.4.:** Symmetry of the different flavour components of the  $a_0(980)$ .

**$a_0(980)$**  The  $a_0(980)$  is an isospin triplet and comes in three charges. We will only consider the neutral particle. Similar to the rest of the nonet, the  $a_0(980)$  has two flavour amplitudes with different symmetries.

$$\begin{aligned} a_0(980)_{\bar{3}\otimes\bar{6}} &= \frac{1}{2\sqrt{2}}(\bar{d}\bar{s}ds + \bar{u}\bar{s}us + \bar{s}\bar{d}ds + \bar{s}\bar{u}us - \bar{d}\bar{s}sd - \bar{u}\bar{s}su - \bar{s}\bar{d}sd - \bar{s}\bar{u}su) \\ a_0(980)_{6\otimes 3} &= \frac{1}{2\sqrt{2}}(-\bar{d}\bar{s}ds - \bar{u}\bar{s}us + \bar{s}\bar{d}ds + \bar{s}\bar{u}us - \bar{d}\bar{s}sd - \bar{u}\bar{s}su + \bar{s}\bar{d}sd + \bar{s}\bar{u}su). \end{aligned} \quad (3.3.5)$$

As can be seen in table 3.4, charge conjugation is not a ‘good’ symmetry of the flavour amplitude. That means that the flavour amplitude does not transform with a definite global plus or minus. In order to have a well defined charge conjugation quantum number, the flavour components have to be combined individually with appropriate tensor

structures in such a way, that the charge conjugation operation always yields a definite sign. This procedure is always possible. For example, a charge conjugation + state can be constructed by multiplying all flavour components that transform with a minus by

$$P \cdot k. \quad (3.3.6)$$

According to table 3.1, this momentum combinations has the right properties to change just the charge conjugation from + to - without changing the transformation under  $P_{12}$  and  $P_{34}$ .

**$f_0(980)$**  The  $f_0(980)$  mirrors the  $f_0(500)$ . There are two contributions from the  $\bar{3} \otimes 3$  and  $\bar{6} \otimes 6$  flavour channel with different symmetries.

$$\begin{aligned} f_0(980)_{\bar{3} \otimes 3} &= \frac{1}{2\sqrt{2}}(-\bar{s}\bar{u}s u + \bar{u}s s u + \bar{s}\bar{u}u s - \bar{u}\bar{s}u s + \bar{d}\bar{s}d s - \bar{s}\bar{d}d s - \bar{d}\bar{s}s d + \bar{s}\bar{d}s d) \\ f_0(980)_{\bar{6} \otimes 6} &= \frac{1}{2\sqrt{2}}(-\bar{u}\bar{s}u s - \bar{s}\bar{u}u s - \bar{u}\bar{s}s u - \bar{s}\bar{u}s u + \bar{d}\bar{s}d s + \bar{s}\bar{d}d s + \bar{d}\bar{s}s d + \bar{s}\bar{d}s d) \end{aligned} \quad (3.3.7)$$

State	$P_{12}$	$P_{34}$	$P_{13,24}$	$P_{14,23}$
$f_0(980)_{\bar{3} \otimes 3}$	-	-	+	+
$f_0(980)_{\bar{6} \otimes 6}$	+	+	+	+

**Table 3.5.:** Symmetry of the different flavour components of the  $f_0(980)$ .

### 3.4. Color structure

Because of confinement, the bound-states have to be colour singlets. As in the case of the construction of the flavour amplitude, we couple two quarks and two antiquarks:

$$\bar{3}_c \otimes \bar{3}_c \otimes 3_c \otimes 3_c = 1_c \dots \quad (3.4.1)$$

Different from the nucleon and the  $q\bar{q}$ -mesons, we get two colour-singlet structures. Because the Maris-Tandy interaction contains Gell-Mann matrices, the interaction will mix the colour singlets. Here we provide the full colour singlet amplitudes. In this case the characters  $u, d, s$  stand for the three colours  $r, g, b$ .

$$\begin{aligned} 3 \otimes \bar{3}_S &= \frac{1}{2\sqrt{3}}(ud\bar{u}\bar{d} - u\bar{d}\bar{d}\bar{u} - du\bar{u}\bar{d} + du\bar{d}\bar{u} \\ &\quad + su\bar{s}\bar{u} - su\bar{u}\bar{s} - us\bar{s}\bar{u} + us\bar{u}\bar{s} \\ &\quad + ds\bar{d}\bar{s} - ds\bar{s}\bar{d} - s\bar{d}\bar{d}\bar{s} + s\bar{d}\bar{s}\bar{d}) \end{aligned} \quad (3.4.2)$$

and

$$\begin{aligned}
6 \otimes \bar{6}_S = \frac{1}{2\sqrt{6}} & (2ddd\bar{d} + ds\bar{d}\bar{s} + ds\bar{s}\bar{d} \\
& + sdd\bar{s} + sd\bar{s}\bar{d} + 2ss\bar{s}\bar{s} + dud\bar{u} \\
& + du\bar{u}\bar{d} + udd\bar{u} + ud\bar{u}\bar{d} + su\bar{s}\bar{u} \\
& + su\bar{u}\bar{s} + us\bar{s}\bar{u} + us\bar{u}\bar{s} + 2uu\bar{u}\bar{u}).
\end{aligned} \tag{3.4.3}$$

The colour factors for each diagram can now be readily calculated, because all ingredients are known explicitly and can be found in appendix A.3.

### 3.5. Tensor structure

The tetraquark amplitude (wave function) in the quark picture is an object with four internal legs and one external leg. The internal legs carry each a flavour index, a colour index, a Dirac index and a momentum. These internal legs are connected to quarks. The external leg carries a Lorentz index, a colour index, a flavour index and the total momentum of the bound-state. These external indices specify the quantum numbers of the bound-state:  $J_{f,c}^{PC}$ .

In this notation,  $J$  denotes the angular momentum,  $P$  the parity,  $C$  the charge parity,  $f$  specifies in which flavour multiplet the tetraquark resides and  $c$  specifies the colour multiplet of the bound-state. Because all bound-states in QCD are colour singlets, this index will be suppressed. In a graphical representation, the wave function is depicted as:

$$\tag{3.5.1}$$

The single capital  $P$  on the right hand denotes the total momentum. It should be clear from the context if the parity or the total momentum is meant. The leg momenta are labeled  $p_1, p_2, p_3, p_4$ . The red arrow specifies the flow direction of these momenta and the black arrow specifies the spin-line of the attached quarks. The indices  $\{c_1, c_2, c_3, c_4\} \in \{1 \dots 3\}$  represent the colour indices of each leg and  $\{f_1, f_2, f_3, f_4\} \in \{1 \dots 3\}$  the flavour indices. Because the underlying group structure of both flavour and colour is  $SU(3)$ , the indices run over the interval  $\{1 \dots 3\}$ . The last index set is formed by the Dirac indices  $\{a, b, c, d\} \in \{1 \dots 4\}$ . The upper two legs are attached to anti-quarks and the lower two legs to quarks.

In the following chapters, permutation operations will play an important role and some notations will be introduced beforehand. The permutation of any two legs  $i, j$ , including momenta and all attached indices, will be denoted by  $P_{ij}$ .

The general structure of the tensor structure of the tetraquark, with flavour and colour related indices suppressed, reads:

$$\Gamma_{abcd}^{\{\mu\nu\dots\}} = \sum_i T_{abcd}^{\{\mu\nu\dots\},i}(p_1, p_2, p_3, p_4, \Omega) f^i(\Omega) \quad (3.5.2)$$

$$T_{abcd}^{\{\mu\nu\dots\},i} = (\tau_{1,ab}^i \otimes \tau_{2,cd}^i)^{\{\mu\nu\dots\}}(p_1, p_2, p_3, p_4, \Omega). \quad (3.5.3)$$

Here the index  $i$  runs over the different tensor structures and  $\Omega$  stands for a set of nine Lorentz invariants formed from  $p_1, p_2, p_3, p_4$ . The index set  $\{\mu\nu\dots\}$  encodes the total angular momentum ( $J$ ) of the state. A scalar/pseudo-scalar tetraquark has no such index, a vector/axial-vector state carries one etc.

The scalar dressing functions are denoted by  $f^i(\Omega)$ . Suppressing any Lorentz index, the direct tensor product  $\tau_{1,ab}^i(\Omega) \otimes \tau_{2,cd}^i(\Omega)$  carries the full Dirac structure. There are three different choices to pair up the indices.

$$(ab), (cd) : (D) \quad (3.5.4)$$

$$(ac), (bd) : (M_I) \quad (3.5.5)$$

$$(ad), (bc) : (M_{II}) \quad (3.5.6)$$

Transformations between the different composition are achieved by means of Fierz transformations. The first of the three combinations ( $D$ ) combines two quark legs and two anti-quark legs and is therefore identified with a diquark-(anti-)diquark decomposition. The other two combinations ( $M_I$ ), ( $M_{II}$ ) pair a quark and an anti-quark leg and are thus classified as meson-meson decompositions. The amplitudes can be expressed in the ( $D$ ) and in the ( $M_I, M_{II}$ ) decomposition without losing any information because a transformation between them is always possible. In the rest of this work the ( $D$ ) is chosen because the Pauli principle is much easier to establish in this decomposition. In the following we will consider the scalar tetraquark only.

### 3.5.1. Quantum numbers

The tetraquark is characterized by its quantum numbers  $J$ ,  $C$  (charge conjugation) and  $P$  (parity), subsumed in the notation  $J^{PC}$ . In order to construct a tensor structure that respects the symmetries connected with the quantum numbers, we first introduce the corresponding operators and then perform the construction.

**Parity** The action of the parity operator  $\mathcal{P}$  on the tetraquarks tensor structure can be written as:

$$\begin{aligned} \mathcal{P}[T_{abcd}^{\{\mu\nu\dots\},i}(p_1, p_2, p_3, p_4, \Omega) f^i(\Omega)] = \\ (\gamma_4 \tau_1^i \otimes \gamma_4 \tau_2^i)^{\{\mu\nu\dots\}}(\Lambda p_1, \Lambda p_2, \Lambda p_3, \Lambda p_4, \Omega_9) f^i(\Omega). \end{aligned} \quad (3.5.7)$$

Here  $\Lambda = \text{Diag}(-1, -1, -1, 1)$  multiplies the spatial part of a Lorentz four-vector with  $-1$  and  $\gamma_4$  is one of the euclidean gamma matrix. The set of Lorentz invariants  $\Omega$  is invariant under a parity transformation.

**Charge Conjugation** The charge conjugation operator  $\mathcal{C}\mathcal{C}_{13,24}$  exchanges quarks and antiquarks and multiplies the tensor structure with  $\mathcal{C} = \gamma_2\gamma_4$ :

$$\begin{aligned} \mathcal{C}\mathcal{C}_{13,24}[T_{abcd}^{\{\mu\nu\dots\},i}(p_1, p_2, p_3, p_4, \Omega) f^i(\Omega)] = \\ (\mathcal{C}\tau_1^i\mathcal{C}_{cd}^T \otimes \mathcal{C}\tau_2^i\mathcal{C}_{ab}^T)^{\{\mu\nu\dots\}}(p_3, p_4, p_1, p_2, \Omega_{CC})f^i(\Omega_{CC}). \end{aligned} \quad (3.5.8)$$

The Lorentz invariants are not invariant under a charge conjugation and the new set is named  $\Omega_{CC}$ . Besides the momenta, charge conjugation also permutes the Dirac indices. As can be seen in (3.5.8), this interchange is equivalent to a permutation of the structures  $\tau_1$  and  $\tau_2$ .

There is another possible charge conjugation operation which interchanges the legs 1, 4 and 2, 3. This charge conjugation can be written as a combination of  $\mathcal{C}\mathcal{C}_{13,24}$  and a subsequent permutation  $P_{34}$ . Because the tensor structure is symmetric or anti symmetric under  $P_{34}$  by construction, it is sufficient to consider  $\mathcal{C}\mathcal{C}_{13,24}$ .

**Time reversal** The Time reversal operator reads in euclidean space:

$$\begin{aligned} \mathcal{T}[T_{abcd}^{\{\mu\nu\dots\},i}(p_1, p_2, p_3, p_4, \Omega) f^i(\Omega)] = \\ (\gamma_5\mathcal{C}(\tau_1^i)^*\gamma_5\mathcal{C}_{cd}^T \otimes \gamma_5\mathcal{C}(\tau_2^i)^*\gamma_5\mathcal{C}_{ab}^T)^{\{\mu\nu\dots\}}(p_1^*, p_2^*, p_3^*, p_4^*, \Omega)f^i(\Omega)^*, \end{aligned} \quad (3.5.9)$$

with the  $*$  denoting a complex conjugation. Because the euclidean total momentum vector reads  $P = (0, 0, 0, iM)$ , the phase space variables  $\eta_i$  transform as  $\eta_1 \rightarrow -\eta_1$  under  $\mathcal{T}$ . In terms of the variables introduced in sec. 3.2.3, this transformation reads:

$$\begin{aligned} z_\rho &\rightarrow -z_\rho \\ \Phi_\rho &\rightarrow \Phi_\rho + \pi. \end{aligned} \quad (3.5.10)$$

Because the combined symmetry  $\mathcal{CPT}$  is a good symmetry, yielding a minus if the object carries an odd number of Lorentz indices and a plus if the number is even, instead of charge conjugation, a time reversal operation combined with a parity operation can be applied. Because the time reversal in eq. (3.5.10) does not involve an interpolation on  $\Omega$  when choosing a suitable grid, this operation is numerically considerably cheaper to carry out.

**Pauli principle** The Pauli principle is not related to a quantum number, but an important property of the complete tetraquark wave function.

The Pauli principle states that under exchange of any two quarks, equivalent to  $P_{34}$ , or antiquarks, equivalent to  $P_{12}$ , the amplitude picks up a minus sign. The exchange of two quarks involves the interchange of all flavour, colour and Dirac indices, and also an exchange of the momenta associated with the two quarks. Because the colour and flavour structures have a definite transformation property under  $P_{34}$  and  $P_{12}$ , see chapter 3.4 and

3.3, the transformation property of the Dirac-structure is also fixed.

Before we construct the amplitudes, we give in the next section a short argument why there are 256 linear independent tensor structures.

**Number of tensor structures** The number (256) of linear independent tensor structures can be determined from its quantum numbers and a bit of  $\gamma$ -matrix technology. First one combines the 16 elements of the Clifford-algebra, formed by the Dirac  $\gamma$ -matrices, with the 4 momenta  $p_1, p_2, p_3, p_4$  into two sets of tensors with Dirac indices:

$$I = \{\mathbb{1}, \not{p}_i, [\not{p}_i, \not{p}_j]\} \quad II = \{\gamma_5, \gamma_5 \not{p}_i\} \quad i, j \in \{1 \dots 4\}, i > j. \quad (3.5.11)$$

The first set has positive parity and the second set has a negative one. These two sets can be combined via a direct product to form a object with four Dirac indices. This tensor product can be again grouped into a set of two sets with different parity:

$$T_I = \{I \otimes I, II \otimes II\}, \quad T_{II} = \{I \otimes II, II \otimes I\}. \quad (3.5.12)$$

The set  $T_I$  has positive parity and the set denoted by  $T_{II}$  carries a negative parity. If the second or first set is combined with the negative parity factor

$$\epsilon^{\mu\nu\lambda\eta} p_1^\mu p_2^\nu p_3^\lambda p_4^\eta, \quad (3.5.13)$$

both sets have the same parity respectively, denoted by the superscript  $\pm$ . Barring collinear kinematic configurations, the four 4-vectors  $p_i$  can be orthogonalized and it follows that all elements in  $T_I^\pm$  and  $T_{II}^\pm$  are orthogonal to each other. The total number count is thus 256. This is also the maximal number of linear independent tensor structures with four Dirac indices that can be constructed from the Dirac matrices in four dimensions.

It is important to point out that the set of tensor structures  $T_I, T_{II}$ , introduced in this chapter, are not a good choice for actual calculations because important symmetries, such as the Pauli principle, interrelate the different amplitudes in a complicated manner. A better suited basis is constructed in the following sections.

**Consideration for higher J** In order to construct the tetraquark amplitude for  $J = 1$ , we need structures that carry one open Lorentz-index and are transversal to  $P$ . A possible choice for such structures are the three orthogonal momenta

$$\tilde{p}_i^\mu. \quad (3.5.14)$$

Here the tilded momenta are some linear combinations of  $p_i$  that are transverse to the total momentum  $P = \frac{1}{4} \sum_{i=1}^4 p_i$ . Such a combination of momenta are for example the relative momenta

$$p_T, q_T, k_T. \quad (3.5.15)$$

This momenta can be combined with the 256 structures of  $T_I^\pm$  and  $T_{II}^\pm$  so that we can conclude that the  $J = 1$  tetraquark has  $3 \times 256 = 768$  linear independent tensor structures.

Instead of using three orthogonal momenta as basis for the Lorentz-index carrying structure, we can alternatively use the following structures that maximize the number of momentum independent tensor structures:

$$\gamma_T^\mu \quad (3.5.16)$$

$$3 \mathbb{1} w^\mu - \psi \gamma_T^\mu \quad (3.5.17)$$

$$u^\mu \psi + v^\mu \bar{\psi}, \quad (3.5.18)$$

with the momenta  $u, v, w$  defined as in eq. (3.5.34). The orbital angular momentum  $L$  of each structure reads 0, 1, 2 from top to bottom. These three tensors would be the natural starting point for the construction of a complete  $J = 1$  amplitude, respecting all relevant symmetries.

### 3.5.2. LS-decomposition

For  $J = 0$ , the tensor structures transform as Lorentz scalars. The angular momentum  $J$  can be furthermore decomposed into its spin  $S$  and orbital angular momentum  $L$ . In general, these are not good quantum numbers because they are not Lorentz invariant and thus frame dependent. But the bound-state equation is formulated in the rest frame of the tetraquark, which does not change during the calculation, and so for calculation purposes, a partial wave decomposition of the tensor structure is worthwhile. Especially taking into account that studies investigating the ground state properties of the nucleon and  $\Delta$  have shown that the tensor structures with  $L > 0$  are subleading [93]. Assuming that a similar mechanism also applies for the tetraquark, we will drop all tensor structures from the actual calculation that have  $L > 0$ . But to be able to ignore all structures with  $L > 0$ , we first have to perform the complete LS-decomposition of the tetraquark amplitude.

A similar decomposition was performed for the nucleon in refs. [96, 113] and we will follow the same prescription given there to construct the  $LS$ -decomposition for the tetraquark. The first ingredient in an LS-decomposition is the Pauli-Lubanski operator in the rest frame, and the eigenvalues of its square :

$$W^\mu = \frac{1}{2} \epsilon^{\mu\nu\alpha\beta} \hat{P}^\nu J^{\alpha\beta} = S^\mu + L_u^\mu + L_v^\mu + L_w^\mu. \quad (3.5.19)$$

$$W^2 \rightarrow J(J+1) \quad (3.5.20)$$

In this notation, the total momentum  $\hat{P}$  is normalized to 1, indicated by the hat  $\hat{\cdot}$ . The vectors  $u, v, w$  are assumed to be ortho-normal. The eigenvalue of the Pauli-Lubanski

operator determines the total angular momentum of the tetraquark. The spin operator  $S^\mu$  and the orbital angular momentum operators  $L_{u,v,w}^\mu$  that appear on the right-hand side read

$$S^\mu = \frac{1}{4} \epsilon^{\mu\nu\alpha\beta} \hat{P}^\nu \left( \sigma^{\alpha\beta} \otimes \mathbb{1} \otimes \mathbb{1} \otimes \mathbb{1} + \text{perm} \right) \quad (3.5.21)$$

$$L_{(y)}^\mu = \frac{i}{2} \epsilon^{\mu\nu\alpha\beta} \hat{P}^\nu \left( y^\alpha \partial_y^\beta - y^\beta \partial_y^\alpha \right) \mathbb{1} \otimes \mathbb{1} \otimes \mathbb{1} \otimes \mathbb{1}, \quad (3.5.22)$$

where  $y$  represents any four-vector, and  $\sigma^{\alpha\beta}$  is defined as

$$\sigma^{\alpha\beta} = -\frac{i}{2} [\gamma^\alpha, \gamma^\beta]. \quad (3.5.23)$$

In order to construct the eigenvectors of  $W^2$ , the products of these operators are needed:

$$S^2 = 3 (\mathbb{1} \otimes \mathbb{1} \otimes \mathbb{1} \otimes \mathbb{1}) + \frac{1}{4} \left( \sigma_T^{\alpha\beta} \otimes \sigma_T^{\alpha\beta} \otimes \mathbb{1} \otimes \mathbb{1} + \text{perm} \right) \quad (3.5.24)$$

$$L_{(y)}^2 = 2y_T \cdot \partial_y + \left( y_T^\alpha y_T^\beta - y_T^2 T_P^{\alpha\beta} \right) \partial_y^\alpha \partial_y^\beta \quad (3.5.25)$$

$$L_{(y)} \cdot L_{(z)} = \left( y_T^\alpha z_T^\beta - y_T \cdot z_T T_P^{\alpha\beta} \right) \partial_y^\beta \partial_z^\alpha. \quad (3.5.26)$$

The definition of the transverse projector  $T_P^{\alpha\beta}$  and the transverse  $\sigma_T^{\alpha\beta}$ -matrices is given by

$$T_P^{\alpha\beta} = \delta^{\alpha\beta} - \hat{P}^\alpha \hat{P}^\beta \quad (3.5.27)$$

$$\sigma_T^{\alpha\beta} = -\frac{i}{2} [\gamma_T^\alpha, \gamma_T^\beta] \quad (3.5.28)$$

$$\gamma_T^\alpha = T_P^{\alpha\beta} \gamma^\beta = \gamma^\alpha - \hat{P}^\alpha \hat{P}. \quad (3.5.29)$$

As shown in section 3.5.1, there are 256 linear independent tensor structures. Using a different decomposition, this space can be factorized into 8 sets which are orthogonal to each other:

$$(\mathbb{1} \pm \hat{P}) \otimes (\mathbb{1} \pm \hat{P}) \cdot \{R_1 \otimes R_2\} := (\mathbb{1} \pm \hat{P}) R_1 \otimes (\mathbb{1} \pm \hat{P}) R_2 \quad (3.5.30)$$

$$\gamma_5(\mathbb{1} \pm \hat{P}) \otimes \gamma_5(\mathbb{1} \pm \hat{P}) \cdot \{R_1 \otimes R_2\} := \gamma_5(\mathbb{1} \pm \hat{P}) R_1 \otimes \gamma_5(\mathbb{1} \pm \hat{P}) R_2. \quad (3.5.31)$$

Here any permutation of the signs  $\pm$  is allowed, the dot  $\cdot$  denotes an ordinary matrix multiplication of all tensors on the right and left side of  $\otimes$  respectively, and the set  $\{R_1 \otimes R_2\}$  stands for the ‘rest’ of the tensor structure. Because  $\gamma_5$  and  $\mathbb{1} \pm \hat{P}$  have an orbital angular momentum of  $L = 0$ , the set  $\{R_1 \otimes R_2\}$ , containing 32 elements, will carry all the orbital angular momentum. The momenta  $u, v, w, P$ , appearing in eq. (3.5.19), are assumed to be orthonormal.

The vectors  $u, v, w$  can be constructed by combination of the three vectors  $p_T, q_T, k_T$  introduced in eq. (3.2.2):

vector	$P_{12}$	$P_{34}$	$P_{13,24}/P_{14,23}$
$\mathbf{u}$	$\mathbf{u}$	$\mathbf{u}$	$-\mathbf{u}$
$\mathbf{v}$	$-\mathbf{v}$	$-\mathbf{v}$	$\mathbf{v}$
$\mathbf{w}$	$-\mathbf{w}$	$-\mathbf{w}$	$-\mathbf{w}$

**Table 3.6.:** Transformation properties of the vectors  $u, v, w$ .

$$u := k_T \tag{3.5.32}$$

$$v := p_T(q_T \cdot k_T) - q_T(p_T \cdot k_T) \tag{3.5.33}$$

$$w := u_T \times v_T = (k_T \times p_T)(q_T \cdot k_T) - (k_T \times q_T)(p_T \cdot k_T). \tag{3.5.34}$$

Orthogonality of these three momenta to each other is immediately clear, as is the orthogonality to  $P$ . The  $S_4$ -transformation properties of these three vectors are given in table 3.6. The final result for the 32 amplitudes that, together with the factors in eq. (3.5.31), span the whole tetraquark amplitude space, is given in table 3.7.

### 3.5.3. Construction of symmetric tensor structures

The LS-decomposition is a first step in constructing a proper basis that reflects all the symmetries of the tetraquark. In the next step, one has to linear combine the structures in table 3.7 within the s-wave ( $L=0$ ), p-wave ( $L=1$ ) and d-wave ( $L=2$ ) channels, to get tensor structures that have a defined transformation property under parity, charge conjugation and an exchange of two quarks and two anti-quarks.

In table 3.8, this procedure was done for the momentum independent s-waves. The columns denoted by  $C, P, T$  provide the transformation property under  $CPT$ . The abbreviation  $F$  specifies the sign, that the amplitude picks up when performing a Fierz-transformation as detailed in section 3.6. If amplitudes do not transform automorphically, the amplitude *into* which they transform is provided in brackets.

As an example, we show the explicit calculation to obtain the transformation properties for the first amplitude in table 3.8:

#### Quark exchange $P_{12}$

$$\begin{aligned} & (\mathcal{C}^T \gamma_5)_{2,1} \otimes (\gamma_5 \mathcal{C})_{3,4} \xrightarrow{P_{12}} (\mathcal{C}^T \gamma_5)_{1,2} \otimes (\gamma_5 \mathcal{C})_{3,4} = \\ & = (\gamma_5^T \mathcal{C})_{2,1} \otimes (\gamma_5 \mathcal{C})_{3,4} = (\mathcal{C} \mathcal{C}^T \gamma_5^T \mathcal{C})_{2,1} \otimes (\gamma_5 \mathcal{C})_{3,4} = \\ & = (\mathcal{C} \gamma_5)_{2,1} \otimes (\gamma_5 \mathcal{C})_{3,4} = -(\mathcal{C}^T \gamma_5)_{2,1} \otimes (\gamma_5 \mathcal{C})_{3,4} \end{aligned} \tag{3.5.35}$$

#### Charge conjugation $C_{13,24}$

$$\begin{aligned} & (\mathcal{C}^T \gamma_5)_{2,1} \otimes (\gamma_5 \mathcal{C})_{3,4} \xrightarrow{C_{13,24}} (\mathcal{C} \mathcal{C}^T \gamma_5 \mathcal{C}^T)_{4,3} \otimes (\mathcal{C} \gamma_5 \mathcal{C} \mathcal{C}^T)_{1,2} = \\ & = (\gamma_5 \mathcal{C}^T)_{4,3} \otimes (\mathcal{C} \gamma_5)_{1,2} = (\mathcal{C} \gamma_5^T \mathcal{C}^T \mathcal{C})_{3,4} \otimes (\mathcal{C} \mathcal{C}^T \gamma_5^T \mathcal{C})_{2,1} = \\ & = (\gamma_5 \mathcal{C})_{3,4} \otimes (\mathcal{C}^T \gamma_5)_{2,1} \end{aligned} \tag{3.5.36}$$

Here we used the properties of the charge conjugation matrices

$$\mathcal{C}^T \mathcal{C} = \mathbb{1}, \quad \mathcal{C}^T = -\mathcal{C} \quad (3.5.37)$$

and the charge conjugation properties of the Dirac-matrices, see ref. [114]. Additionally the following property is useful to derive the transformations:

$$\gamma_T^\mu \not{P} = -\not{P} \gamma_T^\mu. \quad (3.5.38)$$

### 3.6. Amplitude conventions and Fierz transformations

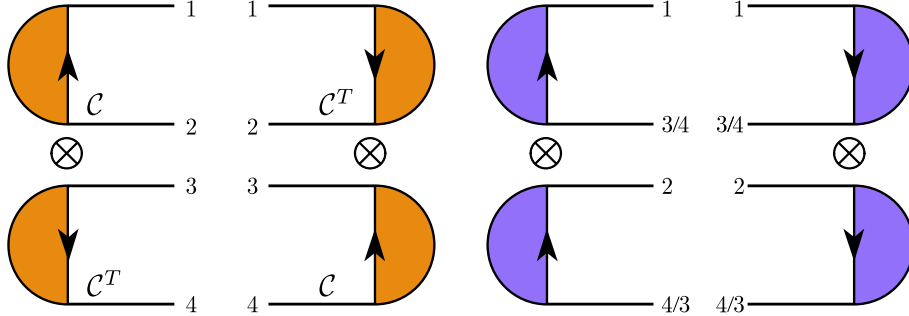


**Figure 3.6.:** Index convention for the (D)-decomposition on the left-hand side and ( $M_{I/II}$ )-decomposition on the right-hand side. The charge conjugation matrices, that are part of the tensor structure, are explicitly drawn at the quark line, denoted by the number, they are attached to. The arrow specifies the spin-line of the tensor structure. When performing a matrix-matrix product all involved quantities are supposed to have an index ordering against the spin-line.

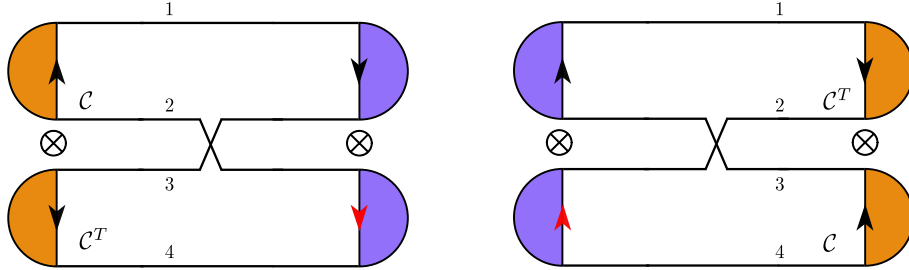


**Figure 3.7.:** Index convention for a Fierz-transformation from (D)-decomposition to the ( $M_I$ )-decomposition. The red arrow denotes the tensor structure that has to be transposed.

We adopt the index convention as depicted in figure 3.6 for the tetraquark amplitude. The choice we took has no particular benefit but it is of utmost importance to stick to the chosen convention when performing projections, Fierz-transformation etc. When performing a matrix-matrix product all involved quantities (quarks, vertices, tensor structures) are supposed to be traced against the spin-line. This means that for any matrix object  $A_{ij}$ , the index  $i$  is located at the front of the spin-line arrow and  $j$  at the rear. For a matrix-matrix product, all pairwise summed indices are supposed to be adjacent. Whenever this is not the case, an appropriate transposition of the matrix is performed.

This is the case for the Fierz-transformation in figure 3.7: The lower tensor structure of the  $(M_I)$ -decomposition has to be transposed. The red arrow denotes the structure that has the wrong spin-line direction. Together with the  $\mathcal{C}, \mathcal{C}^T$  on both sides of the amplitude, this amounts to a charge conjugation of the tensor structure.

### 3.7. Polynomial representation and interpolation

The scalar dressing functions of the tetraquark are defined on a cartesian grid which we call the external grid. In order to calculate the BSE we have to integrate over these scalar dressing functions. The grid points of the integration grid constitute the so-called internal grid. The points of both grids do not coincide for all diagrams. Therefore, in order to evaluate the dressing functions under the integral, we have to interpolate these dressing functions. We employ an interpolation rule that is constructed as the tensor product of nine one-dimensional polynomial interpolation rules. The complete nine-dimensional interpolation rule reads

$$\begin{aligned}
f(\mathcal{S}_0, r, R, \rho, \varphi, z_R, \Phi_R, z_\rho, \Phi_\rho) = & \\
& \sum_{i_1=1}^{N_{\mathcal{S}_0}} \frac{w_{i_1}}{(\mathcal{S}_0)_{i_1} - \mathcal{S}_0} \sum_{i_2=1}^{N_r} \frac{w_{i_2}}{(r)_{i_2} - r} \sum_{i_3=1}^{N_R} \frac{w_{i_3}}{(R)_{i_3} - R} \\
& \sum_{i_4=1}^{N_\rho} \frac{w_{i_4}}{(\rho)_{i_4} - \rho} \sum_{i_5=1}^{N_\varphi} \frac{w_{i_5}}{(\varphi)_{i_5} - \varphi} \sum_{i_6=1}^{N_{z_R}} \frac{w_{i_6}}{(z_R)_{i_6} - z_R} \\
& \sum_{i_7=1}^{N_{\Phi_R}} \frac{w_{i_7}}{(\Phi_R)_{i_7} - \Phi_R} \sum_{i_8=1}^{N_{z_\rho}} \frac{w_{i_8}}{(z_\rho)_{i_8} - z_\rho} \sum_{i_9=1}^{N_{\Phi_\rho}} \frac{w_{i_9}}{(\Phi_\rho)_{i_9} - \Phi_\rho} \times \\
& \times f\left((\mathcal{S}_0)_{i_1}, (r)_{i_2}, (R)_{i_3}, (\rho)_{i_4}, (\varphi)_{i_5}, (z_R)_{i_6}, (\Phi_R)_{i_7}, (z_\rho)_{i_8}, (\Phi_\rho)_{i_9}\right), \quad (3.7.1)
\end{aligned}$$

with  $N_{(\cdot)}$  specifying the number of points in each dimension and  $w_i$  and  $(\cdot)_i$  denoting the weights and nodes of the one-dimensional rules respectively. For each dimension a Chebyshev rule was used and the corresponding weights and nodes were taken from ref. [70]. The nodes in each dimension are defined on the domains as specified in chapter 3.2.

#	L	$R_1 \otimes R_2$	Norm factor
1	0	$\mathbb{1} \otimes \mathbb{1}$	1
2	0	$\gamma_T^\mu \otimes \gamma_T^\mu$	$\sqrt{3}$
3	0	$\mathbb{1} \otimes [(\psi\psi - \phi\psi)\psi + (\phi\psi - \psi\phi)\psi + (\psi\psi - \psi\psi)\phi]$	6
4	0	$\gamma_T^\mu \otimes \gamma_T^\mu [(\psi\psi - \phi\psi)\psi + (\phi\psi - \psi\phi)\psi + (\psi\psi - \psi\psi)\phi]$	$\sqrt{108}$
5	1	$3\psi \otimes \mathbb{1} - \gamma_T^\mu \otimes \psi\gamma_T^\mu$	$\sqrt{6}$
6	1	$3\phi \otimes \mathbb{1} - \gamma_T^\mu \otimes \phi\gamma_T^\mu$	$\sqrt{6}$
7	1	$3\psi \otimes \mathbb{1} - \gamma_T^\mu \otimes \psi\gamma_T^\mu$	$\sqrt{6}$
8	1	$3\phi\psi \otimes \mathbb{1} - \gamma_T^\mu \otimes \phi\psi\gamma_T^\mu$	$\sqrt{12}$
9	1	$3\psi\phi \otimes \mathbb{1} - \gamma_T^\mu \otimes \psi\phi\gamma_T^\mu$	$\sqrt{12}$
10	1	$3\psi\phi \otimes \mathbb{1} - \gamma_T^\mu \otimes \psi\phi\gamma_T^\mu$	$\sqrt{12}$
11	1	$\psi\gamma_T^\mu \otimes \gamma_T^\mu$	$\sqrt{3}$
12	1	$\phi\gamma_T^\mu \otimes \gamma_T^\mu$	$\sqrt{3}$
13	1	$\psi\gamma_T^\mu \otimes \gamma_T^\mu$	$\sqrt{3}$
14	1	$\not{P}\phi\psi\gamma_T^\mu \otimes \gamma_T^\mu$	$\sqrt{3}$
15	1	$\not{P}\psi\phi\gamma_T^\mu \otimes \gamma_T^\mu$	$\sqrt{3}$
16	1	$\not{P}\psi\psi\gamma_T^\mu \otimes \gamma_T^\mu$	$\sqrt{3}$
17	1	$\psi \otimes \mathbb{1}$	1
18	1	$\phi \otimes \mathbb{1}$	1
19	1	$\psi \otimes \mathbb{1}$	1
20	1	$\phi\psi \otimes \mathbb{1}$	1
21	1	$\psi\phi \otimes \mathbb{1}$	1
22	1	$\psi\psi \otimes \mathbb{1}$	1
23	2	$2\phi \otimes \phi - \psi \otimes \psi - \psi \otimes \psi$	$\sqrt{6}$
24	2	$\psi \otimes \psi - \psi \otimes \psi$	$\sqrt{2}$
25	2	$\psi \otimes \psi - \psi \otimes \psi$	$\sqrt{2}$
26	2	$\psi \otimes \phi - \phi \otimes \psi$	$\sqrt{2}$
27	2	$\psi \otimes \phi - \phi \otimes \psi$	$\sqrt{2}$
28	2	$\phi \otimes [\phi\psi - \psi\phi] - \frac{1}{2}\gamma_T^\mu \otimes [\gamma_T^\mu\psi - \psi\gamma_T^\mu]$	$\sqrt{2}$
29	2	$\phi \otimes [\phi\psi - \psi\phi] - \frac{1}{2}\gamma_T^\mu \otimes [\gamma_T^\mu\psi - \psi\gamma_T^\mu]$	$\sqrt{2}$
30	2	$\psi \otimes [\psi\phi - \phi\psi] - \frac{1}{2}\gamma_T^\mu \otimes [\gamma_T^\mu\phi - \phi\gamma_T^\mu]$	$\sqrt{2}$
31	2	$-2\phi \otimes [\psi\psi - \psi\psi] + \psi \otimes [\phi\psi - \psi\phi] + \psi \otimes [\psi\psi - \psi\psi]$	$\sqrt{24}$
32	2	$-2\phi\gamma_T^\mu \otimes \gamma_T^\mu [\psi\psi - \psi\psi] + \psi\gamma_T^\mu \otimes \gamma_T^\mu [\phi\psi - \psi\phi] + \psi\gamma_T^\mu \otimes \gamma_T^\mu [\psi\psi - \psi\psi]$	$\sqrt{24}$

**Table 3.7.:** L-S decomposition of the tetraquark structure. Divide by  $N$  to normalize the tensor structure to 1.

#	Structure	$P_{12}$	$P_{34}$	$C$	$T$	$F$	Norm
1	$(\mathcal{C}^T \gamma_5)_{2,1} \otimes (\gamma_5 \mathcal{C})_{3,4}$	-(1)	-(1)	+	+	+(1)	1
2	$\mathcal{C}^T \gamma_5 \not{P} \otimes \gamma_5 \mathcal{C} + \mathcal{C}^T \gamma_5 \otimes \gamma_5 \not{P} \mathcal{C}$	-(2)	-(2)	+	+	+(2)	$\sqrt{2}$
3	$\mathcal{C}^T \gamma_5 \not{P} \otimes \gamma_5 \mathcal{C} - \mathcal{C}^T \gamma_5 \otimes \gamma_5 \not{P} \mathcal{C}$	-(3)	-(3)	-	+	+(3)	$\sqrt{2}$
4	$\mathcal{C}^T \gamma_5 \not{P} \otimes \gamma_5 \not{P} \mathcal{C}$	-(4)	-(4)	+	+	+(4)	1
5	$\mathcal{C}^T \gamma_T^\mu \otimes \gamma_T^\mu \mathcal{C}$	+(5)	+(5)	+	+	-(5)	$\sqrt{3}$
6	$\mathcal{C}^T \gamma_T^\mu \not{P} \otimes \gamma_T^\mu \mathcal{C} + \mathcal{C}^T \gamma_T^\mu \otimes \gamma_T^\mu \not{P} \mathcal{C}$	+(6)	+(6)	+	+	-(6)	$\sqrt{6}$
7	$\mathcal{C}^T \gamma_T^\mu \not{P} \otimes \gamma_T^\mu \mathcal{C} - \mathcal{C}^T \gamma_T^\mu \otimes \gamma_T^\mu \not{P} \mathcal{C}$	+(7)	+(7)	-	+	-(7)	$\sqrt{6}$
8	$\mathcal{C}^T \gamma_T^\mu \not{P} \otimes \gamma_T^\mu \not{P} \mathcal{C}$	+(8)	+(8)	+	+	-(8)	$\sqrt{3}$
9	$\mathcal{C}^T \mathbb{1} \otimes \mathbb{1} \mathcal{C}$	-(9)	-(9)	+	+	+(9)	1
10	$\mathcal{C}^T \not{P} \otimes \mathcal{C} - \mathcal{C}^T \otimes \not{P} \mathcal{C}$	+(11)	-(11)	-	+	+(10)	$\sqrt{2}$
11	$\mathcal{C}^T \not{P} \otimes \mathcal{C} + \mathcal{C}^T \otimes \not{P} \mathcal{C}$	+(10)	-(10)	+	+	+(11)	$\sqrt{2}$
12	$\mathcal{C}^T \gamma_T^\mu \not{P} \otimes \gamma_T^\mu \not{P} \mathcal{C}$	+(12)	+(12)	+	+	+(12)	1
13	$\mathcal{C}^T \gamma_T^\mu \gamma_5 \otimes \gamma_T^\mu \gamma_5 \mathcal{C}$	-(13)	-(13)	+	+	+(13)	$\sqrt{3}$
14	$\mathcal{C}^T \gamma_T^\mu \gamma_5 \not{P} \otimes \gamma_T^\mu \gamma_5 \mathcal{C} + \mathcal{C}^T \gamma_T^\mu \gamma_5 \otimes \gamma_T^\mu \gamma_5 \not{P} \mathcal{C}$	+(15)	-(15)	-	+	+(15)	$\sqrt{6}$
15	$\mathcal{C}^T \gamma_T^\mu \gamma_5 \not{P} \otimes \gamma_T^\mu \gamma_5 \mathcal{C} - \mathcal{C}^T \gamma_T^\mu \gamma_5 \otimes \gamma_T^\mu \gamma_5 \not{P} \mathcal{C}$	+(14)	-(14)	+	+	+(14)	$\sqrt{6}$
16	$\mathcal{C}^T \gamma_T^\mu \gamma_5 \not{P} \otimes \gamma_T^\mu \gamma_5 \not{P} \mathcal{C}$	+(16)	+(16)	+	+	+(16)	$\sqrt{3}$

**Table 3.8.:** Symmetrized and momentum independent s-wave tensor structures. For details see chapter 3.5.3. The subscripts in the first line denote the Dirac index labeling of the amplitude, with the number specifying the quark leg the index is attached to. Divide by  $N$  to normalize the tensor structure to 1.

## 4. Singularity structure and threshold effects

As mentioned in chapter 3.2, the tetraquark BSE contains two-body poles inside and outside of the doublet triangle. In this chapter we investigate the nature of these poles from two different points of view. First of all we elucidate the origin of the poles and show that they entail a threshold condition. In the next we show numerical results that demonstrate the emergence of the poles and investigate the influence on the spectrum and the shape of the tetraquark amplitudes. We also explain the numerical difficulties that these poles pose and how we (partially) solved them.

### 4.1. Phase space arguments

There are several kinds of singularities that can appear in the tetraquark bound-state equation. One can distinguish between singularities of the static components and dynamical singularities which are ‘created’ during iterations.

**Static singularities** The static singularities are known beforehand and lead to restrictions on the phase space. In this work the objects that have known singularities are the quarks and gluons.

The quark propagator in the Maris-Tandy model develops poles in the complex plane, see chapter 2.7. These poles are never probed as long as the total mass  $P$  in the tetraquark BSE stays below a critical value of the order of  $2\text{ GeV}$  for light quarks ( $m_q \approx 4\text{ MeV}$ ) and  $7\text{ GeV}$  for heavy quarks ( $m_q \approx 0.9\text{ GeV}$ ).

The gluon has a kinematic singularity for relative momenta  $p_g = 0$ . This singularity appears only at the integration boundary and is integrable.

**Dynamical singularities** The dynamical singularities are not obvious from the tensor structure but ‘hide’ in the phase space of the relative variables. The right-hand side of the combinations

$$\begin{aligned}
 A : \quad & \left(k + \frac{1}{2}P\right)^2 = (p_1 + p_2)^2, \quad \left(k - \frac{1}{2}P\right)^2 = (-p_3 - p_4)^2 \\
 B : \quad & \left(q + \frac{1}{2}P\right)^2 = (p_1 + p_3)^2, \quad \left(q - \frac{1}{2}P\right)^2 = (-p_2 - p_4)^2 \\
 C : \quad & \left(p + \frac{1}{2}P\right)^2 = (p_1 + p_4)^2, \quad \left(p - \frac{1}{2}P\right)^2 = (-p_2 - p_3)^2
 \end{aligned} \tag{4.1.1}$$

is the total momentum squared of two quark/antiquark lines respectively. Two-body bound states will appear whenever these ‘subclusters’ go on-shell.

Putting the lowest pseudo-scalar mass  $m_\pi$  for combination  $A$  and  $B$  and the lowest scalar diquark mass  $m_D$  for combination  $D$  into eq. (4.1.1), yields three threshold conditions:

$$\begin{aligned} -m_\pi^2 &= p^2 + \frac{1}{4}P^2 \pm i\eta_1 \\ -m_\pi^2 &= q^2 + \frac{1}{4}P^2 \pm i\eta_2 \\ -m_D^2 &= k^2 + \frac{1}{4}P^2 \pm i\eta_3 \end{aligned} \quad (4.1.2)$$

Whenever any of these equation is fulfilled for  $p^2 \geq 0, q^2 \geq 0$  or  $k^2 \geq 0$ , the *dressing functions* of the tetraquark acquire poles at this location. The quantities  $\eta_{1,2,3}$  are the angles between the relative momenta  $p, q, k$  and the total momentum  $P$ , see eq. (3.2.9).

Focusing on the condition for  $p^2$ , eq. (3.2.21) can be inserted into eq. (4.1.1) and can be solved for the variable  $\hat{r}_p$ :

$$\hat{r}_p^{sing} = \frac{\frac{3}{4S_0}(-m_\pi^2 + \frac{1}{4}M^2 + 2i\Gamma \pm i\eta_1) - 1}{f_p(\varphi)} \quad (4.1.3)$$

$$f_p(\varphi) := r_{max}(\varphi) \cos(\varphi + \frac{2\pi}{3}) \quad (4.1.4)$$

$$P^2 = M^2 + 2i\Gamma. \quad (4.1.5)$$

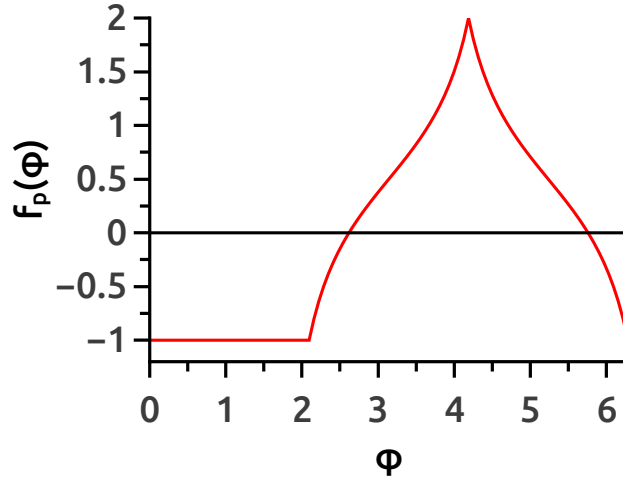


**Figure 4.1.:** Function  $f_p(\varphi)$  found in eq. (4.1.3).

The function  $f_p(\varphi)$  has the value  $-1$  in the range  $\varphi \in [0, \frac{2\pi}{3}]$ , see figure 4.1. For generalities sake we introduced the width  $\Gamma$  which is the imaginary part of  $P^2$ , the complex T-matrix pole of the tetraquark.

Investigating  $\hat{r}_p^{sing}$  further, there are two general cases that can be distinguished:

$M < 2m_\pi$  For simplicities sake we assume that  $\Gamma = 0$  and  $\eta_1 = 0$ . The numerator is always negative with magnitude larger than 1. Because  $f_p \geq -1$ , the following inequalities hold:

$$\begin{aligned} \hat{r}_p^{sing} &> 1 \quad \text{if} \quad f_p < 0 \\ \hat{r}_p^{sing} &< 0 \quad \text{if} \quad f_p > 0. \end{aligned} \quad (4.1.6)$$

If  $\eta_1 \neq 0$ ,  $\hat{r}_p^{sing}$  has always non-zero imaginary part, and thus is never inside the doublet-triangle.

$M > 2m_\pi$  Take for example  $f_p = -1$  and  $\mathcal{S}_0 = \frac{4}{3}$ . The numerator is now negative but with a magnitude smaller than 1. Because  $f_p = -1$ , the pole at  $\hat{r}_p^{sing}$  is now inside the phase space triangle:

$$0 < \hat{r}_p^{sing} < 1 \quad (4.1.7)$$

It is clear that for a  $f_p \neq -1$  and  $\Gamma \neq 0$ , one can always find a  $\varphi \in [0, 2\pi]$  and a  $\mathcal{S}_0 \geq 0$  so that  $0 \leq \hat{r}_p^{sing} \leq 1$  holds.

The appearance of poles in the phase space of  $\hat{r}$  for  $M > 2m_\pi$  is the first evidence that the system exhibits thresholds.

## 4.2. Numerical evidence - Shape of amplitudes

Besides this analytical reasoning, the emergence of poles can also be seen by solving the bound-state equation and investigating the amplitudes, see figure 4.2. These figures were calculated at the two-pion threshold ( $M^2 = 0.26 GeV$ ,  $m_\pi = 0.138$ ). To resolve the structure of the tetraquark amplitude inside the doublet triangle, a larger number of points along the  $\varphi$  (16)- and  $r$ - direction (20) were used. As a side remark we mention that a simple power method to solve the eigenvalue problem was not sufficient and the use of the advanced library SLEPc [75] was necessary to get any result at all. There are three distinctive features that can be interpreted physically.

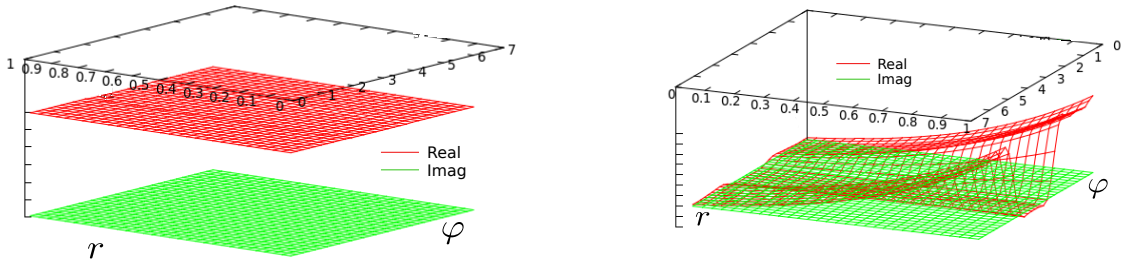


**Figure 4.2.:** Dominant  $\gamma_5 \otimes \gamma_5$  amplitude along the  $\varphi - r$  direction. The left figure at  $\mathcal{S}_0 \approx 10^{-5} GeV$  shows no structure. In the right figure at  $\mathcal{S}_0 \approx 0.1 GeV$ , the bend of the amplitude towards the boundary is attributed to the close-by poles. The discontinuity in the  $\varphi$ -direction is caused by the difference between diquark and pion mass.

- The first feature is the bending of the amplitude towards  $r = 1$ , as can be seen in the right panel of figure 4.2. This is attributed to a pole close-by.
- The second feature is the (almost) discontinuity along the  $\varphi$  direction, also seen in figure 4.2. Geometrically, the discontinuity appears at angles  $\varphi$  where the meson side meets the diquark side:  $\varphi = 2/3\pi, 4/3\pi$ . This sharp drop in the amplitude can be understood from the mass difference of the pion ( $m_\pi \approx 0.138 \text{ GeV}$ ) and the diquark  $m_D \approx 0.88 \text{ GeV}$ . The pole of the diquark is further away and the amplitude does not ‘feel’ the influence of the diquark pole as strongly as the pion pole.
- The amplitude is essentially flat for small  $\mathcal{S}_0$ , see left panel of figure 4.2. All potential poles that could give rise to a more complicated structure are far outside of the doublet triangle: ( $\hat{r}_p^{sing} \gg 1$ ).

In light of the threshold condition derived beforehand, these aspects are perfectly understandable and a welcomed physical feature. Unfortunately, these poles introduce a lot of numerical problems and restrict the actual calculation to masses below the two-pion threshold.

We want to mention, that one can naively calculate above threshold. However, going beyond the threshold worsens the numerical stability. The eigenvalue spectrum acquires complex, grid dependent contributions; additionally the spectrum becomes dense and the overall convergence is bad. Thus all further calculations will be restricted to masses below threshold.

**Remark** It is interesting to note that the formation of two-body clusters seems to be a feature of the phase-space, and more precisely of the doublet-triangle, and not so much a feature of the tensor-decomposition. That means that the two-pion poles, seen as bending of the amplitude towards the boundary of  $\hat{r}$ , appear in the  $\gamma_5 \otimes \gamma_5$ ,  $\gamma^\mu \otimes \gamma^\mu$ ,  $\mathcal{C}\gamma_5 \otimes \gamma_5\mathcal{C}^T$  etc. amplitudes. This seems counter intuitive to the naive picture, that the tensor-structure should correspond to the poles, e.g. the  $\gamma_5 \otimes \gamma_5$  structure should contain the  $\pi - \pi$  poles, the  $\gamma^\mu \otimes \gamma^\mu$  the  $\rho - \rho$  poles and so on. However, taking into account Fierz-transformations explains why the poles appear in all tensor structures. All amplitudes in the different decompositions ( $D, M_I, M_{II}$ ), see sec. 3.5, are related via Fierz-transforms. Poles that appear for example in the  $\gamma_5 \otimes \gamma_5$  amplitude in the ( $M_I$ ) decomposition will be mixed via Fierz-transformation into the  $\gamma^\mu \otimes \gamma^\mu$  and  $\gamma_5 \otimes \gamma_5$  structures in the ( $M_{II}$ ) decomposition. The pole position is not changed because the Fierz-transformation acts only on the Dirac-indices of the amplitude and not on the phase space of the dressing functions.

Besides the Dirac-structure, the same argument holds for the colour structure: The poles appearing in the amplitudes in the three different *colour*-decompositions ( $D, M_I, M_{II}$ ) are the same. As for the Dirac-tensor case, the colour amplitudes are related via Fierz-transforms that only act on the colour indices.

In the case of the flavour structure, there is an important complication. The kernel explicitly depends on the flavour when taking into account the quarks that are also part of the kernel.

To investigate how the flavour structure is related to the pole structure, we look at the  $a_0(980)$  flavour amplitude [8]:

$$\begin{aligned}
a_0 \propto & |ds\bar{d}\bar{s}\rangle - |sd\bar{d}\bar{s}\rangle + |ds\bar{s}\bar{d}\rangle \\
& + |us\bar{s}\bar{u}\rangle - |sd\bar{s}\bar{d}\rangle - |su\bar{u}\bar{s}\rangle \\
& + |us\bar{u}\bar{s}\rangle - |su\bar{s}\bar{u}\rangle.
\end{aligned} \tag{4.2.1}$$

Taking the red printed part as example, we can make the following observations: Combining the flavour indices (1, 3) and (2, 4)

$$\overline{\boxed{d\bar{s}ds}}, \tag{4.2.2}$$

we could associate this amplitude with an  $\pi\eta$ . From eq. (4.1.1) we know that poles in the momentum combination  $(p_1 + p_3)^2 = -m_\pi^2$  and  $(p_2 + p_4)^2 = -m_\eta^2$  will appear on the right side of the doublet triangle (figure 3.3). But we could also combine the flavour indices (1, 4) and (2, 3),

$$\overline{\boxed{d\bar{s}d}s}, \tag{4.2.3}$$

and associate the same flavour amplitude with a  $KK$ . But from eq. (4.1.1) we already know that poles in the momentum combination  $(p_1 + p_4)^2 = -m_K^2$  and  $(p_2 + p_3)^2 = -m_K^2$  will appear on the left side of the doublet triangle. The third way to combine the flavour indices is to combine two quarks and two anti-quarks:

$$\overline{\boxed{d\bar{s}}}\boxed{ds}. \tag{4.2.4}$$

This amplitude is subsequently identified with a diquark-diquark bound state and the poles in the momentum combination  $(p_1 + p_2)^2 = -m_{D_{ds}}^2$  and  $(p_3 + p_4)^2 = -m_{D_{ds}}^2$  will appear on the upper side of the doublet triangle.

We finally arrive at the following picture: Each flavour structure has its own dressing function that features meson poles and diquark poles which are located at the corresponding site of the doublet triangle. Charge conjugation operations and quark exchange operations relate all flavour amplitude to each other by exchanging the poles. For example  $|ds\bar{d}\bar{s}\rangle$  turns under a  $P_{12}$  transformation up to minus sign into the  $|sd\bar{d}\bar{s}\rangle$  amplitude by exchanging the  $KK$  poles on the left side of the triangle with the  $\pi\eta$  poles on the right side and vice versa.

### 4.3. Numerical evidence - Eigenvalue spectrum

Besides the the shape of the amplitudes, the eigenvalue spectrum and its dependence on the radial variable  $\hat{r}$  was also investigated. In order to do a systematical study, we calculated the first three eigenvalues of the scalar tetraquark for a light quark  $m_q = 0.00405 \text{ GeV}$  and a heavy quark  $m_Q = 0.89 \text{ GeV}$ . The tetraquark mass in both cases was kept below the two- $m_\pi/m_{\eta_c}$  threshold. To investigate the  $\hat{r}$ -boundary effects we used three different setups. The first setup employed a larger number of points (14) along the  $\hat{r}$  direction over the full range  $I = [0, 1]$ . In the second one, the radial variable  $\hat{r}$  was restricted to the interval  $I = [0, 0.5]$ . A constant extrapolation of the value at the boundary was used whenever  $\hat{r} \notin I$ . This setup is meant to estimate the effect of excluding the boundary region in a crude ad-hoc fashion.

In the third setup, the interval was restricted to  $I = [0.8, 1]$  to over-emphasize the boundary region with the same extrapolation scheme as in setup two.

We want to stress that these setups are not to be taken as full-fledged calculations to estimate the tetraquark mass, but as means to estimate the gross effect of two-body bound-state correlations on the tetraquark (mass). The treatment in terms of the three described setups may be crude but in the light of the findings in the previous section, that two-body bound-state correlations hide at the boundary, we think it justified to do so, and that the results can be used to get a rough idea of how these effects influence the tetraquark.

#### 4.3.1. Light quarks

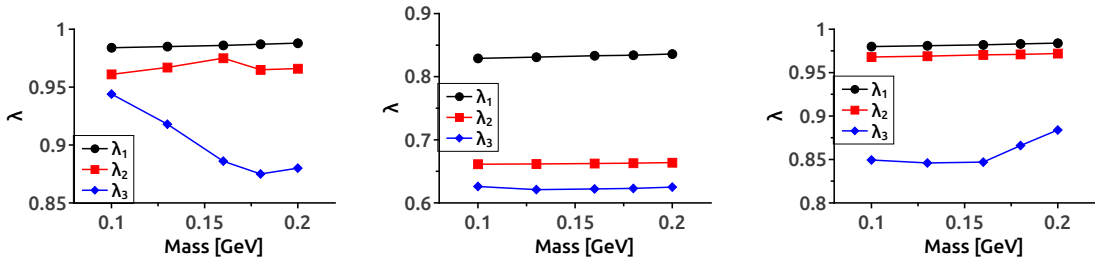


**Figure 4.3.:** *Left figure:* Eigenvalue curve  $\hat{r} \in [0, 1]$ . *Middle figure:* Eigenvalue curve for probing  $\hat{r} \in [0, 0.5]$ . *Right figure:* Eigenvalue curve for probing  $\hat{r} \in [0.8, 1]$ . All three setups used a light quark ( $m_q = 0.00405 \text{ GeV MeV}$ ).

The results for the setups that used light quarks can be seen in 4.3. In the following we will provide a detailed analysis of each setup:

**Setup I** The left panel shows the eigenvalue curve for the first setup. The eigenvalue corresponding to the ground state is quite flat and has a small imaginary part. The second eigenvalue is quite close and even decreases, as is the third one. This is not the typical behavior of the eigenvalue spectrum of the Maris-Tandy model in the meson sector [85]. The magnitude of the ground state eigenvalue is close to 1, and using a linear extrapola-

tion indicates a tetraquark mass of somewhere around  $0.480 \text{ GeV}$ .

**Setup II** The second panel shows the result for the second setup. In this setup the effect of exclusion of the boundary  $\hat{r}$  was investigated. The separation of the eigenvalues is much more pronounced. This immediately had also a positive effect on the convergence rate of the eigenvalue equation. However, the biggest difference to setup I is the extrapolated mass. Using a linear extrapolation for the largest eigenvalue, we read off a mass of about  $2.6 \text{ GeV}$ . This is much heavier than the mass obtained from setup I and a clear indicator of the importance and influence of the boundary effects included in setup I.

**Setup III** In the third panel we see the effect when over-emphasizing the boundary region. The first two eigenvalues are as close as in setup I, but at least the third one is not decreasing anymore. The convergence of the system was comparable with setup II. The interesting aspect is again the extrapolated mass of around  $0.6 \text{ GeV}$ , which is larger than in setup I, but in the same ball park and definitely smaller than the mass of setup II.

**Summary** The main conclusion is the importance of the two-body correlations. Without these, the mass of the tetraquark rises well above  $1 \text{ GeV}$ . Including them pushes the mass down to values well below  $1 \text{ GeV}$ . This is also the mass-region where the experimental value for the  $f_0(500)$  is located [14]. We thus conclude that the formation of pions in the  $0^{++}$ -tetraquark is of attractive nature and the dominant mechanism to ensure a light mass of the tetraquark. The diquark correlation, as could already be seen from the shape of the amplitude in sec. 4.2, plays a minor role. This is quite expected, when taking the large mass ( $m_D = 0.88 \text{ GeV}$ ) of the diquark into account. This is also in line with previous investigations where the tetraquark was modeled as a bound-state of off-shell pions [99] and the contributions of the diquark was found to be sub-leading.

### 4.3.2. Heavy quarks

A similar investigation was performed for a quark in the charm quark region with a current mass of  $m_q = 0.89 \text{ GeV}$ . We choose the same prescription to investigate the influence of the boundary effects and the results are depicted in figure 4.4.

**Setup I** The left panel shows the eigenvalue curve for the first setup. The eigenvalue corresponding to the ground state is much better separated from the second eigenvalue than in the light quark case. Also the curve rises more steeply. Employing a linear extrapolation we extracted a mass of  $5.3 \text{ GeV}$  for the tetraquark.

**Setup II** The second panel shows the result for the second setup. In this setup the effect of exclusion of the boundary  $\hat{r}$  was investigated. In comparison with the light quark case,

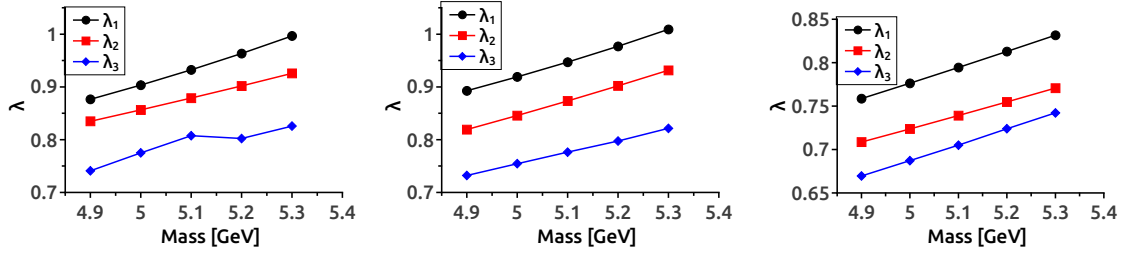


**Figure 4.4.:** *Left figure:* Eigenvalue curve  $\hat{r} \in [0, 1]$ . *Middle figure:* Eigenvalue curve for probing  $\hat{r} \in [0, 0.5]$ . *Right figure:* Eigenvalue curve for probing  $\hat{r} \in [0.8, 1]$ . All three setups used a heavy quark ( $m_q = 0.89 \text{ GeV}$ ).

the difference between setup I and II is not so pronounced when looking at the separation of eigenvalues. And we also do not see a mass shift as in the light quark case. The mass reads off as  $5.3 \text{ GeV}$ , the same value as in setup I.

**Setup III** In the third panel we see the effect when over-emphasizing the boundary region. The first and second eigenvalues are slightly further apart than the eigenvalues in setup I and II. The linear extrapolated mass is around  $6.2 \text{ GeV}$ . This is a clear shift of the mass to higher values, and a exactly opposite to setup III in the light quark case.

**Summary** Comparing the light and heavy quark case, we see two distinctions.

The heavy quark case is numerically much better behaved. The eigenvalues are better separated and the slope of the curves is noticeable compared with the light quark case. This can be readily understood from the mass of the corresponding two-body bound-states. In the light quark case, the threshold is defined by two times the mass of the pion,  $2m_\pi = 0.274 \text{ GeV}$ . This is very close to the  $\hat{r}$  boundary, even below threshold and for moderately small  $\mathcal{S}_0$ . In the heavy quark case, the threshold is determined by two times the  $\eta_c$  mass,  $2m_{\eta_c} = 5.9 \text{ GeV}$ . For the same  $\mathcal{S}_0$ , the pole is further away from the boundary and does not cause so many problems as in the light quark case.

However, the biggest difference is the shift of the mass. Setup II was employed to determine the effect of neglecting the boundary effects. In the light quark case this leads to an increase of the mass. In the heavy quark case this is reversed. The same inversion is seen when switching off the boundary effects. In the light quark case, the mass is not changing by much but in the heavy quark case the over-emphasizing of the boundary effects leads to a much heavier tetraquark.

This difference could be related to the role of the diquark. In the heavy quark case, the diquark is not so much heavier than the  $\eta_c$ , so that the diquark influence on the boundary is not so small. If the diquark produces a repulsive effect, such an effect would be stronger in the heavy quark case, because the mass of  $\eta_c$  and the scalar diquark are comparable. Another explanation could be, that the boundary effects in total do not play the dominating role as they do in the light quark case, because both  $\eta_c$  and the diquark are quite heavy. This conclusion is bolstered by the observation that apparently the mass of the

heavy tetraquark is determined by the opposite boundary  $\hat{r} = 0$ , where pole effects below threshold are suppressed. In physical terms this could be boldly interpreted as a hint that in the light quark sector the tetraquark is more a molecule like object, where the physics is determined by the pion-pion correlations inside the tetraquark, whereas in the heavy quark sector the tetraquark behaves more like a four-quark core with sub-leading  $\eta_c - \eta_c$ /diquark-diquark correlations. However, as mentioned before, these observations should be taken with a grain of salt because the numerical means to distill them are still quite crude.

Concluding this numerical section we want to make a remark regarding the dense and complex eigenvalues that afflicted this work for a long time. In the literature continuous spectra and complex eigenvalues are not unknown. The continuous spectra in QED plagued the Bethe-Salpeter approach from the very start [115] and was coined the ‘Goldstein problem’. Also complex eigenvalues were a topic that sparked much debate about the physical significance of such solutions in the (spinor-spinor)-BSE [116].

Generically, continuous spectra are connected with some critical value for the coupling constant of the system and complex eigenvalues are identified with abnormal states, corresponding to unphysical excitations in the relative time of the two bound particles. See refs [117, 118, 119] and references therein for a thorough discussion. Furthermore ref. [120] proves that a divergence of the Bethe-Salpeter amplitude in the infrared causes a continuous spectrum that can ‘hide’ an additional discrete spectrum.

All the examples in literature that investigate the spectral properties of BSEs in the ladder-kernel approximation treat simplified *two*-body problems. There exists no investigation of three- and four-body problems.

In the light of our numerical findings, we draw the heuristic conclusion, that a close-by (dynamical) pole in the BSE-amplitude pollutes the numerics and leads to potential spurious complex eigenvalues and a squeezing of the spectrum and not any of the above mentioned cases found in literature. Additionally, with the dynamic pole ansatz that will be introduced in the next section to handle the two-body correlations below threshold, the ground state eigenvalue becomes real and the second eigenvalue is pushed away. The spectrum is still not as clean as in the two-body case but we think this is mostly attributed to the larger phase-space (nine-dimensional) and the larger tensor-basis (256 structures) which increases the potential numerical noise.

#### 4.4. Pole ansatz

Having shown the numerical and phase-space arguments for the dynamical emergence of threshold effects in the form of two-body poles, we will proceed and construct a suitable parametrization for this poles to improve the numerical stability. We choose the following parametrization:

$$f(\bar{\Omega}, \hat{r}) = a(\bar{\Omega}) + \frac{b(\bar{\Omega})}{(\hat{r} - \hat{r}_+^s)(\hat{r} - \hat{r}_-^s)} \quad (4.4.1)$$

$$\hat{r}_\pm^s = -\frac{3}{4\mathcal{S}_0} \left( -m_\pm(\varphi)^2 - \frac{1}{4}P^2 \pm \Lambda_P(\varphi) \right) + 1 \quad (4.4.2)$$

$$m_\pm(\varphi) = \begin{cases} m_{ps,1}^\pm & \text{if } \varphi \in [0, \frac{2\pi}{3}] \\ m_D^\pm & \text{if } \varphi \in [\frac{2\pi}{3}, \frac{4\pi}{3}] \\ m_{ps,2}^\pm & \text{if } \varphi \in [\frac{4\pi}{3}, 2\pi] \end{cases} \quad (4.4.3)$$

$$\Lambda_P(\varphi) = \begin{cases} P \cdot p & \text{if } \varphi \in [0, \frac{2\pi}{3}] \\ P \cdot k & \text{if } \varphi \in [\frac{2\pi}{3}, \frac{4\pi}{3}] \\ P \cdot q & \text{if } \varphi \in [\frac{4\pi}{3}, 2\pi] \end{cases}. \quad (4.4.4)$$

We will give the reasons and justifications for this particular choice in the following paragraphs.

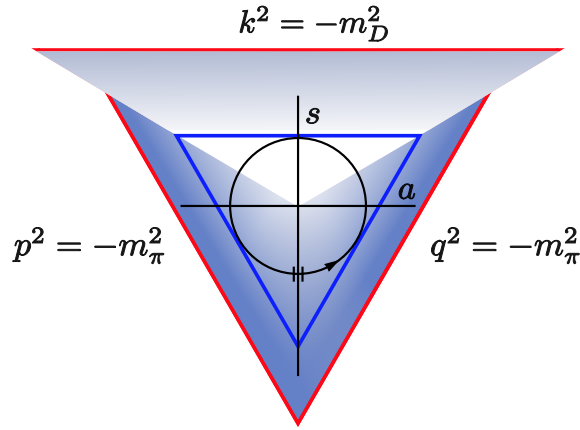


**Figure 4.5.:** Position of the two-body poles in the doublet-triangle for fixed  $\mathcal{S}_0$  and  $\Lambda_P(\varphi) = 0$ . The physical region is bounded by the blue triangle, the poles are located at the red lines and the shaded area corresponds to the sector the pole contributes to.

**Segmentation** In eq. 4.1.3, the pole of a two-body bound-state is defined for the whole doublet-triangle and therefore for  $\varphi \in [0, 2\pi]$ . Because we are mostly interested in the effects of the bound-state pole at the boundary  $\hat{r} = 1$ , we restrict the poles to the region in  $\varphi$  where  $f_{p,q,k} = -1$ . This is precisely the case for the segmentation chosen in eq. (4.4.3). Each segment, which coincides with the sides of the doublet-triangle, is associated with bound-states in the momentum combinations  $A, B, C$  of eq. (4.1.1). A graphical representation of this segmentation is shown in figure 4.5. This segmentation coincides also with our observation that the amplitude develops an almost discontinuous jump between the segments, see figure 4.2. For a tetraquark containing more than one quark species, for example the  $a_0(980)$ , we pick one representative of the flavour amplitude and fix the

masses  $m_{ps,1}^\pm, m_{ps,2}^\pm, m_D^\pm$ . In the case of the  $|ds\bar{d}\bar{s}\rangle$  as an example, this yields:

$$\begin{aligned}
& |ds\bar{d}\bar{s}\rangle : \\
& m_{ps,1}^+ = m_\pi, \quad m_{ps,1}^- = m_{s\bar{s}} \\
& m_{ps,2}^+ = m_K, \quad m_{ps,1}^- = m_K \\
& m_D^+ = m_{D_{ds}}, \quad m^- = m_{D_{\bar{u}\bar{s}}}.
\end{aligned} \tag{4.4.5}$$

All other elements of the flavour amplitude are related to the chosen representative by  $S_4$ -permutations.

**Parametrization** The parameters  $a(\bar{\Omega})$  and  $b(\bar{\Omega})$  depend on each Lorentz invariant *except*  $\hat{r}$ , denoted by  $\bar{\Omega}$ . That means the amplitude is defined on a nine-dimensional grid with two points in the  $\hat{r}$ -direction. The constants  $a(\bar{\Omega}), b(\bar{\Omega})$  can always be reconstructed for fixed  $\bar{\Omega}$  from the dressing-function values at these two points. We choose two points close to the boundaries 0 and 1. The regular part, parametrized by  $a$ , is mostly determined by the value close to  $\hat{r} = 0$  and the singular part, parametrized by  $b$ , is determined by the value close to  $\hat{r} = 1$ . This parametrization can easily be generalized by replacing the constants  $a, b$  by polynomials in  $\hat{r}$  and by adding more singular terms for each possible bound-state in the two-body sub-cluster. Because the amplitude will be dominated by the lowest laying two-body bound-states and its pole, the restriction to one pole structure is a reasonable truncation. A further advantage of this pole ansatz is the reduction of points needed to represent the tetraquark amplitude.

Besides numerical stability, the pole-ansatz has the advantage to be interpreted in physical terms. This parametrization can be understood as decomposition into a pure four-quark amplitude, captured by  $a(\bar{\Omega})$ , and a molecular like meson-meson/diquark-antidiquark part, encoded in  $b(\bar{\Omega})$ .

**Analytical structure** The simplest choice for a singular function is a simple pole, with a residue  $b(\bar{\Omega})$ :

$$\frac{b(\bar{\Omega})}{(\hat{r} - \hat{r}_+^s)(\hat{r} - \hat{r}_-^s)}. \tag{4.4.6}$$

We chose the product of two poles instead of the the sum of two poles in each segment. This reduces the number of singular terms, and therefore the number of dynamical parameters. Physically, this can be motivated by the assumption that in a tetraquark, the meson-meson correlations, represented by a product, should be more dominant than the single meson/diquark-correlations, associated with a sum of the form  $\frac{1}{\hat{r}^s - \hat{r}}$ .

## 5. Results

After having laid the the foundations for calculating the tetraquark in the four-body picture, we come to the presentation of our results. In the first section we investigated the dependence of the tetraquark mass on the various Lorentz invariants. The results of chapter 4 are also repeated in the first section. The result for the tetraquark mass curve are presented and the values calculated for  $\kappa$  and  $a_0/f_0$  tetraquarks are provided in the last two sections.

### 5.1. Comparing Lorentz invariants

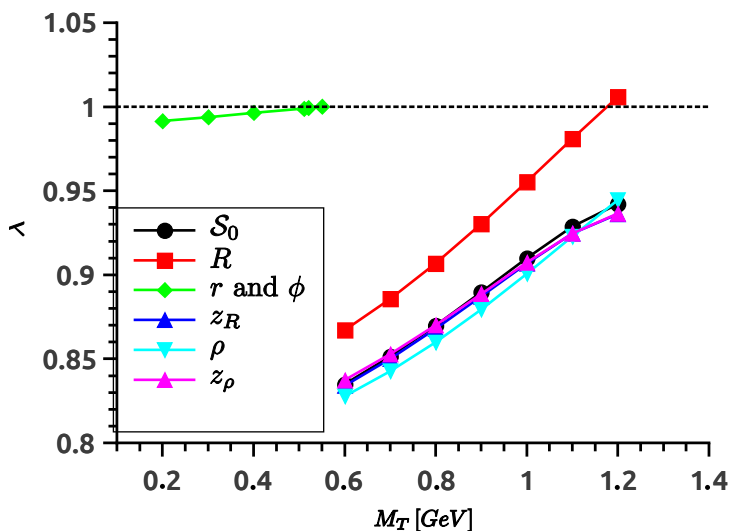


**Figure 5.1.:** Eigenvalue  $\lambda$  in dependence of the different Lorentz invariants as functions of the tetraquark mass  $M_T$ . The mass  $M_T$  at which an eigenvalue crosses the dashed line  $\lambda = 1$  corresponds to the bound state mass.

The scalar dressing functions of the tetraquark depend on the nine Lorentz invariants of chapter 3.2. Because of the large number of dimensions  $d = 9$  it is not feasible to use a large number of points for all of them. For example, using a cartesian grid with 10 points for each Lorentz invariant, the number of grid points for just one dressing function would be of the order of  $10^9$  points. In order to reduce the size of the problem we had to drastically reduce the number of points in some directions. To gauge the numerical error of such a truncation, we first investigated the dependence of the eigenvalue on each of the

nine Lorentz invariants separately.

To investigate each Lorentz invariant separately, we switched on one Lorentz invariant after the other by using a 12 interpolation rule in that specific direction and using one-point rules for the rest of the Lorentz invariants. The only exception was the variable  $\mathcal{S}_0$  which was always taken with 20 points, because otherwise the BSE did not converge. We also note that for the variables  $\Phi_R$  and  $\Phi_\rho$  a one-point rule was used in all cases. The same calculation for 16 points along the tested Lorentz invariants was repeated, and the deviations found to be less than five percent. A similar result was found for the variation of the points along the  $\Phi_R$  and  $\Phi_\rho$  direction.

Employing the construction principle for the complete nine-dimensional interpolation rule of chapter 3.7, the tetraquark BSE was solved for a range of tetraquark masses  $M_T$  and the largest eigenvalue was tracked. The mass  $M_T$  at which the eigenvalue curve (or its linear extrapolant) crosses the dashed line corresponds to the mass of the bound state. The final result for a current quark mass of  $m_q = 0.00405 \text{ GeV}$  is shown in figure 5.1. The legend on the left side of the figure denotes the Lorentz invariant(s) investigated. As stated above, all other Lorentz invariants except  $\mathcal{S}_0$  are approximated by one-point rules.

The relevance of a Lorentz invariant can be deduced from the deviation between its associated curve and the curve that contains the  $\mathcal{S}_0$  variable only. Because the crossing of the ‘1’ is associated with a bound-state, an increased eigenvalue directly corresponds to a lowering of the bound-state mass and a decrease of the eigenvalue raises the bound-state mass.

It is immediately clear that the  $r$ ,  $\varphi$  and  $R$  variables are the most important ones because the eigenvalue curves change considerably compared to the  $\mathcal{S}_0$  curve. The other variables are of lesser importance, as can be seen from the fact that their curves lay almost on-top of the  $\mathcal{S}_0$  curve.

Comparing the  $r - \varphi$  and the  $R$  curve, we make the following observations:

- The variables  $r$  and  $\varphi$  are the most important ones. They strongly reduce the tetraquark mass leading to a *light*  $\sigma$ -tetraquark and change the shape of the eigenvalue curves considerably. These variables are connected with pion-pion and diquark-diquark correlations, emerging as poles in the doublet triangle, as was elaborated in chapter 4. Because the influence of these variables is so large compared to the other ones, we think it justified to state that our calculations support the notion that the  $\sigma$  tetraquark is dominantly a molecular state, in the sense that the two-body correlations play the dominant role. At this point we want to stress, that by ‘molecular’ we mean only the dominance of two-body correlations within the phase space of the *four*-body tetraquark amplitude. We do not make any statement about the size of the object or about effective forces between the mesons and diquarks which are usually used to differentiate the molecular from the four-quark picture.
- Extrapolating the eigenvalue curves of the other variables, including  $R$ , yields much

heavier masses for the  $\sigma$ , above or around  $1\text{ GeV}$ . Because an exclusion of the  $r, \varphi$  variables amounts to an exclusion of any two-body correlations, the only poles that can dominate the tetraquark are the (complex) quark poles. As we discussed in chapter 3.2.2, these quark poles are connected with the triplet  $\mathcal{T}_0$  and will reside outside the associated (deformed) tetrahedron. Because the surface of this tetrahedron is probed for  $R \approx 1$ , it is conceivable that the four-quark correlations will show up when taking into account the Lorentz invariant  $R$ . Similar to the interpretation of the meson-meson correlations as the molecular part of the tetraquark, we identify the four-quark correlations with a ‘four-quark’ part.

We conclude that the two-body correlations for an equal mass tetraquark do not only play the dominant role but also favour a light  $\sigma$  below  $1\text{ GeV}$ , whereas the four-quark correlations are only subleading and feature a heavy tetraquark above  $1\text{ GeV}$ . To further support this conclusion, we also included  $r, \varphi$  and  $R$  at the same time. The resulting eigenvalue curve was very close to the case of  $r$  and  $\varphi$  only. Because the inclusion of all three variables  $r, \varphi, R$  is part of the main result that is presented in chapter 5.2, this case was omitted from figure 5.1.

Additionally, we established that all other Lorentz invariants except  $r, \varphi, R$  and  $S_0$  can be approximated by one point rules without yielding a too large error.

Because the pion poles, or meson poles in general, spoil the calculation even below threshold, all following calculations included the variables  $r$  and  $\varphi$  by the pole ansatz found in chapter 4.4.

The main results of chapter 4 are repeated and put into context with the rest of our findings.

In chapter 4 we found out that the four-body tetraquark dressing functions feature poles inside and outside of the doublet triangle that represents the variables  $r, \varphi$ . The pion poles can be seen graphically as rise of the dressing function towards the border of the triangle. Figure 5.2 shows a contour plot of the dominant  $\gamma_5 \otimes \gamma_5$  dressing function in the doublet triangle for an  $S_0$  of about  $0.1\text{ GeV}$ .

The dark shaded area at the left and right side of the triangle, the so-called meson-sides, indicate that the dressing function ‘feels’ a structure outside of the triangle. This structure was identified in chapter 4 with pion poles. On the upper side of the triangle, the diquark side, the magnitude of the dressing function is much smaller. The difference of the magnitude between meson and diquark sides is easily conceivable from the mass difference of the pion and the diquark. The diquark pole is further way from the border of the triangle, yielding a smaller rise than the pion poles which are much closer to the border.

As early as chapter 4 it was argued that this behaviour of the amplitude close to the border justifies a pole approximation, leading to an improved convergence of the BSE. But besides the numerical stabilization, the poles are physically relevant:

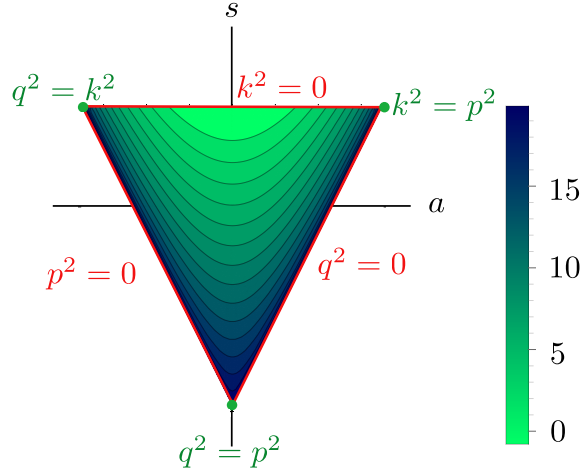


**Figure 5.2.:** Contour plot of the dominant  $\gamma_5 \otimes \gamma_5$  dressing function in the doublet triangle. The darker the plot, the larger is the modulus of the dressing function. The left and right side are called the meson sides because pion poles appear at that side of the triangle, whereas the upper side is called the diquark side.

Meson-meson and diquark-diquark correlations are an intrinsic part of the four-body tetraquark amplitude and manifest themselves as poles in the doublet triangle of the tetraquark. In chapter 4.3.2 we investigated the influence of these meson and diquark poles on the mass spectrum of the scalar tetraquarks, by including and excluding the boundary region of the doublet triangle. We found that the inclusion of the boundary yielded a smaller tetraquark mass in the case of light  $u/d$  quark masses, whereas in the case of quark masses in the charm region, the boundary effects increased the mass of the tetraquark.

Besides the difference in quark masses, the mass of the resulting pseudo scalar meson and scalar diquark distinguishes both cases from each other.

In the case of light quarks, the mass of the pseudo scalar reads  $m_\pi = 0.138 \text{ GeV}$  and the mass of the scalar diquark  $m_D = 0.789 \text{ GeV}$ . The pion pole is much closer to the boundary than the diquark one and the effect of the diquark is expected to be small. However, in the case of the charm quark, the scalar diquark has a mass  $m_D$  of about  $3.5 \text{ GeV}$ , comparable with the mass of the pseudo-scalar meson with a mass  $m_{\eta_c}$  of about  $2.95 \text{ GeV}$ . Because *both* poles have a comparable distance to the boundary, the effect of the diquark is presumed to be larger.

Because the inclusion and exclusion of the boundary involves cutoffs in the doublet triangle and relies on simple constant extrapolations (see chapter 4.3), a statement cannot be made that strong diquarks-diquark correlations *in general* lead to higher tetraquarks masses and strong pseudoscalar-pseudoscalar correlations lead *in general* to lower masses, but the results are a strong indication in this direction.

Finally, we conclude that all effects caused by two-body correlations scale with the mass of the associated bound states. Therefore, we can speculate with some confidence that in the case of the  $\sigma$ , the influence of the  $\rho$ -meson in form of poles outside of the doublet

triangle is eclipsed by the much closer pion poles. However, in the case of the all charm tetraquarks this argument is expected to be weaker because the mass of the  $\eta_c$  and the  $J/\Psi$  are comparable.

## 5.2. Mass curve

$m_q[GeV]$	$m_\pi[GeV]$	$m_D[GeV]$	$2m_\pi[GeV]$	$m_T[GeV] \text{ lin}$	$m_T[GeV] \text{ quad}$
0.00405	0.138	0.789	0.276	0.335	0.361
0.035	0.428	0.987	0.856	0.891	0.878
0.065	0.593	1.14	1.186	1.21	1.219
0.105	0.77	1.33	1.54	1.6	1.6
0.2	1.11	1.63	2.236	2.352	2.362
0.3	1.42	1.99	2.84	3	3.09
0.4	1.71	2.28	3.42	3.637	3.725
0.5	2	2.57	4	4.251	4.395
0.55	2.13	2.716	4.26	4.34	4.61
0.6	2.25	2.85	4.512	4.731	5.017
0.625	2.32	2.91	4.64	4.9	4.83
0.65	2.38	2.975	4.76	4.83	4.9
0.7	2.51	3.09	5.02	5.037	5.101
0.89	2.95	3.5	5.9	5.771	5.771

**Table 5.1.:** Tabulated values of figure 5.3. The last two columns contain the tetraquark masses obtained by quadratic and linear extrapolation respectively. See the appendix A.1 for the plots.

We now come to the main result of this work, the quark mass dependence of the tetraquark mass, as depicted in figure 5.3. We used the pole ansatz from chapter 4.4, and used a grid with 20 points in the  $S_0$  direction and 12 points in the  $R$  direction. All other Lorentz invariants were approximated by one-point rules, which, according to the discussion in chapter 5.1, introduces only a small error but reduces the demand on memory and computation time noticeably. For the integration we used a Gauss-Legendre rule with 30 points in the radial direction and 10 points in all three angular directions.

The two-pion threshold puts a limit on the tetraquark mass that can be used as input for the BSE. It turned out that for a large range of quark masses the tetraquark is heavier than two-pions, so that it was necessary to extrapolate the eigenvalue curves below threshold to higher quark masses. We follow the prescription of eq. (2.8.4) and extrapolate the quantity

$$f_\lambda(M_T^2) = \frac{1}{\lambda(M_T^2)} - 1, \quad (5.2.1)$$

with  $\lambda$  representing the eigenvalue curve of the BSE as function of  $M_T^2$ . To obtain the bound state mass, we extrapolate the quantity in eq. (2.8.5) as function of  $M_T^2$  and search

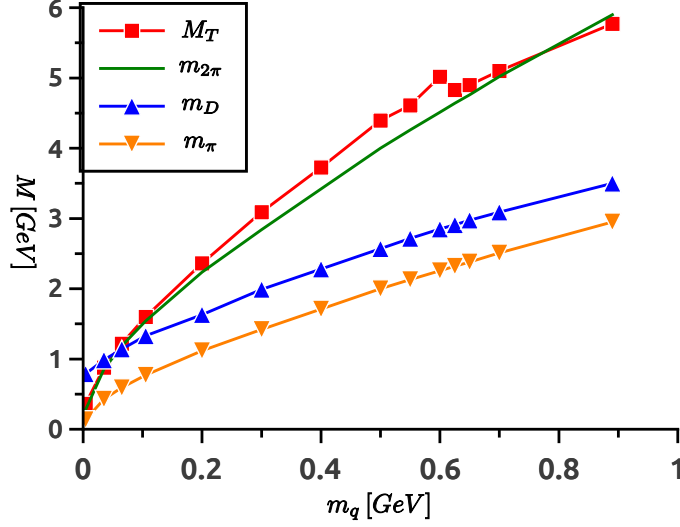


**Figure 5.3.:** Mass curves of the pion ( $m_\pi$ ), diquark ( $m_D$ ) and  $\sigma$ -like tetraquark ( $M_T$ ) in dependence of the quark mass. The green line denoted by  $m_{2\pi}$  represents the  $2m_\pi$  threshold.

for the zero crossing of the extrapolant. Finally, the mass corresponding to the zero crossing is identified with the bound state mass.

For mesons, the quantity in eq. (5.2.1) is approximately linear [76], so that a linear extrapolation is a valid choice. But in the case of tetraquarks, the curves show some small curvature, see appendix A.1. Therefore, in order to extract a mass from the eigenvalue curves, we used a linear *and* a quadratic extrapolation and compared both. The difference of the two extrapolation prescriptions is noted in table 5.1 and the curves and their extrapolants are given explicitly in the appendix A.1. Except for quark masses around  $0.6 GeV$ , both extrapolation prescriptions agree roughly on the five-percent level. However, around the a quark mass of  $0.6 GeV$  the curves are clearly non linear and also the quadratic extrapolation prescription breaks down because the curves bend *upwards* and do not cross the zero. We still extracted a mass by taking the peak of the quadratic extrapolant as mass. Therefore, the tetraquark masses in that quark mass range should be taken with a grain of salt. To conclude this technical remarks, we mention that figure 5.3 depicts the tetraquark masses obtained from a quadratic extrapolation.

We come now to the discussion of figure 5.3 make the following observation:

The pion curve (yellow triangles) follows the Gell-Mann-Oakes-Renner relation [121]

$$m_\pi^2 \propto m_q, \quad (5.2.2)$$

because it is the Goldstone boson, associated with the spontaneous break-down of the chiral symmetry. This is a well understood result and is closely connected to the ax-

ial Ward-Takahashi identity which is preserved by the Maris-Tandy interaction and the corresponding Bethe-Salpeter kernel.

The diquark (blue triangles), which is not a Goldstone boson, does not show such a behavior, but develops a finite part for vanishing quark masses. Interestingly, the pion and the diquark curve have the same shape, seemingly shifted by a constant. This is understandable from the fact that for the Maris-Tandy interaction, the scalar diquark BSE and the pion BSE differ by a colour factor  $\frac{1}{2}$  only.

The tetraquark (red squares) shows a completely different behavior. For quark masses around the physical mass, the tetraquark is lighter than the diquark but above the two pion threshold (green line). With increasing quark mass the tetraquark stays above this threshold with a slope that is steeper than the curves of the diquark and the pion. For a quark mass  $m_q$  of about  $0.625 GeV$  the mass curve develops a cusp. Behind the cusp the slope is reduced and for a quark mass of about  $0.7 GeV$  the tetraquark mass ultimately drops below the two pion threshold. Around the cusp, the quadratic extrapolation prescription, which was used to extract the tetraquark mass, becomes ambiguous and the extracted masses around the cusp should be seen as ‘guide for the eye’. Nonetheless, we conclude that the mass curve of the  $\sigma$  changes fundamentally for quark masses of about  $0.625 GeV$ .

It is worthwhile to note that the authors of ref. [122] also find a mass curve for the  $\sigma$  that features a cusp, albeit located at a lower quark mass. In this reference, the cusp originates in the T-matrix pole of the  $\sigma$  which for small quark masses comes as complex conjugated pair in the second Riemann sheet (resonance). With increasing quark mass the poles move closer together and one of the poles appears in the first sheet on the real axis (bound state) whereas the other one moves to the real axis of the second sheet (virtual particle). In a future work, it would be interesting to investigate this cusp more thoroughly by taking the threshold caused by the pion poles explicitly into account.

Besides the general form of the mass curve, we can extract two states that correspond to an all charm and all strange state respectively:

$$m_{\bar{s}\bar{s}s s} = 1.6 GeV \tag{5.2.3}$$

$$m_{\bar{c}\bar{c}c c} = 5.7 GeV. \tag{5.2.4}$$

They are close to the values  $m_{\bar{s}\bar{s}s s} = 1.3 GeV$  and  $m_{\bar{c}\bar{c}c c} = 5.3 GeV$  found in a previous work [99] employing a two-body approach, but a recent lattice study [123] that looked for the all charm state could not verify a tetraquark of that mass. However, the all charm tetraquarks were investigated by the authors in refs. [124, 125] which used a parametrized hamiltonian approach and a hadron string model to calculate the tetraquark. Both authors found the the all charm tetraquark to be around  $6 GeV$ , much closer to the  $2\eta_c$  threshold.

Furthermore, we can speculate that our all strange state is in the right mass region to be

be related to the  $f_0(1500)$  and/or  $f_0(1710)$  which are candidates for states with a sizable tetraquark component [126].

To improve the calculations of tetraquarks in the DSE/BSE framework, further investigations could follow two directions: First, improving the truncation and the model to probe the effect of those improvements on the tetraquark spectrum and secondly, developing and implementing a method in the BSE approach that can deal with poles and thus could be used to calculate tetraquarks beyond the  $2m_\pi$  threshold. Especially the deduction of a width, related to decays into mesons, would be one of the first things one could learn by going beyond the  $2m_\pi$  threshold.

Because the analytical structures in form of two-body poles in the phase space is a feature of the tetraquark and thus will prevail in all truncations, a proper treatment of these poles should be investigated before improving the truncation and even before including all tensor structures and all Lorentz invariants.

We point out that a lot of the numerical problems in the beginning of this thesis, even for tetraquark masses below the  $2m_\pi$  threshold, originated in the improper treatment of the pion poles in the phase space and were only solved by the pole ansatz introduced in chapter 4.4. One can therefore hope that by dealing with the poles above threshold, not only interesting quantities such as the width become calculable, but also the overall numerical stability will improve.

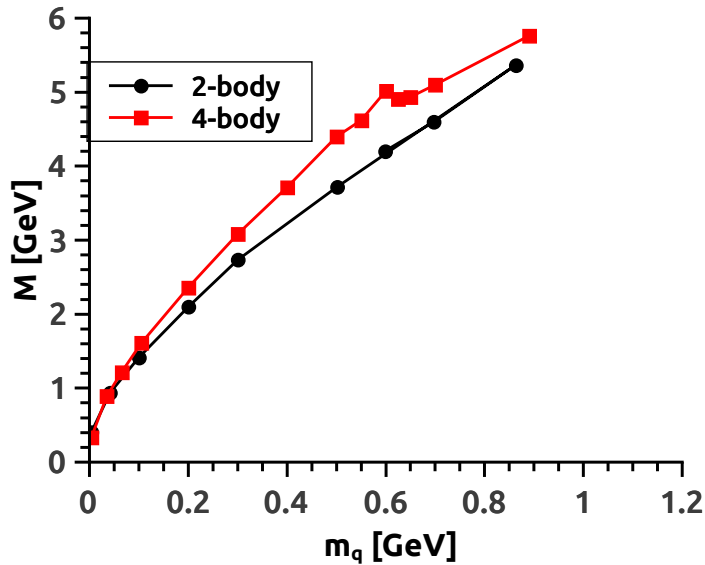


**Figure 5.4.:** Mass curves of the  $\sigma$  in the two-body approach [99] and in the four-body approach.

**Comparison to previous works** In our previous work, published in ref. [99], we approximated the four body equation with an effective two-body equation by employing pions and diquarks as constituents which interacted via a quark exchange. Within the two-body approach we calculated a mass curve for the equal mass  $0^+$  tetraquarks that looks qual-

itatively similar to the curve obtained in the four-body approach. A comparison of the four-body and two-body calculations is shown in figure 5.4. The curves agree for low quark mass but show some deviations for higher quark masses. It is interesting that we did not find a cusp like structure in the case of the two-body approach. Ignoring the deviations in the mid-mass range, it is striking that the two-body calculation that features different constituents and a different interaction agrees so well with the four-body calculation. We attribute this agreement to the fact that both approaches contain the pion which we found to dominate the  $\sigma$ . In the two-body approach they are included explicitly as (off-shell) particles whereas in the four-body equation they appear as poles in the phase space. In this sense, the more fundamental and consistent four-body calculation gives validity to the approximations employed in the two-body framework. It is also interesting to note that the main unresolved problem in the two-body approach is the same two-pion threshold that plagues the four-body calculation. Therefore, it would be advantageous to first solve the threshold problem in the numerical easier two-body framework and apply the methods to the numerical more involved four-body equation.

### 5.3. Masses of the scalar nonet

State	$m_T [GeV]$	PDG[14] [GeV]
$\sigma$	0.35	0.4 – 0.55
$\kappa$	0.64	$0.682 \pm 0.029$
$a_0/f_0$	0.89	$f_0 : 0.990 \pm 0.02$ $a_0 : 0.98 \pm 0.02$

**Table 5.2.:** Masses of the scalar tetraquark nonet. Calculated values are shown in the second column and values taken from the PDG are shown in the third column.

Besides the mass curve for tetraquarks with quarks with the same mass, we solved the BSE for the  $\kappa$  and  $a_0/f_0$  respectively. Right now, we do not include the full flavour amplitude as shown in chapter 3.3, but treat the  $\kappa$  as a  $\sigma$  with one quark replaced by an  $s$ -quark and the  $a_0$  and  $f_0$  as a  $\sigma$  with two quarks replaced by an  $s$ -quark. Because of the inclusion of quarks with a higher mass and the appearance of pion poles in the phase-space at the same time, the accessible tetraquark mass is much further away from the mass shell than in the case of the  $\sigma$ , see appendix A.1. This amounts to an extrapolation that is much further away from the calculated values, rendering the deduced values to be taken with some grain of salt.

The result is shown in table 5.2. Comparing these values with the candidates in the PDG [14], the masses in the Maris-Tandy model are generically too low. In the case of the  $\kappa$  and  $a_0/f_0$  this could be partially related to larger extrapolation errors but from our experience in the two-body approach [99], which also yielded a mass for the  $\sigma$  in the range of  $0.35 - 0.4 GeV$ , we suspect the low mass of the tetraquarks to be a feature of the Maris-Tandy model.

## 6. Conclusion and outlook

Bound states and their properties are an inherent non-perturbative feature of QCD. Moreover, QCD is a confining theory so that instead of the elementary quarks and gluons themselves, only colourless bound states formed of these elementary particles are directly measurable. One non-perturbative framework to describe QCD are the Dyson-Schwinger equations, which interrelate all Green functions of the theory by an infinite tower of integral equations, and the corresponding Bethe-Salpeter equations that define the bound states of the theory. To reduce the infinite tower to a tractable form, the equations have to be truncated. In this thesis, see chapter 2.9, we used a so-called ‘rainbow ladder’ truncation that reduces the quark-gluon vertex to the bare vertex and replaces the gluon by an effective modeled one so that the only Green function that has to be solved, is the quark propagator. This truncation preserves the important axial Ward-Takahashi-identity and the Gell-Mann–Oakes–Renner relation. For the effective gluon we used the Maris-Tandy gluon/interaction that is modeled to reproduce the pion mass and decay constant. Together, the truncation and the interaction model are well investigated in the meson and baryon sector and are known to yield a good description of various meson and baryon ground state properties.

Starting from this well-established truncation, the four-body tetraquark Bethe-Salpeter equation was constructed in chapter 2.5. Within this truncation, there are no irreducible three- or four-body interactions but only two-body ones, appearing in the form of one-gluon exchange diagrams. As elaborated in chapter 2.5.1, it turned out that for the tetraquark bound state equation, the one-gluon exchange diagrams have to be supplemented by two-gluon exchange diagrams to remove double counting which is absent in three-body and two-body Bethe-Salpeter equations.

To solve the tetraquark Bethe-Salpeter equation, a fully covariant basis for the tetraquark amplitude is necessary. Additionally, the basis has to reflect the quantum numbers of the tetraquark and has to fulfill the Pauli principle. The construction of such a basis was performed in chapter 3 for all parts of the amplitude: The Dirac-tensor structure, the phase space, the colour and the flavour tensor structure.

Upon solving the tetraquark bound state equation, dynamical poles in the tetraquark amplitude phase space appeared which are discussed in chapter 4. On one hand these poles caused major problems in solving the Bethe-Salpeter equation but on the other hand these poles reflect the actual physics that determines the tetraquark:

The tetraquark is dominated by two-body correlations which manifest themselves as poles in the phase space. It is especially noteworthy that these two-body correlations in form of poles are of a dynamical nature and are not put in by hand. Additionally, these two-body

poles in the four-body equation can be interpreted as connection between the more fundamental four-body picture, where four quarks bind together, and the two-body picture, where the tetraquark is pictured as a bound state of two mesons and/or diquarks. In accordance with previous studies in a two-body framework, the pion-pion correlations are found to be much more dominant than the diquark-diquark correlations.

Guided by the result that the tetraquark is dominated by poles in the phase space, an explicit pole ansatz for the amplitude was constructed in chapter 4.4. This procedure improved the numerical stability considerably.

Subsequently, in chapter 5 the Bethe-Salpeter equation was solved for tetraquarks with the quantum numbers  $0^{++}$ . For physical  $u/d$ -quark masses, we calculated the masses of the  $\sigma$  ( $m_\sigma = 0.35\text{GeV}$ ), the  $\kappa$  ( $m_\kappa = 0.64\text{GeV}$ ) and the  $f_0/a_0$  ( $m_\sigma = 0.89\text{GeV}$ ), with the corresponding masses given in brackets. Compared with the values of the experimental candidates, the masses are generically too low, probably caused by truncation artifacts.

According to the success of the Maris-Tandy model to describe ground state properties of mesons and baryons, our result is a strong indication that the lowest scalar nonet has indeed a considerable tetraquarks component.

We also investigated the quark mass dependence of the  $\sigma$  and found candidates for an all strange tetraquark around  $1.6\text{GeV}$  and an all charm tetraquark around  $5.7\text{GeV}$ . These findings agree qualitatively with our former results from a two-body approach. We also found that the mass curve features an interesting cusp at a quark mass of about  $0.65\text{GeV}$ . Such cusps are known in the literature to be related to whether the T-matrix pole corresponds to a bound-state, a resonance or a virtual state.

In this work a four-body tetraquark equation in the DSE/BSE framework was solved for the first time. Therefore, there are a some unresolved issues but also great opportunities to gain more insight into the nature of tetraquarks that make it worthwhile to further develop our approach.

Besides the incorporation of all tensor structures and Lorentz invariants to reduce the systematic numerical uncertainty, there are other interesting properties that could be investigated in future investigations. We will provide a small list and sketch how our framework could be used to achieve these goals. Moreover, we will outline the major problems and limitations one has to overcome.

**Other quantum numbers** The application of our framework to other quantum numbers is possible, as the construction principle for the tetraquark amplitude was laid down in chapter 3 for angular momentum  $J = 1$  and parity  $P = \pm$  states. A future investigation of these quantum numbers would be of high interest because some of the recently discovered charged charmonia states, which are most likely tetraquarks, have  $J > 0$  quantum numbers. From experience in the meson and baryon sector, the weak dependence of the tetraquark (mass) on some of the Lorentz invariants, see chapter 5.1, is expected to become stronger for  $J \neq 0$  states and the reduction of the nine dimensional phase space to a four dimensional one, see also chapter 5.1, would be no longer possible. Additionally,

the number of tensor structures will increase by a factor of three. Besides this increase in numerical complexity, the mass of these tetraquarks will be higher than the mass of the already calculated  $0^{++}$  states. To obtain a mass, the eigenvalue curve has to be extrapolated even further, increasing the systematic uncertainty of the extrapolation prescription. To avoid such an extrapolation, a proper incorporation of the two-meson poles that we found in the tetraquark amplitude is of high importance.

**Width, decays and beyond** Besides the mass of the tetraquark, the width, decays and various form-factors would provide valuable insight into the physics of tetraquarks. In order to calculate these properties, the amplitude has to be known on the mass-shell, which excludes the extrapolation prescription that was employed to deduce the mass in this thesis. The main reason that forced us to use an extrapolation prescription, was the appearance of two-meson poles in the phase space. The limitations caused by these poles are especially severe for tetraquarks that contain light quarks because the pion is so light. A proper treatment of the poles would render the extrapolation obsolete and would make it possible to search directly for poles in the complex plain of  $P^2$ , automatically yielding a width and providing the bound-state (or resonance) amplitude for further calculations, such as form factor calculations.

The pole expansion that was used for some of the Lorentz invariants, see chapter 4.4, points into one direction how to include threshold effects caused by poles in the phase space. Instead of using a pole ansatz for some of the variables, the whole scalar dressing function could be expanded in terms of meson poles. Besides an unambiguous complex continuation of the tetraquark amplitude, this expansion would make it possible to use contour deformation techniques to calculate the integrals of the BSE beyond the limitations posed by the various two-meson/diquark thresholds.

**Mixing** Although there exist various investigations of (scalar) mesons [80, 127, 128] and glueballs [65, 129] within the DSE/BSE approach, the mixing of these states is not investigated yet. Especially in the scalar  $0^{++}$  channel, the mixing of  $\bar{q}q$  mesons, glueballs and tetraquarks is still an open issue, experimentally and theoretically. Therefore, it would be of high interest to solve a system of DSEs and BSEs that takes into account  $\bar{q}q$  mesons, glueballs and tetraquarks at the same time, providing a consistent description of the mixing of these states. To achieve this goal within the DSE/BSE framework, one would certainly have to go beyond the rainbow ladder truncation employed in this work and the truncations used in the above mentioned references.

**Part B.**

**Beyond Rainbow ladder**

## 7. Introduction

Understanding the spectrum of light and heavy hadrons is an important task on our way towards a full understanding of QCD. In order to identify states that can be accounted for as quark-antiquark bound systems and separate them from more complex ones such as tetraquarks, meson molecules or glueballs one needs to develop a framework that makes contact to the details of the underlying quark-gluon interaction. Lattice QCD is one such approach, the functional method using Dyson-Schwinger equations (DSEs) and Bethe-Salpeter equations (BSEs) is another.

In the latter approach, the construction of an approximation scheme that yields an interaction consistent with chiral symmetry and its breaking patterns is a necessary requirement for the description of light mesons. Only then, the Goldstone boson nature of the pseudo-scalar bound-states are preserved resulting in a massless pion in the chiral limit [130, 59, 131]. This requirement can most easily be met with the rainbow-ladder truncation which has been widely applied for QCD phenomenology [132, 133, 134, 92]. This truncation has, however, limitations. These become visible for excited states [135, 136], states with finite width, or mesons with axial-vector or scalar quantum numbers, where the rainbow-ladder approach does not provide results in agreement with experiment. On a fundamental level, going beyond simple models for the quark-gluon interaction requires a dynamical treatment of the Yang-Mills sector of QCD as well as a treatment of the quark-gluon vertex that includes beyond rainbow-ladder structures [137].

There have been many efforts to go beyond rainbow-ladder. One promising route is to use explicit diagrammatic approximations to the DSE of the quark-gluon vertex [98, 138, 139, 140, 141, 142, 143, 102]. This allowed to explicitly study the effects of the gluon self-interaction [143] as well as pion cloud effects [102] on the spectrum of light mesons. Another promising approach uses explicit representations of selected tensor structures of the quark-gluon vertex [144, 100, 145, 127]. Most of these approaches have in common that they rely on techniques based on the two-particle-irreducible (2PI) representation of the effective action. In this language the interaction kernel is given as the functional derivative of the quark self-energy with respect to the quark propagator as is detailed in Refs. [130, 59].

In this work we use a similar idea. The difference is, though, that instead of employing a diagrammatic representation of the quark-gluon vertex, we use representations of the vertex that depend on the quark propagator explicitly and perform a systematic derivation of the corresponding Bethe-Salpeter kernel. Our approach is similar in spirit but technically different from the one outlined in [100, 145, 127] and therefore serves as a complementary tool. In particular it has the advantage, that not only the mesons' masses but also their

Bethe-Salpeter wave functions can be obtained. This opens up the possibility for future studies of structural information such as form factors and distribution amplitudes beyond the mere calculation of meson spectra. In this respect, our approach improves upon the previous ones.

## 8. Theoretical foundation

In this section we discuss the general principles that are at the heart of the techniques used in this work. This will also serve to make some basic definitions and to introduce our notation.

Our starting point is the definition of the quark anti-quark interaction Kernel  $K$  as the functional derivative of the quark self-energy  $\Sigma$  with respect to the dressed quark propagator  $S$

$$K_{ab}^{cd}(x, y, z, z') = \frac{\delta \Sigma^{cd}(x, y)}{\delta S^{ab}(z, z')}, \quad (8.0.1)$$

where  $a, b, c$  and  $d$  are Dirac indices and we work in coordinate space. In a similar fashion, the quark self-energy is obtained from the 2PI effective action. The technique given by Eq. (8.0.1) is often called 'cutting' since in a graphical language it corresponds to the cutting of a quark line. A good reason to use this technique is that it guarantees symmetries. The 2PI formalism allows for a closed representation of a truncated effective action in terms of a loop expansion [83, 146]. This has the advantage that the validity of symmetries, such as chiral symmetries, can be checked on the level of the effective action, i.e. the symmetries are manifest. The cutting procedure then generates equations that respect the consequences of the given symmetry. It has to be emphasized, however, that cutting alone is not sufficient. The quark gluon vertex also needs to behave correctly under chiral transformations [59]. An appropriate tool to investigate the transformation properties of the vertex in the momentum space representation is the axial-vector Ward Takahashi identity (AXWTI) which, if fulfilled, guaranties a massless pion in the chiral limit [131]. In the chiral limit this identity reads

$$iP_\mu \Gamma_{5\mu}(P, k) = S^{-1}(k_+) \gamma_5 + \gamma_5 S^{-1}(k_-), \quad (8.0.2)$$

where  $\Gamma_{5\mu}(P, k)$  is the axial-vector vertex, depending on the total and relative quark momenta  $P$  and  $k$ , and  $S^{-1}(k_\pm)$  the inverse quark propagator with  $k_\pm = k \pm P$ . The axial-vector vertex has an exact representation via a Bethe-Salpeter equation (BSE)

$$\Gamma_{5\mu}^{ab}(P, k) = - \int_q [S(q_+) \Gamma_{5\mu}(P, q) S(q_-)]^{cd} K_{cd}^{ab}(P, q, k), \quad (8.0.3)$$

where  $K$  is the Fourier transform of the exact kernel defined through Eq. (8.0.1) and  $\int_q = \int d^4q / (2\pi)^4$ . To proceed we have to define the quark self-energy in the exact form

$$\Sigma(k) = g^2 Z_{1F} C_F \int_q \gamma_\mu S(q) \Gamma_\nu(q, k) D_{\mu\nu}(q - k), \quad (8.0.4)$$

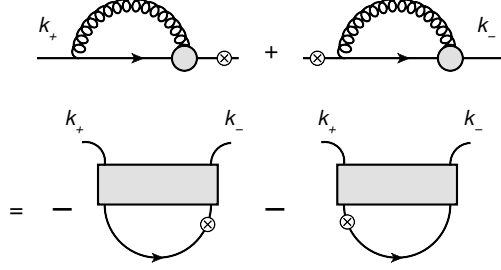


**Figure 8.1.:** A graphical representation of the AXWTI shown in Eq. (8.0.6). The Grey dots are the dressed quark-gluon vertices, Grey boxes denote the kernels and the crossed dots represent  $\gamma_5$ 's.

with the Casimir  $C_F = (N_c^2 - 1)/(2N_c)$ , the vertex renormalization factor  $Z_{1F}$ , the gluon propagator  $D_{\mu\nu}$  and the dressed quark-gluon vertex  $\Gamma_\nu$  depending on the incoming and outgoing quark momenta. The self-energy appears in the quark DSE

$$S^{-1}(k) = [S^0(k)]^{-1} + \Sigma(k). \quad (8.0.5)$$

with inverse bare propagator  $[S^0(k)]^{-1} = Z_2(-i\not{k} + m)$  including the quark wave function renormalization factor  $Z_2$ . The AXWTI from Eq. (8.0.2) can be rewritten in the form

$$\begin{aligned} & [\Sigma(k_+)\gamma_5 + \gamma_5\Sigma(k_-)]^{ab} = \\ & - \int_q [S(q_+)\gamma_5 + \gamma_5S(q_-)]^{cd} K_{cd}^{ab}(P, q, k), \end{aligned} \quad (8.0.6)$$

This representation is obtained upon inserting the BSE Eq. (8.0.3) in the AXWTI Eq. (8.0.2) and using the Dyson-Schwinger equation of the quark Eq. (8.0.5). A graphical representation of the resulting expression can be found in Fig. 8.1.

Before we apply the derivative of Eq. (8.0.1) to a given vertex representation we make a short mathematical detour. The space of Euclidean Dirac-matrices<sup>1</sup> is spanned by the 16 dimensional basis  $T_i = \{\gamma_\mu, \mathbb{1}, \gamma_5, \gamma_5\gamma_\mu, \sigma_{\mu\nu}\}$ , with  $\sigma_{\mu\nu} = i/2[\gamma_\mu, \gamma_\nu]$ . The elements obey <sup>2</sup> $T_i T_i = \mathbb{1}$  and  $1/4 \text{tr}[T_i T_j] = \delta_{ij}$ . Thus in general, the fully dressed quark propagator and inverse propagator can be represented by

$$S(p) = \sum_{i=1}^{16} T_i \tau_i(p^2), \quad S^{-1}(p) = \sum_{i=1}^{16} T_i \mathcal{A}_i(p^2), \quad (8.0.7)$$

where the quark dressings  $\tau$  and  $\mathcal{A}$  depend on the quadratic momentum only. The physical quark propagator has the structure  $S(p) = i\not{p}\sigma_V(p^2) + \sigma_S(p^2)$  but in the process of taking the derivative the representation of Eq. (8.0.7) is necessary for reasons of completeness.

<sup>1</sup>We use  $\{\gamma_\mu, \gamma_\mu\} = 2\delta_{\mu\nu}$ .

<sup>2</sup>No summation of indices here.

In particular we wish to maintain

$$\begin{aligned}
\delta_{ac} \delta_{bd} \delta^{(4)}(p-q) &\stackrel{!}{=} \frac{\delta S^{ab}(p)}{\delta S^{cd}(q)} \\
&= \sum_{i=1}^{16} \frac{\delta \tau_i(q)}{\delta S^{cd}(q)} \frac{\delta}{\delta \tau_i(q)} \sum_{j=1}^{16} T_j^{ab} \tau_j(p) \\
&= \sum_{i=1}^{16} \frac{1}{4} T_i^{dc} T_i^{ab} \delta^{(4)}(p-q), \tag{8.0.8}
\end{aligned}$$

which, as a completeness relation, can only be valid with the full basis. We used  $\delta \tau_i / \delta S^{cd} = 1/4 [T_i^{dc}]^{-1} = 1/4 T_i^{dc}$  and  $\delta \tau_j(p) / \delta \tau_i(q) = \delta_{ij} \delta^{(4)}(p-q)$ .

The functional derivative onto the quark self-energy (8.0.4) acts on the quark itself, the vertex and the gluon. For simplicity, in the following we disregard derivatives of the gluon propagator. Since the gluon depends on the quark only implicitly via closed loops, contributions from derivatives wrt. the quark only show up in kernels of flavour-singlet mesons. The following discussion is therefore directly applicable only in non-flavour-singlet channels but can be easily generalized to include also the flavour-singlet case.

Although the cutting rule is probably best defined in coordinate space, let us first work in momentum space. On the one hand, this serves illustrational purposes, on the other hand this is necessary for vertex models such as the Ball-Chiu construction [147], which are derived in momentum space. Later on we will demonstrate that the cutting procedure is much simpler in coordinate space and elaborate on a vertex construction (the Munczek vertex [59]) that has a corresponding representation. Cutting the quark propagator, we obtain the *modified* ladder-like contributions (called type *I* in the following)

$$\left. \frac{\delta \Sigma^{ab}}{\delta S^{cd}} \right|_I = \gamma_\mu^{ac} D_{\mu\nu} \Gamma_\mu^{db}. \tag{8.0.9}$$

This corresponds to a nonperturbative one-gluon exchange. However, in contrast to the usual ladder kernels one of the quark-gluon vertices is dressed.

For brevity, the kinematic dependences in Eq. (8.0.9) are suppressed. On a diagrammatic basis the correct kinematics are easily determined. Yet on a strict mathematical basis the quark is an arbitrary function in the 2PI formalism. Translational invariance cannot be assumed before relaxing the quark to the physical point. Thus in general one has to allow the quark and the self-energy to depend on different ingoing and outgoing momenta. It will be seen below in sections 9.1 and 9.2, that this introduces some complications in the kinematic dependencies of our kernels. These problems are easily overcome when working in coordinate space as will be shown in section 9.3.

Note that with a pure kernel of type *I* the AXWTI from Eq. (8.0.6) is fulfilled in the limit  $P \rightarrow 0$  only if  $\{\Gamma_\mu, \gamma_5\} = 0$ . This is because the terms on the right side of the AXWTI assume the form of self-energies for type *I* kernels. The  $\gamma_5$  has to be moved past the vertices, however. This is trivial for the bare vertex, but non-trivial for more elaborate vertex constructions, pointing towards the necessary appearance of a further type of contributions.

Indeed, a second type of contributions to the interaction kernel contain the variation of the quark-gluon vertex

$$\left. \frac{\delta \Sigma^{ab}}{\delta S^{cd}} \right|_{II} = \int_q [\gamma_\mu S(q)]^{aa'} \frac{\delta \Gamma_\mu^{a'b}(q, p)}{\delta S^{cd}(s)} D_{\mu\nu}(p - q), \quad (8.0.10)$$

which is referred to as type *II* contribution. In our notation the variation of the vertex can be decomposed as

$$\frac{\delta \Gamma_\mu^{ab}}{\delta S^{cd}} = \sum_i \frac{1}{4} T_i^{dc} \frac{\delta \Gamma_\mu^{ab}}{\delta \tau_i} \quad (8.0.11)$$

where the Dirac indices  $\{c, d\}$  are the ones connecting to the incoming quarks. Thus the appearance of certain Dirac structures in the interaction kernel is dictated by whether a corresponding functional variation of the vertex evaluates to zero or not. We will come back to this in the following sections where different vertex representations are considered. The main observables that we will study to underline our theoretical considerations and test the approach are masses of light mesons in the (pseudo-)scalar and (axial-) vector channels. Their generic Bethe-Salpeter equation for the meson amplitude  $\Gamma_M^{(\nu)}$  is given by

$$\begin{aligned} \left[ \Gamma_M^{(\nu)} \right]^{ab}(P, k) = \\ - \int_q [S(q_+) \Gamma_M^{(\nu)}(P, q) S(q_-)]^{cd} K_{cd}^{ab}(P, q, k), \end{aligned} \quad (8.0.12)$$

with kernel  $K$  and the total momentum satisfies  $P^2 = -m_M^2$  with  $m_M$  the mass of the meson in question. For pseudo-scalar mesons, like the pion, the amplitude has the decomposition

$$\begin{aligned} \Gamma_\pi(P, k) = \\ \gamma_5 [E(P, k) + i \not{P} F(P, k) + i \not{k} G(P, k) - [\not{P}, \not{k}] H(P, k)]. \end{aligned} \quad (8.0.13)$$

Similar decompositions for the other mesons are given e.g. in ref. [148]. Furthermore we quote here the Gell-Mann–Oakes–Renner relation (GMOR) [121]

$$f_\pi^2 m_\pi^2 = \langle \bar{\psi} \psi \rangle_\mu m(\mu), \quad (8.0.14)$$

which will be a tool to test the chiral properties in our numerical treatment in section 10. Here  $f_\pi$  is the pion decay constant,  $\langle \bar{\psi} \psi \rangle_\mu$  the chiral condensate and  $m(\mu)$  the running quark mass at renormalization point  $\mu$ .

## 9. Constructing the kernel

In the following we show explicitly, how our formalism serves to construct the kernel, once a representation of the quark-gluon vertex in terms of the quark dressing functions is known. For the longitudinal part of the vertex such a representation can be derived (approximately) from its Slavnov-Taylor identity [149]. It reads

$$p_3^\mu \Gamma(p_1, p_2) = G(p_3^2) \times \left[ H(p_1, p_2) S^{-1}(p_2) - S^{-1}(p_1) H(p_1, p_2) \right] \quad (9.0.1)$$

in terms of the inverse quark propagator  $S^{-1}$ , the ghost dressing function  $G$  and a ghost-quark scattering kernel  $H$ . The momenta  $p_1, p_2$  correspond to the quark legs of the vertex, whereas  $p_3 = p_2 - p_1$  denotes the momentum from the gluon leg. Assuming that  $H(p_1, p_2)$  can be approximated by a function  $\tilde{H}(p_3^2)$  depending on the gluon momentum only, the STI can be converted into a Ward-Takahashi identity with an extra factor  $G\tilde{H}$  on the right hand side. It is then solved by the Ball-Chiu construction [147] supplemented with the product  $G\tilde{H}$

$$\Gamma_\mu^{BC}(p_1, p_2) = G(p_3^2) \tilde{H}(p_3^2) \left[ \gamma_\mu \frac{A(p_1^2) + A(p_2^2)}{2} + 2\not{k} k_\mu \frac{A(p_1^2) - A(p_2^2)}{p_1^2 - p_2^2} - i2k_\mu \frac{B(p_1^2) - B(p_2^2)}{p_1^2 - p_2^2} \right], \quad (9.0.2)$$

where  $k = (p_1 + p_2)/2$  and vector dressing  $A$  and scalar dressing  $B$  of the inverse quark propagator

$$S^{-1}(p) = i\not{p} A(p^2) + \mathbb{1} B(p^2). \quad (9.0.3)$$

Within the quark-DSE the functions  $G(p_3^2)\tilde{H}(p_3^2)$  can then be combined with the gluon propagator into an effective gluon (cf. Appendix B.3) and the vertex has an Abelian structure. As a result one has a representation of the vertex in terms of the quark dressing functions. In general, this construction can be supplemented by transverse terms that are not restricted by the STI/WTI and can be either modeled or extracted from explicit solutions of (approximations of) the vertex-DSE. However, for the purpose of this work we restrict ourselves to the Ball-Chiu part of the vertex since it serves nicely to illustrate the merits of our formalism.

In the following we will first treat the first two terms of this vertex ('2BC vertex model'), then deal with the third term in addition ('Ball Chiu vertex model') and finally work with a different solution of the WTI (the 'Munczek vertex model') that is suited to explore the cutting procedure in coordinate space.

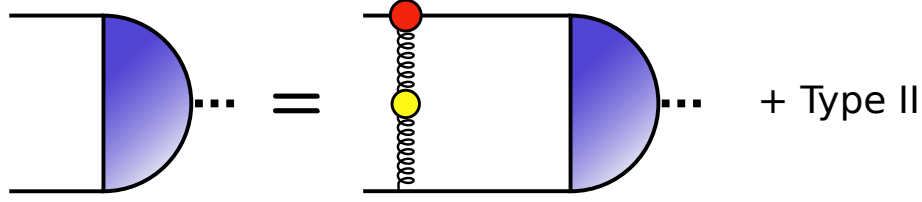


**Figure 9.1.:** Bethe-Salpeter equation for mesons including kernel contributions of type I (dressed one-gluon exchanged) and type II (see text).

## 9.1. The 2BC Vertex model

Here we consider the first two terms of the parts of the Ball-Chiu vertex Eq. (9.0.2) with tensor structures  $\gamma_\mu$  and  $\not{k}$ . Note that these structures correspond to four different structures in the notation of Eq. (8.0.7). In order to carry out the cutting for type *II* kernels along the lines of Eqs. (8.0.10) and (8.0.11) we therefore write

$$\gamma_\mu A \rightarrow \gamma_\mu A_\mu \quad \not{k} A \rightarrow \sum_\alpha k_\alpha \gamma_\alpha A_\alpha \quad \mu, \alpha \in \{1, 2, 3, 4\}, \quad (9.1.1)$$

where no summation over the index  $\mu$  is performed. The functions obey  $A_\mu = \mathcal{A}_\mu/(-ip_\mu)$ , i.e. they represent the subset of the  $\mathcal{A}$  functions, defined in section 8, that correspond to the  $\gamma_\mu$  structures of the Dirac algebra. Via Eq. (9.0.2) the  $A_\mu$  functions are explicitly given in terms of the  $\tau$ -dressings of the quark in the notation of Eq. (8.0.7).

The vertex model Eq. (9.0.2) is defined on the physical point of Dirac space and we call the four contributing basis structures  $\gamma_i$  the physical directions in Dirac-space. However, the actual cutting procedure Eq. (8.0.1) has to be performed in all directions of Dirac-space, i.e. also in the unphysical ones. In analogy to ordinary functions a functional that is zero at a given point may nevertheless have a non-vanishing functional derivative. Thus the cutting-procedure may very well pick up contributions from the unphysical directions. In order to completely specify a vertex model *and* the corresponding Bethe-Salpeter kernel it is therefore not sufficient to define the model on the physical point, but we need additional information on its behavior in the unphysical directions of Dirac-space.

This is irrelevant for the type I contribution of the kernel obtained from cutting the quark line in the quark-DSE. The resulting expression is afterwards set to the physical point and represents the modified dressed one-gluon exchange shown in Fig. 9.1. The situation is different, however, for the type II contributions involving the functional derivative of the vertex.

Let us assume for the moment that our 2BC vertex model away from the physical point still has the reduced functional dependence  $\Gamma_\mu^{2BC}[A_\mu[\tau_{1\dots 4}]]$  corresponding to  $T_{1\dots 4} = \gamma_{1\dots 4}$  and the unphysical directions in Dirac space are identical to zero. This then yields  $\delta\Gamma_\mu/\delta\tau_i = 0, \forall i > 4$  such that the external legs of the kernel that will connect to the internal quark lines in the Bethe-Salpeter equation have a restricted tensor structure. In this case, type II contributions to the kernel will appear, but due to their restricted tensor structure they contribute neither to the AXWTI nor to the Bethe-Salpeter equation for pseudo-scalar (and axial-vector) mesons. This is because of the  $\gamma_5$  contained on the right hand side of the

AXWTI Eq. (8.0.6) and in the meson amplitudes of the Bethe-Salpeter equation (8.0.12) which lead to zero traces. The explicit form of these type II contributions, relevant for scalar and vector mesons, is discussed in appendix B.1.

In the AXWTI we thus have to consider only the modified ladder type contributions. Both vertex structures in the first two terms of Eq. (9.0.2) anti-commute with  $\gamma_5$  so that for this particular vertex model the AXWTI Eq. (8.0.6) is fulfilled in the limit  $P \rightarrow 0$ . For the pseudo-scalar bound-states the modified ladder contributions are all that remains and lead to a massless pion in the chiral limit. This finding will be confirmed by our numerical results in section 10.

Note, however, that the AXWTI is only satisfied in the limit  $P \rightarrow 0$ . This is because the left and right side of the equation, although similar on the diagrammatic level, need a momentum shift to be absolutely identical. This momentum shift becomes impossible due to the momentum dependence of the first two terms in the vertex (9.0.2). In the limit  $P \rightarrow 0$ , however, the diagrams become equal. For physical pions, a simple vertex model such as the 2BC-vertex cannot be the full story and corrections from unphysical directions in Dirac space are necessary. In principle, the requirements of chiral symmetry via the AXWTI allow for a systematic procedure to construct such extensions thus completing a given vertex model. We will perform this exercise in the next section. Allowing the functions  $A_\mu$  to depend on  $\tau_{1\dots 16}$ , non-vanishing contributions of type *II* in the AXWTI and the pseudo-scalar BSEs are generated which can be used to restore the requirements of chiral symmetry also away from the chiral limit. This emphasizes again that a truncation is not uniquely fixed by the vertex model on the physical point.

## 9.2. The Ball-Chiu vertex model

In addition to the first two terms of the Ball-Chiu type vertex in Eq. (9.0.2) we will also consider the third term, which is proportional to the scalar basis element  $T_5 = \mathbb{1}$  in Dirac space. Since this term does not anti-commute with  $\gamma_5$  it cannot fulfill the AXWTI (8.0.6) on the level of a pure type *I* ladder kernel. This can, however, be cured by allowing for type *II* contributions to the kernel that couple to the pseudo scalar channel. In order to generate these in a systematic way, we allow the vertex to depend on unphysical components that will be set to zero in the end, but will contribute during the cutting procedure. Therefore, we write the quark generically as

$$\begin{aligned} S(p) &= \left( i \sum_{j=1}^4 \sigma_j p_j \gamma_j \right) + \sigma_S \mathbb{1} + \sigma_5 \gamma_5 \\ S^{-1}(p) &= \left( -i \sum_{j=1}^4 A_j p_j \gamma_j \right) + B \mathbb{1} + C \gamma_5, \end{aligned} \quad (9.2.1)$$

with  $\sigma_5 = 0$ ,  $C = 0$ ,  $\sigma_j = \sigma_V$  and  $A_i = A$  on the physical point. The functions obey  $\sigma_j = \tau_j / ip_j, \forall i \leq 4$ ,  $\sigma_S = \tau_5$  and  $\sigma_5 = \tau_6$ . The reason why we need only six instead of the full sixteen tensor structures in Dirac space is that we will assume a certain functional

dependence of the vertex on the quark dressings as in the preceding section. Our vertex, called *ABC-vertex* from now on, reads

$$\Gamma_\mu^{ABC} = \Gamma_\mu^{BC} + i2 \gamma_5 k_\mu \frac{C(k_+^2) - C(k_-^2)}{k_+^2 - k_-^2}. \quad (9.2.2)$$

This vertex corresponds to the Ball-Chiu construction for a quark with  $C \neq 0 \neq \sigma_5$  as given in Eq. (9.2.1). Thus we assume that the vertex does depend only on the quark dressings  $A$ ,  $B$  and  $C$ , limiting the possible structures in the type *II* part of the kernel. We furthermore generalize the  $A$  function as discussed in Eq. (9.1.1). This fully determines the Ball-Chiu type of vertex construction for a quark of the form shown in equation (9.2.1). Now we have laid the basis to explicitly derive the type *II* kernel for the vertex of Eq. (9.2.2). The complete set of these kernels is treated in appendix B.1. It turns out, however, that the application of Eq. (8.0.11) generates only one single type *II* kernel that contributes to the AXWTI and the pion BSE after relaxing all dressings to the physical case. Only the derivative with respect to  $\sigma_5$ , being accompanied by the  $\gamma_5^{dc}$  structure (see Eq. (8.0.11)), will give a non-zero contribution upon tracing with the additional  $\gamma_5$  as present in the AXWTI (8.0.6) and the pion BSA (8.0.13).

The relevant piece of Eq. (8.0.11) evaluates to

$$\frac{1}{4} \gamma_5^{dc} \frac{\delta \Gamma_\nu^{ab}(l, k)}{\delta \sigma_5(q)} = \frac{1}{4} \frac{i(l+k)_\nu}{l^2 - k^2} \left[ \frac{\delta C(l^2)}{\delta \sigma_5(q)} - \frac{\delta C(k^2)}{\delta \sigma_5(q)} \right] \gamma_5^{dc} \gamma_5^{ab}, \quad (9.2.3)$$

with

$$\left. \frac{\delta C(l^2)}{\delta \sigma_5(q)} \right|_{phys} = -\frac{1}{4} \frac{1}{\sigma_V^2(l)l^2 + \sigma_S^2(l)} \delta^{(4)}(l - q). \quad (9.2.4)$$

The corresponding kernel is then generated by insertion into Eq. (8.0.10). The resulting expression is provided in appendix B.2 where we also prove that the AXWTI is fulfilled in the limit of vanishing total momentum.

We would like to emphasize that we make a non-trivial observation here. We nicely see how type *I* and type *II* contributions cancel each other exactly in the AXWTI as is shown explicitly in appendix B.2. This gives deep insight into the way chiral symmetry is at work in beyond rainbow-ladder truncations in general. In fact it is no coincidence that the generalized Ball-Chiu vertex from equation (9.2.2) has the correct behavior. Following the arguments of ref. [59] a quark-gluon vertex model that transforms under local chiral transformations as an inverse quark should leave chiral symmetry intact in every possible relation derived from the 2PI effective action. A vertex that fulfills the vector WTI, as the BC vertex does, is thus at least a very good candidate for a vertex model. We show here, how these formal arguments are realized explicitly in a Bethe-Salpeter interaction kernel. There is, however, an additional subtle point here. The momentum space representation of Eq (8.0.1), if written as  $K = \delta\Sigma(p)/\delta S(l)$ , depends only on two momenta,  $p$  and  $l$ . As a four-point function  $K$  should depend on three independent momenta in general  $K(P, p, l)$  as is the case for the type *I* interaction  $K_I(P, p, l) = \gamma_\mu D_{\mu\nu}(p-l)\Gamma_\nu(l, p_+)$ . As

argued above, from our cutting procedure this is not plain obvious, instead we complete the kinematic dependence on the diagrammatic level. For the type *II* kernels this is, however, not so simple since these have no representation as Feynman-diagrams. We choose the kinematics such that the potential dangerous singular structure of Eq. (9.2.3) stays harmless. This is also detailed in appendix B.2.

### 9.3. The Munczek vertex model

Finally we treat a vertex model that has been formulated in coordinate space. We will see, that this choice leads to unique kinematics in the derived kernel and provides for a simple and elegant kernel. The vertex ansatz has been given by Munczek in ref.[59] and reads in coordinate space:

$$\Gamma_\mu(z; x, y) = iS^{-1}(x, y) \times \int \frac{d^4q}{(2\pi)^4} \left[ e^{iq \cdot (z-y)} - e^{iq \cdot (z-x)} \right] \frac{x_\mu - y_\mu}{q \cdot (x - y)}. \quad (9.3.1)$$

Because of the unusual form of this vertex, we repeat a few arguments for this particular choice of vertex, given in [59]:

This vertex transforms under local chiral transformations in the following way:

$$\Gamma_\nu(z; x, y) \rightarrow e^{-i\gamma_5 \tau^l \theta_l(x)} \Gamma_\nu(z; x, y) e^{-i\gamma_5 \tau^l \theta_l(y)} \quad (9.3.2)$$

similar to the inverse quark

$$S^{-1}(x, y) \rightarrow e^{-i\gamma_5 \tau^l \theta_l(x)} S^{-1}(x, y) e^{-i\gamma_5 \tau^l \theta_l(y)}. \quad (9.3.3)$$

This ensures that the 2PI effective action is invariant under a local chiral transformation which is necessary for the pion to be a Goldstone boson. As in the Ball-Chiu case, this vertex ansatz is free of kinematic singularities and compatible with the vector Ward identity (WTI) in coordinate space:

$$\frac{\partial}{\partial z_\mu} \Gamma_\mu(z; x, y) = i [\delta(y - z) - \delta(x - z)] S^{-1}(x, y). \quad (9.3.4)$$

From a technical point of view, the biggest advantage of this vertex, in comparison to the Ball-Chiu one, is the fact, that a representation in coordinate space is available. All the problems of the ambiguous momentum routing, that plagued the cutting procedure for the Ball-Chiu vertex are resolved when applying the cutting procedure to the self-energy in coordinate space. After the cutting, a transformation back to momentum space is possible and yields a closed expression for the interaction kernel and the vertex. For more technical details we refer to appendix B.4, presenting here only the results.

With the definition

$$\left[ \hat{S}^{-1} \right]^\mu := \frac{\partial}{\partial k^\mu} S^{-1}(k) \Big|_{k=k_r + \alpha(k_l - k_r)} \quad (9.3.5)$$

the vertex reads

$$\Gamma^\mu(k_l, k_r) = i \int_0^1 \left[ \hat{S}^{-1} \right]^\mu d\alpha. \quad (9.3.6)$$

Here the momentum  $k_l$  specifies the incoming left momenta and  $k_r$  the outgoing right momenta. They are connected via  $k = k_l - k_r$  where  $k$  is the outgoing gluon momentum. For the kernel we introduce some shorthand notations:

$$\left[ \hat{\Gamma}_\pi \right]^\nu := \frac{\partial}{\partial p^\nu} \Gamma_\pi(p; P) \Big|_{p=\tilde{p}+\alpha(\tilde{p}-p)} \quad (9.3.7)$$

$$\tilde{\Gamma}_\pi := S(p_+) \Gamma_\pi(P, p) S(p_-), \quad (9.3.8)$$

with  $P$  the total and  $p$  the relative momenta of the two-body bound-state and  $p_\pm = p \pm P/2$ . The resulting kernel can be written down in a closed form as linear operator. Inserted into the right hand side of the Bethe-Salpeter equation we obtain

$$\begin{aligned} \int [K^{II} \tilde{\Gamma}_\pi]_{ab} = & \\ \frac{i}{2} \int_{\tilde{p}} d^4 \tilde{p} \int_0^1 d\alpha \left[ \hat{\Gamma}_\pi \right]_{b'b}^\nu & S_{a'b'}(\tilde{p}_-) \gamma_{aa'}^\mu D^{\mu\nu}(\tilde{p} - p) \\ & + \left[ \hat{\Gamma}_\pi \right]_{aa'}^\nu S_{a'b'}(\tilde{p}_+) \gamma_{b'b}^\mu D^{\mu\nu}(\tilde{p} - p). \end{aligned} \quad (9.3.9)$$

This expression is already symmetrized as explained in appendix B.4. The Latin indices represent the Dirac matrix indices. All other additional factors as colour etc. are suppressed. It is interesting to see that the self-energy of the quark, Eq. (8.0.4) with Eq. (9.3.6) as vertex, and the type II contribution to the BSE, Eq. (9.3.9), have the same structure. The only difference, modulo momentum dependence, is the replacement of  $\left[ \hat{S}^{-1} \right]^\mu$  with  $\left[ \hat{\Gamma}_\pi \right]^\mu$ . Upon inserting the kernel in Eq. (8.0.6) and working out the details it can be seen, that the AXWTI is fulfilled and that the structural similarity plays an important role in doing so.

These findings can be summarized in the following way:

- In order to meet the transformation property of Eq. (9.3.2) a vertex model is chosen that depends linearly on  $S^{-1}$  with the transformation properties of Eq. (9.3.3).
- The additional terms on the rhs of Eq. (8.0.6), stemming from the cutting procedure have the same structure as a quark self-energy **because** the vertex is linear dependent on  $S^{-1}$ .
- This additional terms that look like quark self-energies cancel other terms on the rhs of Eq. (8.0.6). This happens in a similar fashion as for the ABC vertex, cf. appendix B.2.

As shown in ref. [59] this comes with no surprise: If the vertex transforms in the proper way, the determination of the kernel via cutting of the quark self-energy yields a interaction

that preserves the AXWTI. The linearity on  $S^{-1}$  is not necessary, but one has to work much harder to preserve the correct transformation behavior if the vertex is nonlinear in  $S^{-1}$ . In the result section we check the GMOR explicitly for this particular choice of vertex.

We make a last comment regarding the similarity between the Munczek vertex and the BC vertex. Despite the unusual form of the vertex in Eq. (9.3.9), this vertex has a striking resemblance with the Ball-Chiu vertex in momentum space. This can be seen by carrying out the derivative in Eq. (9.3.6) explicitly

$$\Gamma^\mu(p_l, p_r) = \int_0^1 d\alpha [2p^\mu A'(p^2) \not{p} + \gamma^\mu A(p^2) - i2p^\mu B'(p^2)]_{p=p_r+\alpha(p_l-p_r)}. \quad (9.3.10)$$

Where the BC vertex has terms that look like finite differences, the Munczek vertex has derivatives smeared by the  $\alpha$  integral.

## 10. Numerical results

For our numerical analysis the quark DSE Eq. (8.0.5) was solved for complex momenta following a contour method, described in ref. [67]. The BSE is solved as an eigenvalue problem with standard numerical methods.

We solved the BSE for the different Ball-Chiu vertex models described in the sections before. Our first main result is shown in Fig. 10.1. For the 1BC and 2BC vertices, the cutting of the vertex yields no additional contribution to the kernel of the pion, so that the kernel is purely of type  $I$ . As argued before, the 1BC and 2BC vertex models have only vector contributions that are proportional to  $\gamma^\mu$  and thus cause no problems in the AXWTI. As one can see in Fig. 10.1 the GMOR-relation (8.0.14) is satisfied: the squared pion mass scales linearly with the quark bare mass and goes through the origin.

The results for the full BC vertex are much more intricate. As described above, setting the BC vertex to its physical form before the cutting procedure yields no contribution of type  $II$  to the pion BSE. Since the scalar parts of the vertex proportional to  $\mathbb{1}$  spoil the AXWTI, the resulting equations are not in accord with the requirements of chiral symmetry. This directly translates to a severe violation of the GMOR with a heavy pion of 400 MeV in the chiral limit. Adding 'unphysical' directions to the vertex before cutting, however, solves the problem as elaborated in section 9.2. With the resulting ABC-vertex the GMOR-relation is satisfied, and the corresponding curve in Fig. 10.1 again describes a Goldstone boson.

Our results for the Munczek vertex model from section 9.3 are displayed in Fig. 10.2. Again we find that the pion becomes a Goldstone boson in the chiral limit. The main difference as compared to the Ball-Chiu vertex is that we did not have to add terms along unphysical directions. This nicely underlines the main message of ref. [59]: having the right chiral transformation property already on the level of the vertex representation ensures a massless pion in the chiral limit, provided the kernel is properly constructed. The Munczek vertex preserves all symmetries by design and produces the correct type  $II$  kernel contributions for the pion automatically.

It is also interesting to discuss the physical implications of such a type of vertex. The Munczek vertex possesses a structure that is proportional to  $\mathbb{1}$  and the derivative of the scalar quark dressing function. Such a structure is not present in the chirally symmetric theory and thus represents an important addition to the structure of the vertex that is mainly generated by the dynamical effects of chiral symmetry breaking. This structure is also not present in a usual ladder approximation with a vertex proportional to  $\gamma^\mu$ . In the Munczek vertex, this term plays a similar role than the corresponding scalar contribution to the Ball-Chiu vertex. In ref. [100] this term has been interpreted as being responsible

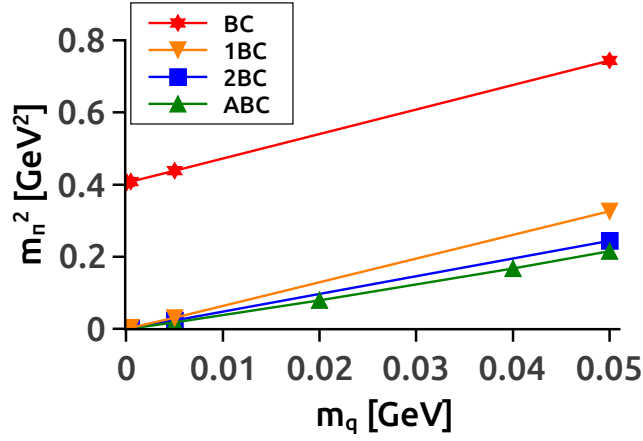


**Figure 10.1.:** This figure depicts the quark mass behavior of the pion mass in the BC-vertex models. Here '1BC' corresponds to a vertex, where only the first term of the Ball-Chiu vertex has been taken into account, '2BC' to the vertex treated in section 9.1, 'BC' is the physical Ball-Chiu vertex dealt with in section 9.2 and 'ABC' is its completion with unphysical directions before cutting, Eq. (9.2.2). The quark mass  $m_q$  is evaluated at a renormalization point of  $\mu = 19$  GeV.

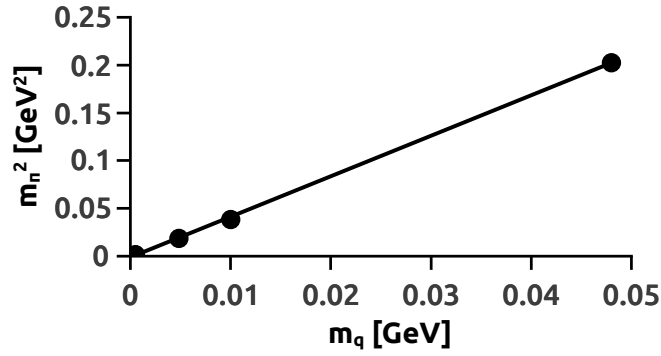


**Figure 10.2.:** This figure depicts the quark mass behavior of the pion mass in the Munczek-vertex model.

for a dramatic increase in the mass splitting between the scalar and the pseudo-scalar ground state and was interpreted as a repulsive spin-orbit force.

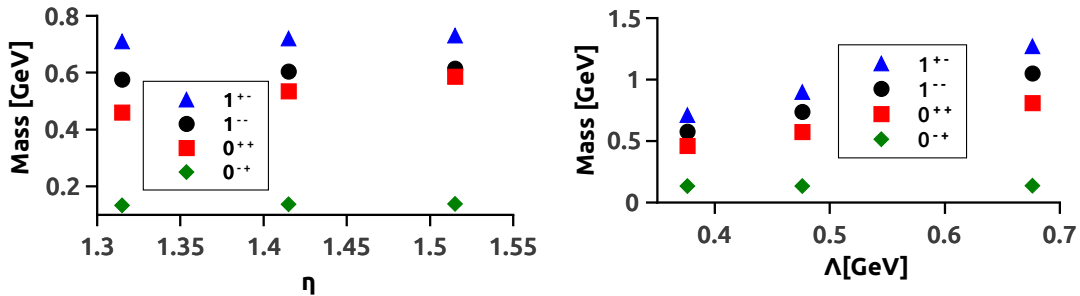


**Figure 10.3.:** Meson ground state masses in dependence of the details of the quark-gluon interaction with Munczek vertex. In the left panel  $\Lambda = 0.376$  is held fixed, in the right panel  $\eta = 1.315$ .

$\Lambda$	$\eta$	$f_\pi$ [GeV]		$\Lambda$	$\eta$	$f_\pi$ [GeV]
0.376	1.315	0.094		0.376	1.315	0.094
0.376	1.415	0.103		0.476	1.315	0.118
0.376	1.515	0.109		0.676	1.315	0.165

**Table 10.1.:** Pseudo-scalar decay constants in dependence of the details of the quark-gluon interaction with Munczek vertex.

We investigated the Munczek vertex for a similar behavior. In order to assess the model dependence of our results we varied the parameters  $\eta$  and  $\Lambda$  in the ansatz for the effective interaction, see Eq. (B.3.2). For each value of the parameters we adjusted the bare quark mass to obtain roughly the physical pion mass of  $m_\pi = 0.137$  GeV. We then calculated the pion decay constant on the pion mass shell, see [131] for numerical details, and the masses for the pion, the scalar, the vector and the axial-vector ground states. Our results are shown in Fig. 10.3 and in Tab. 10.1.

In general, the pion mass serves to fix the input quark mass, whereas the pion decay constant is sensitive to the scale of the interaction. In pure rainbow ladder calculations it has been observed that once the scale is fixed via  $\Lambda$ , there is a whole range of values for  $\eta$  which leave the pion decay constant untouched. It has also been established, that the masses of the scalar and vector meson bound-states are almost insensitive to these variations [128]. This is no longer true, when the vertex is non-trivial as can be seen from Fig. 10.3. Varying the parameters of the interaction one clearly finds a great impact onto the meson mass spectrum. This comes with an increase of the splitting between pseudo-scalar and scalar channels as well as vector and axial-vector channels. Thus in principle, by variation of the model parameters one could drive the masses of the scalar and axial-vector states in a region around and above 1 GeV, where they could be identified with physical states such as the  $f_0(1370)$  and the  $a_1(1260)$ .

	$\Lambda$	$\eta$	$f_\pi$	$m_\pi$	$m_\sigma$	$m_\rho$	$m_{a1}$
RL	1.797	0.094	0.093	0.137	0.65	0.73	0.83
MV	0.376	1.315	0.094	0.134	0.46	0.58	0.71

**Table 10.2.:** Meson masses and decay constants (in units of GeV) for Rainbow ladder (RL) compared with our results using the Munczek vertex (MV).

However, with the construction at hand this would be stretching the model much too far: as can be seen from Tab. 10.1 also the pion decay constant increases with increased spin-orbit splitting, clearly indicating that one is no longer working with acceptable model parameters. Indeed, when we compare the rainbow-ladder result (RL) with the improved approximation scheme using the Munczek vertex (MV) in Tab. 10.2 with model parameters adjusted such that the pion decay constant comes out right we even observe a decrease of the spin-orbit splitting. Similar results can be obtained with the improved Ball-Chiu vertex

(ABC) of section 9.2. We thus find, that a Ward-Identity improved vertex alone is not enough to reproduce the size of the spin-orbit splitting that is suggested from experiment. Note that we do not put much emphasis on the fact, that the mass of the quark-antiquark bound-state in the scalar channel using the MV-vertex is even in the right ballpark for the  $f_0(500)$ . As noted in ref. [127] there are indeed transverse parts of the vertex that do increase the spin-orbit splitting by a substantial amount thus making the identification with the  $f_0(1370)$  more likely. This also ties in with findings of Refs.[99].

# 11. Conclusions

Following the time-honored concept of taking functional derivatives to obtain an interaction kernel, we extended this technique to vertex models which explicitly depend on the quark propagator and its dressing functions. This enabled us to derive closed expressions for the interaction kernel beyond the rainbow-ladder approximation. Our technique is very general, and in principle applicable to any vertex that is given in terms of quark dressing functions. As an improvement over previous approaches [100, 145, 127] our technique allows to determine not only the masses of the bound-states but also their Bethe-Salpeter wave functions. Certainly, these are indispensable when it comes to the calculations of form factors, structure functions, or decay widths of the states in question.

As examples, we applied this technique to two type of vertices, the Ball-Chiu vertex and the Munczek vertex that both respect the constraints due to the vector Ward-Takahashi identity. For the Ball-Chiu vertex we find that we have to amend the vertex by additional parts along unphysical directions in Dirac space. These do not contribute to the Dyson-Schwinger equation for the quark propagator, but generate important additional terms into the interaction kernel of Bethe-Salpeter equations necessary to respect the axial Ward-Takahashi identity. The resulting pion is then a Goldstone boson in the chiral limit. For the Munczek vertex, such additional contributions are not necessary.

Using the Munczek vertex we performed a calculation of the masses of pseudo-scalar, scalar, vector and axial-vector mesons and confirm the findings of ref.[100]: the additional gauge related structure in the vertex is dominated by dynamical effects of chiral symmetry breaking and capable to generate substantial spin-orbit forces. However, these structures alone are not sufficient to generate a physical spectrum of light mesons while keeping the pion properties intact. Additional transverse pieces in the vertex are necessary to improve this situation.

**Connection to tetraquarks** The beyond-rainbow ladder study part of the thesis was finished before the tetraquark part. Therefore we will conclude this work by a few remarks regarding the scalar tetraquarks calculated in the first part of this thesis and the scalar  $\bar{q}q$  mesons calculated in the second part. Using the Munczek vertex, we obtained a scalar meson of the order of  $0.5 \text{ GeV}$ , whereas for the tetraquark we get a mass of around  $0.350 \text{ GeV}$ . Even taking into account that the tetraquark is calculated in the Maris-Tandy model so that a direct comparison to the scalar mesons in the Munczek model is not possible, we see a trend that the mass of the light scalar tetraquark and the scalar  $\bar{q}q$  meson is not so different. A similar low mass scalar  $\bar{q}q$  meson is found in a beyond rainbow ladder study employing a vertex model that takes into account parts of the skeleton-expanded vertex

DSE [150] (soon to be published) and is also found when using the plain Maris-Tandy model, see ref. [80] for just *one* reference.

This light mass is in contrast to the findings in [127], where the authors used a Ball-Chiu like vertex, reinforced by transverse pieces associated with the anomalous chromomagnetic moments of the quark, that yielded a mass for the scalar of about  $1.2 \text{ GeV}$ . Also the authors in [101] found a somewhat higher mass of about  $0.8 \text{ GeV}$  for the scalar meson including pion back-reaction effects. Consequently, the question of the position of the  $\bar{q}q$  *only* meson in the hadron spectrum within a DSE/BSE approach stays open.

In the case of the tetraquark we draw a different conclusion. Because we found the light, scalar tetraquark being dominated by the pion, we suspect that this feature will prevail in truncations beyond the Maris-Tandy model. Our reasoning is summarized in the following two points:

- Because the pion is a Goldstone boson, its mass is small. This feature should be maintained by *any* sensible truncation.
- The pion appears as a phase space singularity in the tetraquark and dominates its properties. Because of the low pion mass this will be the case for *any* sensible truncation.

Thus we hypothesize that the pion dominance, combined with the Goldstone nature of the pion, will ensure a low mass scalar tetraquark in all truncations. After resolving the issue of threshold effects, this hypothesis could be further tested explicitly in future studies by calculating  $\bar{q}q$  *and* tetraquarks in a beyond rainbow ladder truncation, taking into account mixing effects.

# Appendices

# A. Appendix - Tetraquarks

## A.1. Eigenvalue curves

To obtain the masses of the tetraquarks we extrapolated the curves

$$\frac{1}{\lambda} - 1 \quad (\text{A.1.1})$$

and searched for the crossing with zero. For this we employed a linear and parabolic extrapolation. The curves and the extrapolation can be seen in the plots below. The linear extrapolation took only into account the last few points to the left, because the curves are clearly not linear. Still this procedure is justified when taking into account that the calculated points do not vary so much in magnitude and the crossing is quite close to the last calculated point. The parabolic fit is much better, but in the region of the cusp, a crossing is not visible because the curves bend up beforehand. To still deduce a mass, we take the maximum of the curve as ‘bound-state mass’. From a technical point of view this is not satisfactory, but from a physical point of view we are only interested in the gross features of the spectrum, putting extrapolation errors and small inconsistencies around the cusp at a lower priority.

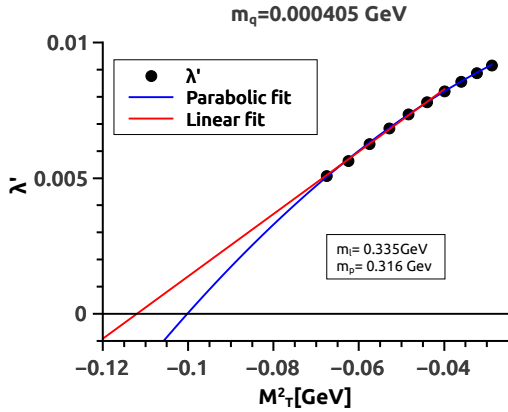


Figure A.1.:  $m_q = 0.00405$  GeV

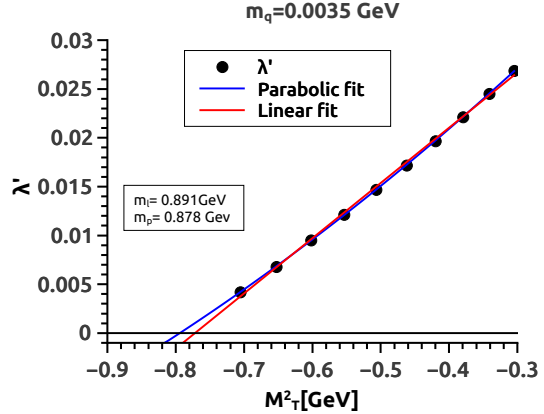


Figure A.2.:  $m_q = 0.035$  GeV

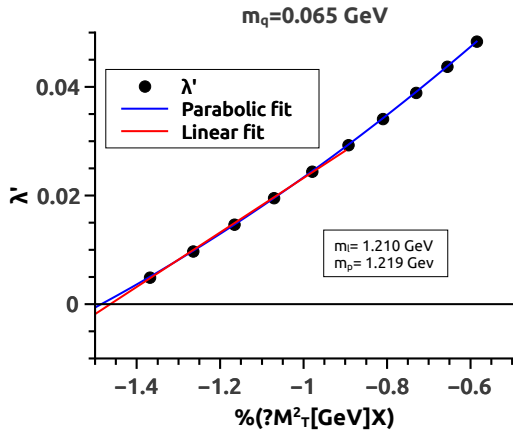


Figure A.3.:  $m_q = 0.065 \text{ GeV}$

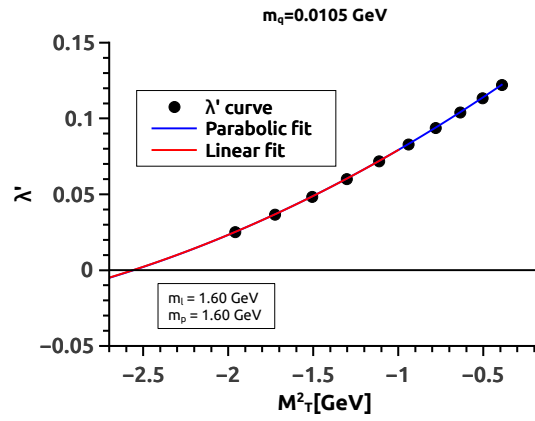


Figure A.4.:  $m_q = 0.105 \text{ GeV}$

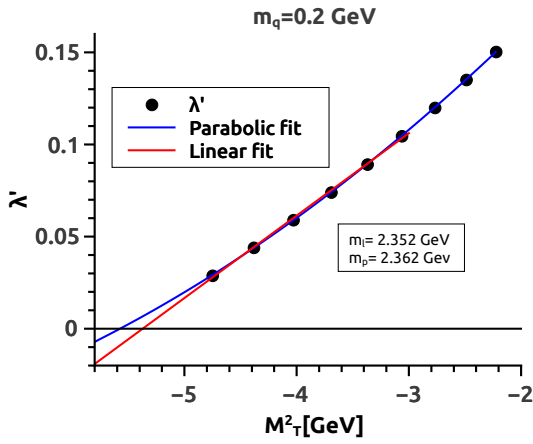


Figure A.5.:  $m_q = 0.2 \text{ GeV}$

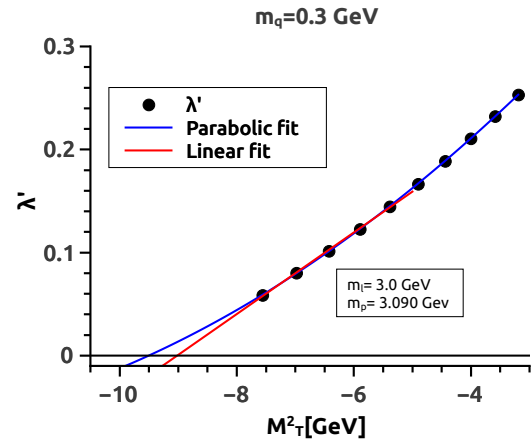


Figure A.6.:  $m_q = 0.3 \text{ GeV}$

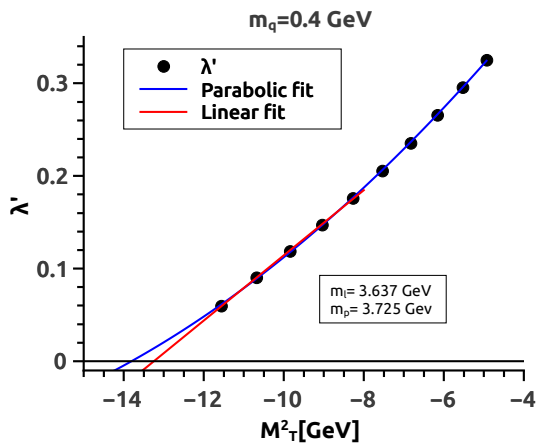


Figure A.7.:  $m_q = 0.4 \text{ GeV}$

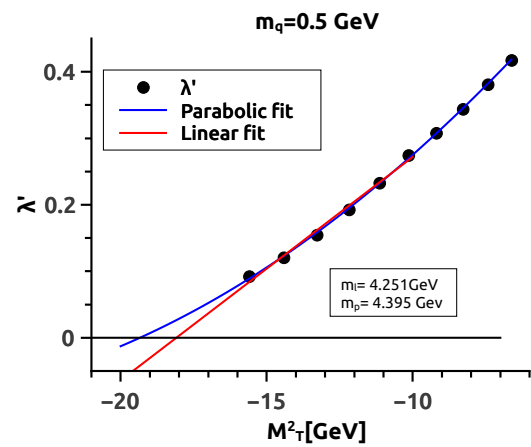


Figure A.8.:  $m_q = 0.5 \text{ GeV}$

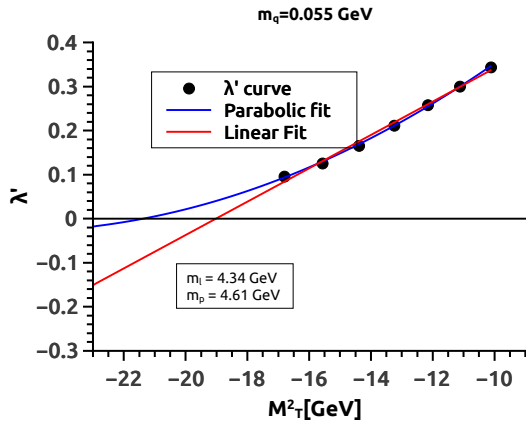


Figure A.9.:  $m_q = 0.55 \text{ GeV}$

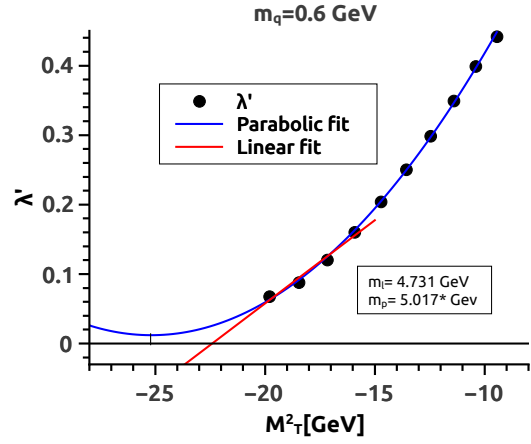


Figure A.10.:  $m_q = 0.6 \text{ GeV}$

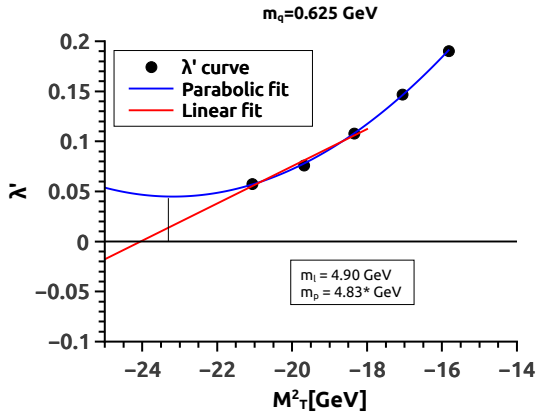


Figure A.11.:  $m_q = 0.625 \text{ GeV}$

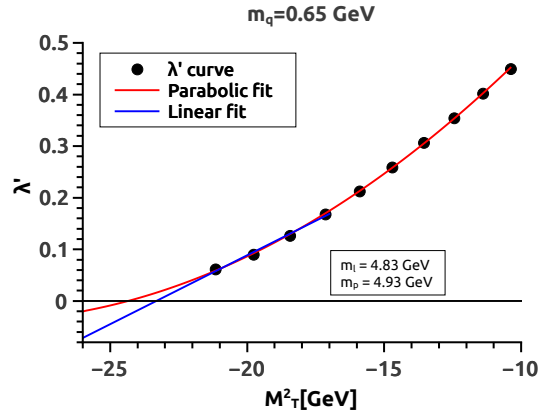


Figure A.12.:  $m_q = 0.65 \text{ GeV}$

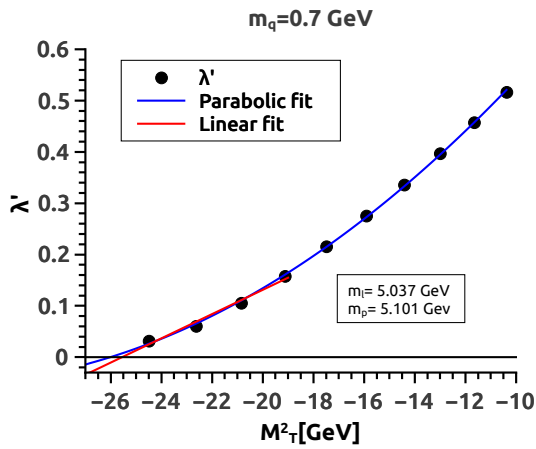


Figure A.13.:  $m_q = 0.7 \text{ GeV}$

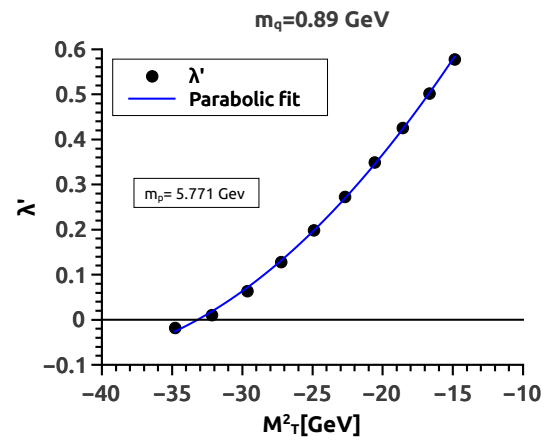
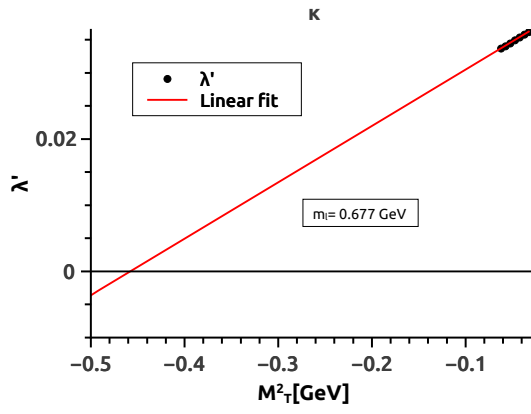
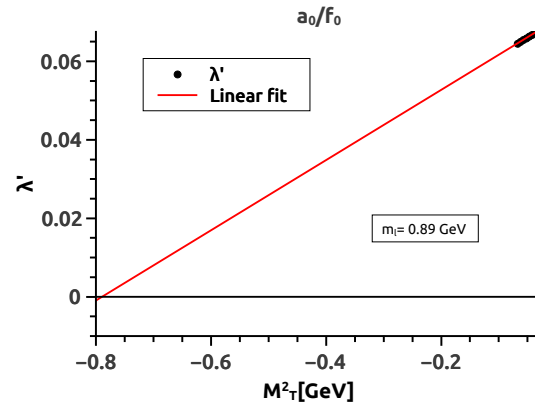


Figure A.14.:  $m_q = 0.89 \text{ GeV}$



**Figure A.15.:**  $m_u = 0.00405$  GeV,  
 $m_s = 0.105$  GeV.



**Figure A.16.:**  $m_u = 0.00405$  GeV,  
 $m_s = 0.105$  GeV.

## A.2. Phase space supplements

The radial variable is factorized into a permutation group invariant part and a bounded variable  $\hat{R} \in \{0, 1\}$ :

$$R = \hat{R} R_{max}$$

Because the four-vectors  $p_{1,2,3,4}$  are not independent, the phase space is a complicated geometrical object captured in the dependence of  $R_{max}$  on all other Lorentz invariants.

To reconstruct  $R_{max}$ , the following procedure is applied:

The triplet  $\mathcal{T}_0$  in spherical coordinates is equated with the triplet expressed in  $\omega'_i$  of eq. (3.2.4):

$$R \begin{pmatrix} -\cos \theta \\ \sin \theta \cos \phi \\ -\sin \theta \sin \phi \end{pmatrix} = \begin{pmatrix} -\frac{\omega'_1 + \omega'_2 + \omega'_3}{2\mathcal{S}_0} \\ -\sqrt{2} \frac{\omega'_1 + \omega'_2 - 2\omega'_3}{4\mathcal{S}_0} \\ \sqrt{6} \frac{\omega'_1 - \omega'_2}{4\mathcal{S}_0} \end{pmatrix}.$$

After inserting the momenta of eq. (3.2.6), this equation can be solved for the angles  $z, z', y$ .

$$\begin{aligned} z' &= R \frac{(\sqrt{3}\mathcal{T}_0|_3 - A) \sqrt{\frac{2}{9}}}{\bar{\Omega}_{23}} := a_1 R \\ z &= R \frac{(-\sqrt{3}\mathcal{T}_0|_3 - A) \sqrt{\frac{2}{9}}}{\bar{\Omega}_{13}} := a_2 R \\ y &= R \frac{-a_3 - (a_1 \bar{\Omega}_{23} + a_2 \bar{\Omega}_{13} + a_1 a_2 R^2 \bar{\Omega}_{12})}{\bar{\Omega}_{12} \sqrt{1 - a_1^2 R^2} \sqrt{1 - a_2^2 R^2}} \end{aligned} \quad (\text{A.2.1})$$

with

$$\begin{aligned} \mathcal{T}_0|_1 &= -\cos \theta, \quad \mathcal{T}_0|_2 = \sin \theta \cos \phi, \quad \mathcal{T}_0|_3 = -\sin \theta \sin \phi \\ A &= \sqrt{2}\mathcal{T}_0|_1 + \mathcal{T}_0|_2 \\ \bar{\Omega}_{12} &= \frac{1}{\mathcal{S}_0 M^2} \sqrt{M^2 p^2 + \rho_1^2} \sqrt{M^2 q^2 + \rho_2^2} \\ \bar{\Omega}_{23} &= \frac{1}{\mathcal{S}_0 M^2} \sqrt{M^2 q^2 + \rho_2^2} \sqrt{M^2 k^2 + \rho_3^2} \\ \bar{\Omega}_{13} &= \frac{1}{\mathcal{S}_0 M^2} \sqrt{M^2 p^2 + \rho_1^2} \sqrt{M^2 k^2 + \rho_3^2} \\ a_1 &= \frac{(\sqrt{3}\mathcal{T}_0|_3 - A) \sqrt{\frac{2}{9}}}{\bar{\Omega}_{23}} \\ a_2 &= \frac{(-\sqrt{3}\mathcal{T}_0|_3 - A) \sqrt{\frac{2}{9}}}{\bar{\Omega}_{13}} \\ a_3 &= 2\mathcal{T}_0|_1. \end{aligned} \quad (\text{A.2.2})$$

The equations for  $z, z'$  can be immediately solved for  $R_{max}$  by setting  $z = \pm 1$  and  $z' = \pm 1$ . The equation for  $y$  can be transformed into a cubic equation, which can be solved

analytically. The resulting cubic equation is of the form

$$a R_{max}^3 + b R_{max}^2 + c R_{max} + d = 0, \quad (\text{A.2.3})$$

with

$$\begin{aligned} a &= -\bar{\Omega}_{12} & (\text{A.2.4}) \\ b &= 0 \\ c &= (a_1^2 + a_2^2) \bar{\Omega}_{12}^2 + (a_3 + a_2 \bar{\Omega}_{13} + d \bar{\Omega}_{23})^2 \\ d &= 2a_1 a_2 \bar{\Omega}_{12} (a_3 + a_2 \bar{\Omega}_{13} + a_1 \bar{\Omega}_{23}). \end{aligned}$$

There are some special cases:

**a=0** The cubic equations reduces to a quadratic one and can be solved as such:

$$R_{1,2} = \frac{-c \pm \sqrt{c^2 - 4bd}}{2b} \quad (\text{A.2.5})$$

Otherwise the cubic equation is solved by

$$\begin{aligned} R_{1,2,3} &= 2\sqrt{|p|/3} y_{1,2,3} - \frac{1}{3}b/a & (\text{A.2.6}) \\ y_n &= \cos(1/3 \cos^{-1}(C) + (2n)2/3 \pi) \\ p &= 3c/a - \frac{(b/a)^2}{3} \\ q &= \frac{9(c/a)(b/a) - 27d/a - 2(b/a)^2}{27} \\ C &= \frac{1}{2} q (3/|p|)^{3/2} \end{aligned}$$

Two of these three solutions turn out to be negative. We choose the one which is positive.  $R_{max}$  is the minimum of the three calculated  $(R_{max})_{z,z',y}$ , because the phase space boundary is defined by the property that at least one of the angles  $z, z', y$  is maximal or minimal that means  $\pm 1$ .

A similar procedure is used to calculate the maximal radius  $\rho_{max}$ .

The triplet  $\mathcal{T}_1$  in spherical coordinates is equated with the triplet expressed in  $\eta_i$ :

$$\rho \begin{pmatrix} -\cos \vartheta \\ \sin \vartheta \cos \xi \\ -\sin \vartheta \sin \xi \end{pmatrix} = \begin{pmatrix} \frac{\eta_1 + \eta_2 + \eta_3}{2\sqrt{3}\sqrt{\mathcal{S}_0} M^2} \\ \frac{\eta_1 + \eta_2 - 2\eta_3}{2\sqrt{6}\sqrt{\mathcal{S}_0} M^2} \\ \frac{\eta_2 - \eta_1}{2\sqrt{2}\sqrt{\mathcal{S}_0} M^2} \end{pmatrix}.$$

After inserting the momenta of eq. (3.2.6), this equation can be solved for  $c_1, c_2, c_3$ (3.2.6):

$$\begin{aligned}
c_1 &= \frac{-(2\sqrt{3}\cos\vartheta - \sqrt{6}\sin\vartheta\cos\xi - 3\sqrt{2}\sin\vartheta\sin\xi)\rho}{3r_1} \\
c_2 &= \frac{-(2\sqrt{3}\cos\vartheta - \sqrt{6}\sin\vartheta\cos\xi + 3\sqrt{2}\sin\vartheta\sin\xi)\rho}{3r_2} \\
c_3 &= \frac{-(2\sqrt{3}\cos\vartheta + 2\sqrt{6}\sin\vartheta\cos\xi)\rho}{3r_3}
\end{aligned} \tag{A.2.7}$$

with

$$\begin{aligned}
r_1 &= \sqrt{\frac{4}{3}(1 + r r_{max} \cos(\varphi + 2\pi/3))} \\
r_2 &= \sqrt{\frac{4}{3}(1 + r r_{max} \cos(\varphi - 2\pi/3))} \\
r_3 &= \sqrt{\frac{4}{3}(1 + r r_{max} \cos(\varphi))}.
\end{aligned} \tag{A.2.8}$$

To find  $\rho_{max}$  we set  $c_{1,2,3}$  to  $\pm 1$  and calculate  $\rho$ . The minimum of the three possible  $\rho_{max}$  is the correct one because the phase space boundary is defined by the surface on which at least one of the angles is  $\pm 1$ .

### A.3. Color traces

We provide the explicit colour traces needed in the calculations of this work. We will denote the colour singlet in the different decompositions as  $3_D, 6_D, 1_{M_I}, 8_{M_I}, 1_{M_{II}}, 8_{M_{II}}$ . The subscripts denote the decompositions introduced in chapter 3.5.

For example,  $3_D$  is the singlet that can be formed by first coupling the two fundamental triplets  $3$  to a anti-triplet  $\bar{3}$ , coupled with the triplet formed by the coupling of the two anti-fundamental triplets:

$$\begin{aligned}
(3 \otimes 3) \otimes (\bar{3} \otimes \bar{3}) &= \bar{3} \otimes 3 \oplus \bar{6} \otimes 6 \oplus \dots = 1_{\bar{3} \otimes 3} \oplus 1_{\bar{6} \otimes 6} \oplus \dots =: 3_D \oplus 6_D \oplus \dots \\
(\bar{3} \otimes 3)_{13} \otimes (3 \otimes \bar{3})_{24} &= 1 \otimes 1 \oplus 8 \otimes 8 \oplus \dots = 1_{1 \otimes 1} \oplus 1_{8 \otimes 8} \oplus \dots =: 1_{M_I} \oplus 8_{M_I} \oplus \dots \\
(\bar{3} \otimes 3)_{14} \otimes (3 \otimes \bar{3})_{23} &= 1 \otimes 1 \oplus 8 \otimes 8 \oplus \dots = 1_{1 \otimes 1} \oplus 1_{8 \otimes 8} \oplus \dots =: 1_{M_{II}} \oplus 8_{M_{II}} \oplus \dots
\end{aligned} \tag{A.3.1}$$

The two possible ways to combine  $3$  and  $\bar{3}$  is denoted by the subscripts. The important numerical factors are the colour traces of the different diagrams and the Fierz-factors to change from one decomposition to the other. Each diagram is calculated in the colour decomposition that is the most suitable one. That means if the diagram connects the quark line 1 and 3, we use the  $M_I$  decomposition and so on. In this decompositions, the diagrams are diagonal in the colour space.

The Fierz table for the three different colour decompositions reads

Diagram	Structure	Factor
12/34	$3_D$	$-2/3$
12/34	$6_D$	$1/3$
13/24	$1_{M_I}$	$4/3$
13/24	$8_{M_I}$	$-1/6$
14/23	$1_{M_{II}}$	$4/3$
14/23	$8_{M_{II}}$	$-1/6$

**Table A.1.:** Color factors of the different diagrams. Numbers in the diagram column specify the quark lines that are connected by a gluon. Each diagram is diagonal in one of the three decompositions. To change from one decomposition to the other see the Fierz table below.

$$3_D = \sqrt{\frac{1}{3}} 1_{M_I} + \sqrt{\frac{2}{3}} 8_{M_I} \quad (\text{A.3.2})$$

$$6_D = -\sqrt{\frac{2}{3}} 1_{M_I} + \sqrt{\frac{1}{3}} 8_{M_I} \quad (\text{A.3.3})$$

$$1_{M_I} = \sqrt{\frac{1}{9}} 1_{M_{II}} + \sqrt{\frac{8}{9}} 8_{M_{II}} \quad (\text{A.3.4})$$

$$8_{M_I} = \sqrt{\frac{8}{9}} 1_{M_{II}} - \sqrt{\frac{1}{9}} 8_{M_{II}} \quad (\text{A.3.5})$$

#### A.4. Momentum routing and $S_4$ relations

In this section we provide the details of the momentum routing and some computational technicalities. The kernels depicted in figure A.17, can be discretized and stored as matrices. The calculation of the right hand side of the BSE is therefore nothing else than a matrix-vector multiplication. We call the application of these matrices 'overlap', and the appropriate matrices overlap matrices.

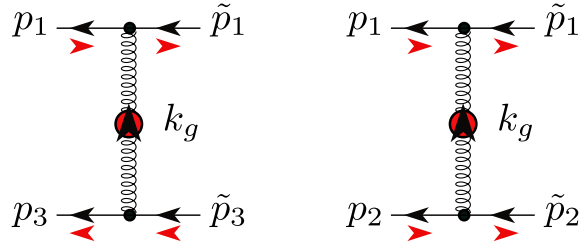


**Figure A.17.:** The left panel specifies the momentum routing for the Diagram  $I_{1,3}$  and the right panel the momentum routing for the diagram  $I_{1,2}$ . The momentum  $k_g$  denotes the momentum of the gluon, the tilded momenta contain the loop momentum  $l$ . The black arrows specify the direction of the momentum flow and the red arrows the direction of the quark spin-line.

The six one-loop diagrams  $I_{i,j}$  (see figure 2.4), labeled by the number of quark lines that are connected by gluons, use the following momentum routing:

**Diagram  $I_{1,2}$**  The gluon momentum  $k_g$  and the *internal* relative momenta  $\tilde{p}, \tilde{q}, \tilde{k}$  read

$$k_g = l + q - p \quad (\text{A.4.1})$$

$$\tilde{p} = q + l \quad (\text{A.4.2})$$

$$\tilde{q} = p - l \quad (\text{A.4.3})$$

$$\tilde{p} = k. \quad (\text{A.4.4})$$

The momentum  $l$  is the integration momentum. Beware that the spin line of the quarks has the opposite direction of the momentum flow direction.

**Diagram  $I_{3,4}$**  Under a  $P_{13,24}$  permutation, this diagram has the same structure and momentum routing than  $I_{1,2}$ . We exploit this feature by applying this transformation to the full amplitude structure (tensor, colour, flavour). After this transformation we can reuse the precalculated kernel of the  $I_{1,2}$  diagram. Afterwards, the result has to be back transformed by applying the same  $P_{13,24}$  transformation. For the two-loop diagram denoted by  $I_{1,2;3,4}$ , we use the factorization of the loops. Each loop can be calculated independent of the other one. So first we calculate the  $I_{1,2}$  diagram with its corresponding overlap matrix. Subsequently, we perform a  $P_{13,24}$  transformation on the result and multiply this transformed amplitude with the overlap matrix of the  $I_{1,2}$  diagram. Afterwards we back transform the result. Thus we only need to store the  $I_{1,2}$  matrix.

The transformations are easily performed because of the inherent symmetry of the tensor structure and the phase space: In the case of the tensor structures, a  $P_{13,24}$  transformation changes the sign as can be deduced from table 3.8 and in the case of the phase space variables, this symmetry operation amounts to an interpolation in  $z_R, \Phi_R, z_\rho, \Phi_\rho$  only. The rest of the variables are invariant.

**Diagram  $I_{1,3}$**  The following momentum routing is used for the  $I_{1,2}$  diagram

$$k_g = l + k - p \quad (\text{A.4.5})$$

$$\tilde{p} = k + l \quad (\text{A.4.6})$$

$$\tilde{q} = q \quad (\text{A.4.7})$$

$$\tilde{p} = p - l. \quad (\text{A.4.8})$$

**Diagram  $I_{1,4}$**  This diagram can be calculated with the same overlap matrix of the  $I_{1,3}$  diagram. The necessary transformation operations are the  $P_{34}$  permutation. This transformation is again a simple transformation when using the tensor structure given in table 3.8 and phase space variables provided in chapter 3.2.

**Diagram  $I_{2,4}$**  The transformation to relate this diagram to the overlap matrix of  $I_{1,3}$  is  $P_{12,34}$ .

**Diagram  $I_{2,3}$**  The transformation to relate this diagram to the overlap matrix of  $I_{1,3}$  is  $P_{12}$ .

The same factorization procedure that was used to calculate the two-loop diagram  $I_{1,2;3,4}$ , can be used to calculate the other two-loop diagrams  $I_{1,2;2,4}$  and  $I_{1,4;2,3}$ .

## A.5. $S_4$ toolbox

In this chapter we collect the different multiplets of  $S_4$  and products between them. This chapter is entirely based on ref. [106] and will be published soon.

### Construction of multiplets

A triplet  $\mathcal{T}^\pm$  and a doublet  $\mathcal{D}$  are elements of the three or two dimensional vector space on which the corresponding representations of the  $S_4$  group act on. They will be denoted by

$$\mathcal{T}^\pm = \begin{pmatrix} u \\ v \\ w \end{pmatrix} \quad \mathcal{D} = \begin{pmatrix} a \\ s \end{pmatrix}. \quad (\text{A.5.1})$$

To construct them, we start from the 24 elements of  $S_4$ , denoted by

$$f_{ijkl} \quad i, j, k, l \in \{1, 2, 3, 4\}. \quad (\text{A.5.2})$$

Any transposition  $P_{ij}$  exchanges the corresponding indices, e.g.,

$$P_{13}f_{2314} = f_{2134}. \quad (\text{A.5.3})$$

We collect them into three objects

$$f^{(1)} = \begin{bmatrix} f_{1234} \\ f_{3412} \\ f_{2143} \\ f_{4321} \end{bmatrix} \quad f^{(2)} = \begin{bmatrix} f_{3241} \\ f_{1423} \\ f_{4132} \\ f_{2314} \end{bmatrix} \quad f^{(3)} = \begin{bmatrix} f_{4213} \\ f_{2431} \\ f_{3124} \\ f_{1324} \end{bmatrix}. \quad (\text{A.5.4})$$

With  $P_\pm := 1 \pm P_{12}$ , one can form the combinations

$$\psi_i^\pm = P_\pm \sum_{k=1}^4 f_k^i, \quad i \in \{1, 2, 3\}. \quad (\text{A.5.5})$$

With these objects at hand, the singlet  $\mathcal{S}$  and antisinglet  $\mathcal{A}$  of the  $S_4$  group can be constructed:

$$\begin{aligned} \mathcal{S} &= (\psi_1^+ + \psi_2^+ + \psi_3^+) \\ \mathcal{A} &= (\psi_1^- + \psi_2^- + \psi_3^-). \end{aligned} \quad (\text{A.5.6})$$

They transform with a plus or minus respectively under *any* group operation  $P_{ij}$ . The doublets can be constructed with the help of the same objects:

$$\begin{aligned}\mathcal{D}_1 &= \begin{pmatrix} (\psi_2^- - \psi_3^-) \\ -\frac{1}{\sqrt{3}}(\psi_2^+ + \psi_3^+ - 2\psi_1^+) \end{pmatrix} \\ \mathcal{D}_2 &= \begin{pmatrix} \frac{1}{\sqrt{3}}(\psi_2^- + \psi_3^- - 2\psi_1^-) \\ (\psi_2^+ - \psi_3^+) \end{pmatrix}.\end{aligned}\tag{A.5.7}$$

With the additional definitions

$$\begin{aligned}a_i^\pm &:= P_\pm \left( f_1^{(i)} - f_2^{(i)} + f_3^{(i)} - f_4^{(i)} \right) \\ b_i^\pm &:= P_\pm \left( f_1^{(i)} - f_2^{(i)} - f_3^{(i)} + f_4^{(i)} \right) \\ c_i^\pm &:= P_\pm \left( -f_1^{(i)} - f_2^{(i)} + f_3^{(i)} + f_4^{(i)} \right)\end{aligned}\tag{A.5.8}$$

and

$$\begin{aligned}(\Phi_1)_1^\pm &:= \pm a_1^\pm & (\Phi_1)_2^\pm &:= a_2^\pm & (\Phi_1)_3^\pm &:= a_3^\pm \\ (\Phi_2)_1^\pm &:= \pm b_1^\pm & (\Phi_2)_2^\pm &:= b_2^\pm & (\Phi_2)_3^\pm &:= b_3^\pm \\ (\Phi_3)_1^\pm &:= \pm c_1^\pm & (\Phi_3)_2^\pm &:= c_2^\pm & (\Phi_3)_3^\pm &:= c_3^\pm\end{aligned}\tag{A.5.9}$$

we can construct the two triplets

$$\begin{aligned}\mathcal{T}_i^+ &= \begin{pmatrix} \sqrt{\frac{2}{3}}(\Phi_1^+ + \Phi_2^+ + \Phi_3^+) \\ \sqrt{\frac{1}{3}}(\Phi_2^+ + \Phi_3^+ - 2\Phi_1^+) \\ (\Phi_2^- - \Phi_3^-) \end{pmatrix} \\ \mathcal{T}_i^- &= \begin{pmatrix} \sqrt{\frac{2}{3}}(\Phi_1^- + \Phi_2^- + \Phi_3^-) \\ \sqrt{\frac{1}{3}}(\Phi_2^- + \Phi_3^- - 2\Phi_1^-) \\ (\Phi_2^+ - \Phi_3^+) \end{pmatrix}.\end{aligned}\tag{A.5.10}$$

With the representation matrices  $M, M', H, H', H''$  found in [105]<sup>1</sup> the action of a group member  $P_{ij}$  on the doublets and triplets can be written as a matrix-vector multiplication

---

<sup>1</sup>Slightly different notation as found in [105].

of the matrices with the doublets and triplets constructed beforehand:

$$M = \begin{pmatrix} -1 & 0 \\ 0 & 1 \end{pmatrix} \quad M' = \frac{1}{2} \begin{pmatrix} 1 & -\sqrt{3} \\ \sqrt{3} & 1 \end{pmatrix} \quad (\text{A.5.11})$$

$$H = \begin{pmatrix} 1 & 0 & 0 \\ 0 & 1 & 0 \\ 0 & 0 & 1 \end{pmatrix} \quad H' = \frac{1}{2} \begin{pmatrix} 1 & 0 & 0 \\ 0 & -1 & -\sqrt{3} \\ 0 & -\sqrt{3} & 1 \end{pmatrix} \quad H'' = \frac{1}{2} \begin{pmatrix} -1 & -\sqrt{8} & 0 \\ -\sqrt{8} & 1 & 0 \\ 0 & 0 & 3 \end{pmatrix} \quad (\text{A.5.12})$$

$$\begin{aligned} P_{12}\mathcal{D}_i &= M\mathcal{D}_i & P_{12}\mathcal{T}_i^\pm &= \pm H\mathcal{T}_i^\pm \\ P_{23}\mathcal{D}_i &= M'\mathcal{D}_i & P_{23}\mathcal{T}_i^\pm &= \pm H'\mathcal{T}_i^\pm \\ P_{34}\mathcal{D}_i &= M\mathcal{D}_i & P_{34}\mathcal{T}_i^\pm &= \pm H''\mathcal{T}_i^\pm \end{aligned} \quad (\text{A.5.13})$$

All other transpositions in  $S_4$  can be constructed by chaining  $P_{12}, P_{23}, P_{34}$  or by repeated multiplication of the matrices  $M, M', H, H', H''$ .

### Products in $S_4$

From the doublets and triplets of  $S_4$  one can construct again doublets, triplets and (anti-)singlets by appropriate combinations/multiplications.

**Doublets** The star product  $*$  between doublets and triplets is defined as follows

$$\begin{aligned} \mathcal{D} * \mathcal{D}' &:= \begin{pmatrix} as' + sa' \\ aa' - ss' \end{pmatrix} \\ \mathcal{T} * \mathcal{T}' &:= \begin{pmatrix} vw' + wv' + \sqrt{2}(uw' + wu') \\ ww' - vv' + \sqrt{2}(wv' + vu') \end{pmatrix}. \end{aligned} \quad (\text{A.5.14})$$

With the help of this product one can form new doublets by multiplying the following objects

$$\mathcal{D}_i * \mathcal{D}_j, \quad \mathcal{T}_i^\pm * \mathcal{T}_j^\pm, \quad \epsilon \left( \mathcal{T}_i^\pm * \mathcal{T}_j^\mp \right) \quad (\text{A.5.15})$$

with the additional matrix

$$\epsilon := \begin{pmatrix} 0 & 1 \\ -1 & 0 \end{pmatrix}. \quad (\text{A.5.16})$$

**Triplets** Triplets can be obtained from the two products denoted  $\vee$  and  $\wedge$

$$\begin{aligned} \mathcal{T} \wedge \mathcal{T}' &:= \begin{pmatrix} vw' - wv' \\ wu' - uw' \\ uv' - vu' \end{pmatrix} & \mathcal{T} \vee \mathcal{T}' &:= \begin{pmatrix} vv' + ww' - 2uu' \\ wv' + vu' + \sqrt{2}(vv' - ww') \\ wu' + wu' - \sqrt{2}(wv' + wv') \end{pmatrix} \\ \mathcal{T} \wedge \mathcal{D} &:= \begin{pmatrix} va - ws \\ ua - \sqrt{\frac{1}{2}}(va + ws) \\ -us - \sqrt{\frac{1}{2}}(vs + wa) \end{pmatrix} & \mathcal{T} \vee \mathcal{D} &:= \begin{pmatrix} vs + wa \\ us - \sqrt{\frac{1}{2}}(vs - wa) \\ ua + \sqrt{\frac{1}{2}}(va + ws) \end{pmatrix}. \end{aligned} \quad (\text{A.5.17})$$

The following combinations are possible to form triplets  $\mathcal{T}^+$

$$S\mathcal{T}^+, \quad \mathcal{A}\mathcal{A}^-, \quad \mathcal{T}^+ \wedge \mathcal{D}, \quad \mathcal{T}^- \vee \mathcal{D}, \quad \mathcal{T}^\pm \wedge \mathcal{T}^\pm, \quad \mathcal{T}^\pm \vee \mathcal{T}^\mp. \quad (\text{A.5.18})$$

**Singlets** Singlets can be formed by the standard scalar product, denoted by ' $\cdot$ ', in three and two dimensions

$$\mathcal{D}_i \cdot \mathcal{D}_j, \quad \mathcal{T}_i^\pm \cdot \mathcal{T}_j^\pm. \quad (\text{A.5.19})$$

Additionally, the products of singlets and antisinglets can also yield a singlet

$$S\mathcal{S}, \quad \mathcal{A}\mathcal{A}. \quad (\text{A.5.20})$$

**Antisinglets** With the help of the product ' $\wedge$ ' between doublets, defined as

$$\mathcal{D} \wedge \mathcal{D}' := a s' - s a', \quad (\text{A.5.21})$$

the antisinglets can be build from the following combinations

$$S\mathcal{A}, \quad \mathcal{D}_i \wedge \mathcal{D}_j, \quad \mathcal{T}_i^\pm \cdot \mathcal{T}_j^\mp. \quad (\text{A.5.22})$$

## B. Appendix - Beyond rainbow ladder

### B.1. Constructing beyond ladder kernels

Here we detail the construction of type *II* kernels in order to provide a self-contained definition that should help the reader who is interested in the numerical implementation. We consider in particular the *ABC* vertex construction from Eq. (9.2.2). The quark dressing functions are taken to be the ones from Eq. (9.2.1).

The kernels are of the form

$$\left. \frac{\delta \Sigma^{ab}(k)}{\delta S^{cd}(q)} \right|_{II} = \int_l [\gamma_\mu S(l)]^{aa'} \frac{\delta \Gamma_\mu^{a'b}(l, k)}{\delta S^{cd}(q)} D_{\mu\nu}(l - k), \quad (\text{B.1.1})$$

where the vertex from Eq. (9.2.2) using the generalization from Eq. (9.1.1) is written as

$$\begin{aligned} \Gamma_\mu^{ABC}(l, k) &= \gamma_\mu \frac{A_\mu(l) + A_\mu(k)}{2} \\ &+ (l + k)_\mu \sum_{\alpha=1}^4 (l + k)_\alpha \gamma_\alpha \frac{1}{2} \frac{A_\alpha(l) - A_\alpha(k)}{l^2 - k^2} \\ &+ i (l + k)_\mu \frac{B(l) - B(k)}{l^2 - k^2} + i \gamma_5 (l + k)_\mu \frac{C(l) - C(k)}{l^2 - k^2}, \end{aligned} \quad (\text{B.1.2})$$

which is the analog of the Ball-Chiu construction for the quark shown in Eq. (9.2.1). The cutting is now explicitly done as

$$\frac{\delta}{\delta S^{cd}(q)} = \sum_{j=1}^4 \frac{\gamma_j^{dc}}{i 4 q_j} \frac{\delta}{\delta \sigma_j(q)} + \frac{\mathbb{1}^{dc}}{4} \frac{\delta}{\delta \sigma_S(q)} + \frac{\gamma_5^{dc}}{4} \frac{\delta}{\delta \sigma_5(q)} \quad (\text{B.1.3})$$

The functional derivatives that occur are of the form

$$\frac{\delta A_i(p)}{\delta \sigma_j(q)} = \frac{\partial A_i}{\partial \sigma_j}(p) \delta^{(4)}(p - q), \quad (\text{B.1.4})$$

and similar for the *B* and *C* functions. We need to specify *A*, *B* and *C* in terms of the  $\sigma$ -dressings. The quark and its' inverse defined as in Eq. (9.2.1) are related by

$$\begin{aligned} A_i &= \frac{\sigma_i}{\sum_i^4 p_i^2 \sigma_i^2 + \sigma_S^2 - \sigma_5} & \rightarrow & \frac{\sigma_V}{p^2 \sigma_V^2 + \sigma_S^2} \\ B &= \frac{\sigma_S}{\sum_i^4 p_i^2 \sigma_i^2 + \sigma_S^2 - \sigma_5} & \rightarrow & \frac{\sigma_S}{p^2 \sigma_V^2 + \sigma_S^2} \\ C &= -\frac{\sigma_5}{\sum_i^4 p_i^2 \sigma_i^2 + \sigma_S^2 - \sigma_5} & \rightarrow & 0, \end{aligned} \quad (\text{B.1.5})$$

where the expressions after ' $\rightarrow$ ' are the ones after  $\sigma_{1\dots 4} \rightarrow \sigma_V$  and  $\sigma_5 \rightarrow 0$ , i.e. the physical ones that are used in all numerical calculations. The 'unphysical' expressions in

Eq. (B.1.5) are only needed for the cutting procedure during the derivation of the type  $II$  kernels. The coefficient matrix from Eq. (B.1.4) evaluates to

$$\frac{\partial(A_i|B|C)}{\partial\sigma_j} = \frac{1}{\mathcal{N}^2} \begin{bmatrix} D_1 & \Sigma_2^V & \Sigma_3^V & \Sigma_4^V & \Sigma^{VS} & 0 \\ \Sigma_1^V & D_2 & \Sigma_3^V & \Sigma_4^V & \Sigma^{VS} & 0 \\ \Sigma_1^V & \Sigma_2^V & D_3 & \Sigma_4^V & \Sigma^{VS} & 0 \\ \Sigma_1^V & \Sigma_2^V & \Sigma_3^V & D_4 & \Sigma^{VS} & 0 \\ \Sigma_1^{VS} & \Sigma_2^{VS} & \Sigma_3^{VS} & \Sigma_4^V & D_S & 0 \\ 0 & 0 & 0 & 0 & 0 & -\mathcal{N} \end{bmatrix}, \quad (\text{B.1.6})$$

with

$$\begin{aligned} \mathcal{N} &= p^2 \sigma_V^2 + \sigma_S^2 & D_i &= \sigma_V^2 \left( \left( \sum_{j \neq i} p_j^2 \right) - p_i^2 \right) + \sigma_S^2 \\ D_S &= p^2 \sigma_V^2 - \sigma_S^2 & \Sigma_i^V &= -2\sigma_V^2 p_i^2 \\ \Sigma_i^{VS} &= -2\sigma_V \sigma_S p_i^2 & \Sigma^{VS} &= -2\sigma_V \sigma_S. \end{aligned} \quad (\text{B.1.7})$$

Note that momentum  $p$  in the equations above will be evaluated as  $l$  or  $k$  in equation (B.1.2). The type  $II$  kernel for the vertex model from Eq. (9.2.2) is now almost fully specified. In addition we adjust the momentum dependence in order to take into account the flow of the total momentum of the bound-state through the kernel. This procedure is explained in appendix B.2 for the case of the  $\delta C/\delta\sigma_5$  part.

## B.2. Massless pion and BC vertex

In this appendix we show how the Ball-Chiu vertex (Eq. (9.0.3)) can yield a massless pion in the chiral limit via the extended structure of the vertex from Eq. (9.2.2). The only type  $II$  term in the kernel originating from cutting the  $ABC$  vertex of Eq. (9.2.2) and contributing to the AXWTI (8.0.6) and the pion BSE (8.0.12) evaluates to (see appendix B.1)

$$\begin{aligned} \frac{\delta\Sigma^{cd}(k)}{\delta S^{ab}(q)} &= -\gamma_5^{ba}/4 \\ &\times \left[ [\gamma_\mu S(q)\gamma_5]^{cd} \frac{i(q+k)_\nu}{q^2 - k^2} \frac{D_{\mu\nu}(q-k)}{q^2 \sigma_V^2(q^2) + \sigma_S^2(q^2)} \right. \\ &\quad \left. - \int_l [\gamma_\mu S(l)\gamma_5]^{cd} \frac{i(l+k)_\nu}{l^2 - k^2} \frac{D_{\mu\nu}(l-k)}{k^2 \sigma_V^2(k^2) + \sigma_S^2(k^2)} \delta^{(4)}(q-k) \right]. \end{aligned} \quad (\text{B.2.1})$$

We mentioned already in section 8 that the kinematics of the kernels generated is not automatically given by the cutting procedure. The self-energy  $\Sigma(k)$  expects the same incoming and outgoing momenta. The kernel that is generated from its derivative should have different momenta  $k_+$  and  $k_-$  to match the kinematics needed in the bound-state equation (8.0.12). If the cutting were carried out in coordinate space, this ambiguity would not arise. In order to arrive at a fully specified kernel one should use Eq. (8.0.1) without assuming translational invariance but only relaxing all Green functions to physical ones

in the end. We were, however, so far unable to write down the Ball-Chiu construction (9.0.3) for a quark with different in- and out-going momenta, or, probably preferable, in coordinate space. In our numerical calculation we thus work with a momentum-shifted version of Eq. (B.2.1) which reads

$$\begin{aligned}
K_{II}^{ABC}(P, q, k)_{ab}^{cd} &= -\gamma_5^{ba}/4 \tag{B.2.2} \\
&\times \left[ [\gamma_\mu S(q) \gamma_5]^{cd} \frac{i(q+k_+)_\nu}{q^2 - k_+^2} \frac{D_{\mu\nu}(q-k)}{q^2 \sigma_V^2(q^2) + \sigma_S^2(q^2)} \right. \\
&\quad \left. - \int_l [\gamma_\mu S(l) \gamma_5]^{cd} \frac{i(l+k_+)_\nu}{l^2 - k_+^2} \frac{D_{\mu\nu}(l-k) \delta^{(4)}(q-k)}{k_+^2 \sigma_V^2(k_+^2) + \sigma_S^2(k_+^2)} \right].
\end{aligned}$$

Our reasoning for this expression is twofold. First of all it does respect the fact that the total momentum  $P$  that should be part of the kernel, as explained above. Second, the singular terms of the form  $1/(q^2 - k^2)$  are potentially dangerous in the integration. This is regularized due to the replacement  $k \rightarrow k_+ = k + P/2$ , where  $P$  is imaginary ( $P^2 = -m_\pi^2$ ). It turns out that with this momentum routing a cancellation between the two types of structures present in Eq. (B.2.2) occurs. This cancellation mechanism resembles the vertex structure from Eq. (9.2.2), where the same type of denominator occurs. However, since the quotient approaches a form that is reminiscent of a derivative  $dC(k^2)/dk^2$  the zero-momentum limit is well defined.

We will now show that the AXWTI, Eq. (8.0.6), is fulfilled in the limit of  $P \rightarrow 0$ . For the case of the type I contribution to the kernel, only the third term of the Ball-Chiu vertex, Eq. (9.0.3), is a problem (cf. section 9.1). This is because the  $\gamma_5$ 's on the right hand side of equation (8.0.6) have to anti-commute with the vertices to give an additional minus sign to match the left side of the equation (cf. Fig. 8.1). This works out for the first two components of the BC vertex:  $\{\Gamma_\mu^{2BC}, \gamma_5\} = 0$ . The third component generates a term with the wrong sign since  $[\Gamma_\mu^{3rdBC}, \gamma_5] = 0$ . It turns out, however, that the type II contributions to the kernel, Eq. (9.2.3), remedy the problem: they equal to twice the same contribution but with opposite sign and therefore effectively switch the sign.

In order to be explicit we will start to check the AXWTI, Eq. (8.0.6) for the case of a bare vertex  $\Gamma_\mu(q, p) = \gamma_\mu$  in Eq. (8.0.9), i.e. the rainbow-ladder case. The essential manipulation in Eq. (8.0.6) is

$$\begin{aligned}
& - \int_q [S(q_+) \gamma_5]^{cd} K_{cd}^{ab}(P, q, k) \tag{B.2.3} \\
&= - \int_q \gamma_\mu S(q_+) \gamma_5 \gamma_\nu D_{\mu\nu}(k-q) \\
&= \int_q \gamma_\mu S(q) \gamma_\nu D_{\mu\nu}(k_+ - q) \gamma_5 = \Sigma(k_+) \gamma_5,
\end{aligned}$$

which then matches a corresponding term on the left side of equation (8.0.6). For the case

of a generic vertex that fulfills  $\{\Gamma_\mu(q, k), \gamma_5\} = 0$  we find

$$\begin{aligned}
& - \int_q [S(q_+) \gamma_5]^{cd} K_{cd}^{ab}(P, q, k) \\
& = - \int_q \gamma_\mu S(q_+) \gamma_5 \Gamma_\nu(q_-, k_-) D_{\mu\nu}(k - q) \\
& = \int_q \gamma_\mu S(q) \Gamma_\nu(q_- - P/2, k_-) D_{\mu\nu}(k_+ - q) \gamma_5 \\
& \xrightarrow{P \rightarrow 0} \int_q \gamma_\mu S(q) \Gamma_\nu(q, k) D_{\mu\nu}(k - q) \gamma_5 = \Sigma(k) \gamma_5,
\end{aligned} \tag{B.2.4}$$

such that the AXWTI is fulfilled at  $P = 0$ . For a vertex component, such as the third term of the BC part in Eq. (9.0.3) that obeys  $[\Gamma_\mu, \gamma_5] = 0$  the contribution has the wrong sign, such that even at  $P = 0$  the AXWTI is not fulfilled.

We will see that this problem can be cured by including a contribution of type *II*. Using the definition  $f_\nu(q, k) = (q + k)_\nu / (q^2 - k^2)$ , the self-energy for the third BC component on the left hand side of the AXWTI reads

$$\int_q \gamma_\mu S(q) f_\nu(q, k_+) (B(q) - B(k_+)) D_{\mu\nu}(k_+ - q) \gamma_5. \tag{B.2.5}$$

The corresponding diagram on the right side of the AXWTI has the opposite sign as already stated above. Therefore we consider now the contribution of the type *II* kernel from Eq. (B.2.1). The corresponding *C* part of the vertex (9.2.2) is zero and does not contribute to the self-energies on the left side of the AXWTI. For simplicity we will use the function  $f_\nu$  again and also the function  $\mathcal{N}$  from Eq. (B.1.7).

$$\begin{aligned}
& - \int_q [S(q_+) \gamma_5]^{cd} K_{cd}^{ab}(P, q, k) = \frac{1}{4} \int_q \text{Tr} [S(q_+) \gamma_5 \gamma_5] \times \\
& \quad \left[ \gamma_\mu S(q) \gamma_5 \frac{f_\nu(q, k_+)}{\mathcal{N}(q)} D_{\mu\nu}(q - k) \right. \\
& \quad \left. - \int_l \gamma_\mu S(l) \gamma_5 \frac{f_\nu(l, k_+)}{\mathcal{N}(k_+)} D_{\mu\nu}(l - k) \delta(q - k) \right] \\
& = \int_q \gamma_\mu S(q) f_\nu(q, k_+) \frac{\sigma_S(q_+)}{\mathcal{N}(q)} D_{\mu\nu}(q - k) \gamma_5 \\
& \quad - \int_l \gamma_\mu S(l) f_\mu(l, k_+) \frac{\sigma_S(k_+)}{\mathcal{N}(k_+)} D_{\mu\nu}(l - k) \gamma_5 \\
& = \int_q \gamma_\mu S(q) f_\mu(q, k_+) \left[ \frac{\sigma_S(q_+)}{\mathcal{N}(q)} - \frac{\sigma_S(k_+)}{\mathcal{N}(k_+)} \right] D_{\mu\nu}(k - q) \gamma_5 \\
& \xrightarrow{P \rightarrow 0} \int_q \gamma_\mu S(q) f_\mu(q, k) (B(q) - B(k)) D_{\mu\nu}(k - q) \gamma_5.
\end{aligned} \tag{B.2.6}$$

Here  $\text{Tr}[S] = 4\sigma_S$  was used as well as the definition of the *B* function in Eq. (B.1.5). We see that the last line corresponds to Eq. (B.2.5) in the  $P \rightarrow 0$  limit. In fact the second contribution on the right side of the AXWTI (8.0.6) differs by  $S(k_+) \gamma_5 \rightarrow \gamma_5 S(k_-)$  such that in the  $P \rightarrow 0$  limit it yields the same contribution. Thus we have the contribution of Eq. (B.2.6) twice. Due to the global minus sign that comes from the definition of *C* in Eq. (B.1.5) we subtract the BC term from Eq. (B.2.5) twice such that the AXWTI is fulfilled in the  $P \rightarrow 0$  limit.

### B.3. Gluon model

In this work we use a model for the effective gluon propagator  $D_{\mu\nu}$  that was given in ref. [151]. In general the gluon is given in Landau gauge as

$$\tilde{D}_{\mu\nu}(k) = \left( \delta_{\mu\nu} - \frac{k_\mu k_\nu}{k^2} \right) \frac{Z(k^2)}{k^2}, \quad (\text{B.3.1})$$

where the non perturbative content is hidden in the dressing function  $Z(k^2)$ . In the Dyson-Schwinger equation for the quark propagator this dressing function appears together with the fully dressed non-Abelian quark-gluon vertex. Since all explicit vertices used in this work are constructed along the Abelian Ward-Takahashi identity, the following model for the effective gluon represents a product of the gluon propagator with the remaining non-Abelian dressing effects  $G\tilde{H}$  in the vertex, cf. the discussion around Eq. (9.0.3). The model is given by

$$\begin{aligned} \alpha_{\text{eff}}(k^2) &= \frac{g^2}{4\pi} Z_{1F} Z(k^2) G(k^2) \tilde{H}(k^2) \\ &= \pi\eta^7 \left( \frac{k^2}{\Lambda^2} \right)^2 e^{-\eta^2 \frac{k^2}{\Lambda^2}} \\ &\quad + \frac{2\pi\gamma_m (1 - e^{-k^2/\Lambda_t^2})}{\ln[e^2 - 1 + (1 + k^2/\Lambda_{QCD}^2)^2]}, \end{aligned} \quad (\text{B.3.2})$$

where for the anomalous dimension of the quark we use  $\gamma_m = 12/(11N_c - 2N_f) = 12/25$ , corresponding to  $N_f = 4$  flavours and  $N_c = 3$  colours, we fix the QCD scale to  $\Lambda_{QCD} = 0.234$  GeV and the scale  $\Lambda_t = 1$  GeV is introduced for technical reasons and has no impact on the results. The interaction strength is characterized by an energy scale  $\Lambda$  and the dimensionless parameter  $\eta$  controls the width of the interaction. The precise form of this model does not matter in this work. Ultimately we aim to replace this with a self-consistently calculated gluon propagator, see e.g. ref. [137], and an appropriate expression for the non-Abelian parts of the vertex.

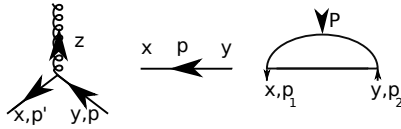


**Figure B.1.:** From left to right: Vertex, Propagator, Amplitude.  $x, y, z$  letters denote space time positions,  $p$  letters denote the corresponding momentum.

## B.4. Munczek model

To cut the quark self-energy of the Munczek model, a formulation in position space is necessary. The building blocks read as following:

$$\begin{aligned}\Gamma^\mu(z; x, y) &= \int_{p', p} e^{-ip'(x-z)-ip(z-y)} \Gamma^\mu(p', p) \\ S(x, y) / D^{\mu\nu}(x, y) &= \int_p e^{-ip(x-y)} S / D^{\mu\nu}(p) \\ A(x, y; P) &= \int_{p_1, p_2} e^{-ip_1 x + ip_2 y} A(p_1, p_2; P).\end{aligned}\quad (\text{B.4.1})$$

The first line represents a vertex in position space, the second a quark or gluon propagator and the third one the Bethe-Salpeter amplitude or wave function with total momentum  $P$ . We denote two further relations that play a role in the derivations:

$$\int_0^1 d\alpha e^{iq\alpha(x-y)} e^{iq(z-x)} = \frac{e^{iq(z-y)} - e^{iq(z-x)}}{iq \cdot (x-y)}, \quad (\text{B.4.2})$$

and

$$\frac{\delta}{\delta S(l, l')} S^{-1}(x', y) = -S^{-1}(l', y) S^{-1}(x', l). \quad (\text{B.4.3})$$

The first one is already used to represent the Munczek vertex model in [59], the second one denotes the functional derivative of an inverse propagator. With all tools at hand the Munczek vertex in momentum space is readily derived from Eq. (9.3.1):

$$\Gamma^\mu(p', p) = \frac{\partial}{\partial p_\mu} \int_0^1 S^{-1}(p + \alpha(p' - p)) d\alpha. \quad (\text{B.4.4})$$

Taking the functional derivative of the quark self-energy yields

$$\begin{aligned}\frac{\delta \Sigma(x_1, x_2)}{\delta S(l, l')} &= \int_{y, z} \gamma^\mu S(x_1, y) \frac{\delta \Gamma^\mu(z; y, x_2)}{\delta S(l, l')} D^{\mu\nu}(z, x_1) \\ &= \int_{y, z} \gamma^\mu S(x_1, y) D^{\mu\nu}(z, x_1) \int_q e^{iq(z-y)-iq(z-x_2)} \\ &\quad \times \frac{(x_2 - y)^\mu}{iq \cdot (x_2 - y)} \frac{\delta}{\delta S(l, l')} S^{-1}(y, x_2).\end{aligned}$$

This expression is now traced with the Bethe-Salpeter wave function from Eq.(B.4.1) (as demanded by the Bethe-Salpeter Equation in coordinate space) and Eq.(B.4.3) is inserted for the derivative of the inverse quark propagator. Additionally the  $\alpha$ -trick from Eq.(B.4.2) is applied resulting in the following expression

$$\begin{aligned}\frac{\delta \Sigma(x_1, x_2)}{\delta S(l, l')} &= - \int_{\substack{y, z \\ l', q}} \int_0^1 d\alpha \gamma^\mu S(x_1, y) D^{\mu\nu}(z, x_1) e^{iq\alpha(x_2-y)} \\ &\quad \times e^{iq(z-x_2)} (x_2 - y)^\mu S^{-1}(l', x_2) \tilde{\Gamma}(l', l; P) S^{-1}(y, l),\end{aligned}\quad (\text{B.4.5})$$

where  $\tilde{\Gamma}$  is the wave function (see Eq. (9.3.8)). Inserting the expressions for the vertex, propagators and amplitudes from Eq.(B.4.1) and replacing  $(x_2 - y)^\mu$  by appropriate derivatives of momenta in the exponentials of the Fourier modes, one finally arrives at the expression for the type *II* momentum space contribution:

$$[\Gamma \times K_{II}](P, p)|_{ab} = - \int_q \int_0^1 d\alpha \gamma_{ac}^\mu S_{cd}(q - \frac{1}{2}P) \times D^{\mu\nu}(q - p) \left[ \frac{\partial}{\partial q^\nu} (\Gamma_{db}(q + \alpha(q - p); P)) \right]. \quad (\text{B.4.6})$$

Color factors and renormalization constants are suppressed. In this case  $\Gamma$  denotes the wave function. and instead of the two momenta  $p_1$  and  $p_2$ , we use the relative momentum  $p = (p_1 - p_2)/2$  to describe the wave function. We included the Dirac indices to clarify the structure.

There is an asymmetry in this type *II* kernel as one can see in the quark momentum. This can lead to an imaginary part of the BSE eigenvalues at least in the form of numerical noise. The source for this is the asymmetry of the quark self-energy that contains only one dressed vertex. If one would start with a symmetrized self-energy

$$\Sigma(p) = \frac{1}{2} \int \gamma^\mu S(q) \Gamma^\nu(q, p) D^{\mu\nu}(p - q) \quad (\text{B.4.7})$$

$$+ \frac{1}{2} \int \Gamma^\mu(p, q) S(q) \gamma^\mu D^{\mu\nu}(p - q) \quad (\text{B.4.8})$$

this problem disappears and there is second type *II* contribution containing a quark with momentum  $q + \frac{1}{2}P$ :

$$[\Gamma \times K_{II}](P, p)|_{ab} = - \int_q \int_0^1 d\alpha \left[ \frac{\partial}{\partial q^\nu} (\Gamma_{ac}(q + \alpha(q - p); P)) \right] \times S_{cd}(q + \frac{1}{2}P) \gamma_{db}^\mu D^{\mu\nu}(q - p). \quad (\text{B.4.9})$$

Both contributions will come with a factor  $\frac{1}{2}$ .

# Bibliography

- [1] W. Heupel, T. Goecke, and C. S. Fischer, *Eur.Phys.J.* **A50**, 85 (2014), hep-ph/1402.5042.
- [2] PDG, K. Nakamura *et al.*, Note on scalar mesons, (2010).
- [3] M. Gell-Mann, *Phys.Lett.* **8**, 214 (1964).
- [4] Particle Data Group, K. Olive *et al.*, *Chin.Phys.* **C38**, 090001 (2014).
- [5] E. Witten, *Nucl.Phys.* **B156**, 269 (1979).
- [6] G. Veneziano, *Nucl.Phys.* **B159**, 213 (1979).
- [7] R. L. Jaffe, *Phys.Rev.* **D15**, 267 (1977).
- [8] E. Santopinto and G. Galata, *Phys.Rev.* **C75**, 045206 (2007), hep-ph/0605333.
- [9] R. Jaffe, *Phys.Rept.* **409**, 1 (2005), hep-ph/0409065.
- [10] I. Caprini, G. Colangelo, and H. Leutwyler, *Phys.Rev.Lett.* **96**, 132001 (2006), hep-ph/0512364.
- [11] S. Okubo, *Phys.Lett.* **5**, 165 (1963).
- [12] J. Iizuka, K. Okada, and O. Shito, *Prog.Theor.Phys.* **35**, 1061 (1966).
- [13] G. Zweig, CERN Report No. TH-412, (1964) (unpublished).
- [14] Particle Data Group, K. Olive *et al.*, *Chin.Phys.* **C38**, 090001 (2014).
- [15] G. 't Hooft, *Nucl.Phys.* **B75**, 461 (1974).
- [16] E. Witten, *Nucl.Phys.* **B160**, 57 (1979).
- [17] S. Coleman, *Aspects of Symmetry*, 1 ed. (Cambridge University Press, 1985).
- [18] S. Weinberg, *Phys.Rev.Lett.* **110**, 261601 (2013), hep-ph/1303.0342.
- [19] A. Esposito, A. L. Guerrieri, F. Piccinini, A. Pilloni, and A. D. Polosa, *Int.J.Mod.Phys.* **A30**, 1530002 (2015), hep-ph/1411.5997.
- [20] S. Protopopescu *et al.*, *Phys.Rev.* **D7**, 1279 (1973).
- [21] G. Grayer *et al.*, *Nucl.Phys.* **B75**, 189 (1974).

- [22] BES Collaboration, M. Ablikim *et al.*, Phys.Lett. **B598**, 149 (2004), hep-ex/0406038.
- [23] NA48-2, J. Batley *et al.*, Eur.Phys.J. **C70**, 635 (2010).
- [24] S. Roy, Phys.Lett. **B36**, 353 (1971).
- [25] R. Garcia-Martin, R. Kaminski, J. Pelaez, and J. Ruiz de Elvira, Phys.Rev.Lett. **107**, 072001 (2011), hep-ph/1107.1635.
- [26] G. Mennessier, S. Narison, and X. Wang, Phys.Lett. **B688**, 59 (2010), hep-ph/1002.1402.
- [27] J. Pelaez, PoS **CD12**, 047 (2013), 1303.0125.
- [28] S. Descotes-Genon and B. Moussallam, Eur.Phys.J. **C48**, 553 (2006), hep-ph/0607133.
- [29] M. Ablikim *et al.*, Phys.Lett. **B693**, 88 (2010), hep-ex/1002.0893.
- [30] KLOE-2, P. Gauzzi, J.Phys.Conf.Ser. **349**, 012002 (2012).
- [31] J. Pelez, J. Londergan, J. Nebreda, and A. Szczepaniak, Acta Phys.Polon.Supp. **7**, 539 (2014), hep-ph/1404.6058.
- [32] G. 't Hooft, G. Isidori, L. Maiani, A. Polosa, and V. Riquer, Phys.Lett. **B662**, 424 (2008), hep-ph/0801.2288.
- [33] H.-X. Chen, A. Hosaka, and S.-L. Zhu, Phys.Rev. **D76**, 094025 (2007), hep-ph/0707.4586.
- [34] D. Parganlija, F. Giacosa, and D. H. Rischke, Acta Phys.Polon.Supp. **3**, 963 (2010), 1004.4817.
- [35] D. Ebert, R. Faustov, and V. Galkin, Eur.Phys.J. **C60**, 273 (2009), hep-ph/0812.2116.
- [36] S. Prelovsek *et al.*, Phys.Rev. **D82**, 094507 (2010), hep-lat/1005.0948.
- [37] S. Prelovsek and D. Mohler, Phys.Rev. **D79**, 014503 (2009), hep-lat/0810.1759.
- [38] M. Wakayama *et al.*, (2014), hep-lat/1412.3909.
- [39] ETM, J. O. Daldrop *et al.*, PoS **LATTICE2012**, 161 (2012), hep-lat/1211.5002.
- [40] Belle, S. Choi *et al.*, Phys.Rev.Lett. **91**, 262001 (2003), hep-ex/0309032.
- [41] M. Padmanath, C. Lang, and S. Prelovsek, (2015), hep-lat/1503.03257.
- [42] Belle, Z. Liu *et al.*, Phys.Rev.Lett. **110**, 252002 (2013), hep-ex/1304.0121.
- [43] G. T. Bodwin *et al.*, (2013), 1307.7425.

- [44] N. Brambilla *et al.*, Eur.Phys.J. **C74**, 2981 (2014), hep-ph/1404.3723.
- [45] M. Peskin and D. Schroeder, *An Introduction To Quantum Field Theory*, 2 ed. (Westview Press, 1995).
- [46] P. Ramond, *Field Theory: A modern primer*, 2 ed. (Addison-Wesley, 1995).
- [47] L. Faddeev and V. Popov, Phys.Lett. **B25**, 29 (1967).
- [48] A. Slavnov, Theor.Math.Phys. **10**, 99 (1972).
- [49] J. Taylor, Nucl.Phys. **B33**, 436 (1971).
- [50] C. Becchi, A. Rouet, and R. Stora, Phys.Lett. **B52**, 344 (1974).
- [51] R. Alkofer, M. Q. Huber, and K. Schwenzer, Comput.Phys.Commun. **180**, 965 (2009), hep-th/0808.2939.
- [52] R. Alkofer and L. von Smekal, Phys.Rept. **353**, 281 (2001), hep-ph/0007355.
- [53] C. S. Fischer, J.Phys.G **G32**, R253 (2006), hep-ph/0605173.
- [54] P. Cvitanović, *Field Theory*, 1 ed. (Niels Bohr Institute, 2004).
- [55] E. Salpeter and H. Bethe, Phys.Rev. **84**, 1232 (1951).
- [56] C. Llewellyn-Smith, Annals Phys. **53**, 521 (1969).
- [57] M. Broido, Rept.Prog.Phys. **32**, 493 (1967).
- [58] J. Berges, S. Borsanyi, U. Reinosa, and J. Serreau, Annals Phys. **320**, 344 (2005), hep-ph/0503240.
- [59] H. Munczek, Phys.Rev. **D52**, 4736 (1995), hep-th/9411239.
- [60] A. Khvedelidze and A. Kvinikhidze, Theor.Math.Phys. **90**, 62 (1992).
- [61] K. Huang and H. A. Weldon, Phys.Rev. **D11**, 257 (1975).
- [62] S. Yokojima, M. Komachiya, and R. Fukuda, Nucl.Phys. **B390**, 319 (1993).
- [63] J. Bijtebier, (2000), hep-th/0010132.
- [64] M. Carrington, W. Fu, T. Fugleberg, D. Pickering, and I. Russell, Phys.Rev. **D88**, 085024 (2013), hep-ph/1310.3295.
- [65] H. Sanchis-Alepuz, C. S. Fischer, C. Kellermann, and L. von Smekal, (2015), hep-ph/1503.06051.
- [66] N. Nakanishi, Phys.Rev. **138**, B1182 (1965).
- [67] A. Krassnigg, PoS **CONFINEMENT8**, 075 (2008), nucl-th/0812.3073.

- [68] N. Ioakimidis, K. Papadakis, and E. Perdios, *BIT Numerical Mathematics* **31**, 276 (1991).
- [69] J.-P. Berrut and L. N. Trefethen, *SIAM Rev* **46**, 501.
- [70] H. Wang, D. Huybrechs, and S. Vandewalle, *ArXiv e-prints* (2012), hep-math/1202.0154.
- [71] M. Floater and K. Hormann, *Numerische Mathematik* **107**, 315 (2007).
- [72] R. Alkofer, W. Detmold, C. Fischer, and P. Maris, *Phys.Rev.* **D70**, 014014 (2004), hep-ph/0309077.
- [73] A. Bashir *et al.*, *Commun.Theor.Phys.* **58**, 79 (2012), nucl-th/1201.3366.
- [74] M. Bhagwat, M. Pichowsky, and P. C. Tandy, *Phys.Rev.* **D67**, 054019 (2003), hep-ph/0212276.
- [75] V. Hernandez, J. E. Roman, and V. Vidal, *ACM Trans. Math. Software* **31**, 351 (2005).
- [76] M. Blank, *Properties of quarks and mesons in the Dyson-Schwinger/Bethe-Salpeter approach*, PhD thesis, (2011), hep-ph/1106.4843v1.
- [77] P. Maris and P. C. Tandy, *Phys. Rev.* **C60**, 055214 (1999).
- [78] P. Maris and C. D. Roberts, *Phys.Rev.* **C56**, 3369 (1997), nucl-th/9708029.
- [79] V. Miransky, *Phys.Lett.* **B165**, 401 (1985).
- [80] C. S. Fischer, S. Kubrak, and R. Williams, *Eur.Phys.J.* **A50**, 126 (2014), hep-ph/1406.4370.
- [81] D. Nickel, C. S. Fischer, and J. Wambach, *eConf* **C070910**, 268 (2007), hep-ph/0711.0610.
- [82] S. L. Adler, *Phys.Rev.* **177**, 2426 (1969).
- [83] J. M. Cornwall, R. Jackiw, and E. Tomboulis, *Phys.Rev.* **D10**, 2428 (1974).
- [84] P. Maris, C. D. Roberts, and P. C. Tandy, *Physics Letters B* **420**, 267 (1998).
- [85] C. S. Fischer, S. Kubrak, and R. Williams, *Eur.Phys.J.* **A51**, 10 (2015), hep-ph/1409.5076.
- [86] T. Hilger, C. Popovici, M. Gomez-Rocha, and A. Krassnigg, *Phys.Rev.* **D91**, 034013 (2015), hep-ph/1409.3205.
- [87] M. Blank and A. Krassnigg, *Phys.Rev.* **D84**, 096014 (2011), hep-ph/1109.6509.
- [88] D. Jarecke, P. Maris, and P. C. Tandy, *Phys.Rev.* **C67**, 035202 (2003), nucl-th/0208019.

- [89] C.-R. Ji and P. Maris, Phys.Rev. **D64**, 014032 (2001), nucl-th/0102057.
- [90] S. R. Cotanch and P. Maris, Phys.Rev. **D66**, 116010 (2002), hep-ph/0210151.
- [91] H. Sanchis-Alepuz, S. Kubrak, and C. Fischer, Int.J.Mod.Phys.Conf.Ser. **26**, 1460121 (2014).
- [92] G. Eichmann, R. Alkofer, A. Krassnigg, and D. Nicmorus, Phys.Rev.Lett. **104**, 201601 (2010), hep-ph/0912.2246.
- [93] D. Nicmorus, G. Eichmann, A. Krassnigg, and R. Alkofer, Phys.Rev. **D80**, 054028 (2009), hep-ph/0812.1665.
- [94] H. Sanchis-Alepuz and C. S. Fischer, Phys.Rev. **D90**, 096001 (2014), hep-ph/1408.5577.
- [95] R. Alkofer, G. Eichmann, H. Sanchis-Alepuz, and R. Williams, (2014), hep-ph/1412.8413.
- [96] G. Eichmann, Phys.Rev. **D84**, 014014 (2011), hep-ph/1104.4505.
- [97] G. Eichmann and C. S. Fischer, Phys.Rev. **D87**, 036006 (2013), hep-ph/1212.1761.
- [98] A. Bender, C. D. Roberts, and L. Von Smekal, Phys.Lett. **B380**, 7 (1996).
- [99] W. Heupel, G. Eichmann, and C. S. Fischer, Phys.Lett. **B718**, 545 (2012), hep-ph/1206.5129.
- [100] L. Chang and C. D. Roberts, Phys.Rev.Lett. **103**, 081601 (2009), nucl-th/0903.5461.
- [101] R. Williams and C. S. Fischer, Chin.Phys. **C34**, 1500 (2010), hep-ph/0912.3711.
- [102] C. S. Fischer and R. Williams, Phys.Rev. **D78**, 074006 (2008), hep-ph/0808.3372.
- [103] R. Williams, (2014), hep-ph/1404.2545.
- [104] H. Sanchis-Alepuz and R. Williams, (2015), hep-ph/1503.05896.
- [105] v. B. E, *Some notes on group theory*, 1 ed. (Universidade de Coimbra, 1998).
- [106] G. Eichmann, C. Fischer, and W. Heupel, in preparation (2015).
- [107] G. Eichmann, C. S. Fischer, W. Heupel, and R. Williams, (2014), hep-ph/1411.7876.
- [108] S. Dorkin, L. Kaptari, T. Hilger, and B. Kampfer, Phys.Rev. **C89**, 034005 (2014), hep-ph/1312.2721.
- [109] T. Langer, A. G. Belyaev, and H. Seidel, SGP , 81 (2006).
- [110] J. de Swart, Rev.Mod.Phys. **35**, 916 (1963).
- [111] T. A. Kaeding, Atom.Data Nucl.Data Tabl. **61**, 233 (1995), nucl-th/9502037.

- [112] A. Alex, M. Kalus, A. Huckleberry, and J. von Delft, *J.Math.Phys.* **52**, 023507 (2011), math-ph/1009.0437.
- [113] G. Eichmann, *Hadron properties from QCD bound-state equations*, PhD thesis, 2009, hep-ph/0909.0703.
- [114] M. Srednicki, *Quantum Field Theory*, 2 ed. (Cambridge University Press, 2007).
- [115] J. S. Goldstone, *Phys.Rev.* **91**, 1516 (1953).
- [116] W. Kaufmann, *Phys.Rev.* **187**, 2051 (1969).
- [117] N. Seto, *Prog.Theor.Phys.Suppl.* **95**, 25 (1988).
- [118] N. Seto and I. Fukui, *Prog.Theor.Phys.* **89**, 205 (1993).
- [119] S. Ahlig and R. Alkofer, *Annals Phys.* **275**, 113 (1999), hep-th/9810241.
- [120] K. Higashijima, *Phys.Rev.* **D18**, 2128 (1978).
- [121] M. Gell-Mann, R. Oakes, and B. Renner, *Phys.Rev.* **175**, 2195 (1968).
- [122] C. Hanhart, J. Pelaez, and G. Rios, *Phys.Lett.* **B739**, 375 (2014), hep-ph/1407.7452.
- [123] M. Wagner *et al.*, *J.Phys.Conf.Ser.* **503**, 012031 (2014), hep-lat/1310.6905.
- [124] R. J. Lloyd and J. P. Vary, *Phys.Rev.* **D70**, 014009 (2004), hep-ph/0311179.
- [125] Y. Iwasaki, *Prog.Theor.Phys.* **54**, 492 (1975).
- [126] E. Klempt and A. Zaitsev, *Phys.Rept.* **454**, 1 (2007), 0708.4016.
- [127] L. Chang and C. D. Roberts, *Phys.Rev.* **C85**, 052201 (2012), nucl-th/1104.4821.
- [128] A. Krassnigg, *Phys.Rev.* **D80**, 114010 (2009), hep-ph/0909.4016.
- [129] J. Meyers and E. S. Swanson, *Phys.Rev.* **D87**, 036009 (2013), hep-ph/1211.4648.
- [130] D. W. McKay and H. J. Munczek, *Phys.Rev.* **D40**, 4151 (1989).
- [131] P. Maris, C. D. Roberts, and P. C. Tandy, *Phys.Lett.* **B420**, 267 (1998), nucl-th/9707003.
- [132] P. Maris and C. D. Roberts, *Int.J.Mod.Phys.* **E12**, 297 (2003), nucl-th/0301049.
- [133] P. Maris and P. Tandy, *Nucl.Phys.Proc.Suppl.* **161**, 136 (2006), nucl-th/0511017.
- [134] T. Goecke, C. S. Fischer, and R. Williams, *Phys.Lett.* **B704**, 211 (2011), hep-ph/1107.2588.
- [135] G. Eichmann, R. Alkofer, I. Cloet, A. Krassnigg, and C. Roberts, *Phys.Rev.* **C77**, 042202 (2008), nucl-th/0802.1948.

- [136] S.-x. Qin, L. Chang, Y.-x. Liu, C. D. Roberts, and D. J. Wilson, *Phys.Rev.* **C85**, 035202 (2012), nucl-th/1109.3459.
- [137] C. S. Fischer and R. Alkofer, *Phys.Rev.* **D67**, 094020 (2003), hep-ph/0301094.
- [138] P. Watson, W. Cassing, and P. Tandy, *Few Body Syst.* **35**, 129 (2004), hep-ph/0406340.
- [139] M. Bhagwat, A. Holl, A. Krassnigg, C. Roberts, and P. Tandy, *Phys.Rev.* **C70**, 035205 (2004), nucl-th/0403012.
- [140] H. H. Matevosyan, A. W. Thomas, and P. C. Tandy, *Phys.Rev.* **C75**, 045201 (2007), nucl-th/0605057.
- [141] R. Alkofer, C. S. Fischer, F. J. Llanes-Estrada, and K. Schwenzer, *Annals Phys.* **324**, 106 (2009), hep-ph/0804.3042.
- [142] C. S. Fischer, D. Nickel, and J. Wambach, *Phys.Rev.* **D76**, 094009 (2007), hep-ph/0705.4407.
- [143] C. S. Fischer and R. Williams, *Phys.Rev.Lett.* **103**, 122001 (2009), hep-ph/0905.2291.
- [144] C. Fischer, P. Watson, and W. Cassing, *Phys.Rev.* **D72**, 094025 (2005), hep-ph/0509213.
- [145] L. Chang, Y.-X. Liu, and C. D. Roberts, *Phys.Rev.Lett.* **106**, 072001 (2011), nucl-th/1009.3458.
- [146] J. Berges, *Phys.Rev.* **D70**, 105010 (2004), hep-ph/0401172.
- [147] J. S. Ball and T.-W. Chiu, *Phys.Rev.* **D22**, 2542 (1980).
- [148] R. Alkofer, P. Watson, and H. Weigel, *Phys.Rev.* **D65**, 094026 (2002), hep-ph/0202053.
- [149] E. Eichten and F. Feinberg, *Phys.Rev.* **D10**, 3254 (1974).
- [150] R. Williams, in preparation (2015).
- [151] P. Maris and P. C. Tandy, *Phys.Rev.* **C60**, 055214 (1999), nucl-th/9905056.

# Danksagung

Zuallererst gilt mein Dank meinem Betreuer Professor Christian Fischer, für die interessante und spannende Themenstellung, die Möglichkeit meine Arbeit in seiner Arbeitsgruppe anfertigen zu dürfen sowie für die Begleitung und Unterstützung während der gesamten Promotion. Besonders bedanken möchte ich mich an dieser Stelle auch für die Freiheit während der Bearbeitung meines Forschungsprojektes sowie die vielen hilfreichen Diskussionen.

Außerdem möchte ich Dr. Gernot Eichmann danken, für dessen konstruktiven Ideen und wertvollen Rat die sehr bei der Bearbeitung des Teils über die Tetraquarks geholfen haben.

An meinen ehemaligen Kollegen Dr. Tobias Göcke möchte ich ein besonderes Dankeschön richten. Aus einer Idee in der Teeküche ist dank unserer gemeinsamen Anstrengungen die spannende Arbeit über den Munczekvertex entstanden.

Dr. Richard Williams und Dr. Helios Alepuz danke ich für die Erörterung spannender physikalischer Fragen, die vielen hilfreichen Diskussionen und dafür, dass ihr Büro und ihr Ohr immer offen stand.

Ganz besonderes herzlich möchte ich mich auch bei allen meinen Kollegen in der Arbeitsgruppe bedanken. Sie haben mich herzlich aufgenommen und standen mir immer mit Rat und Tat zur Seite. Besonders dankend erwähnen möchte ich an dieser Stelle die Teeküchler. Neben der notwendigen Gesellschaft in den Kaffeepausen haben wir auch so Manches ausserhalb des Instituts unternommen und damit die Promotionszeit unvergesslich gemacht.

Ein großes Dankeschön sei auch an alle die gerichtet, die mir diese Promotion ermöglicht haben: Meiner Familie und meinen Freunden danke ich, dass sie mich in dieser Zeit getragen, unterstützt und so manches Mal ertragen haben.

Auch denjenigen, die hier nicht einzeln namentlich erwähnt wurden und mich in der Promotionszeit unterstützt haben, sei es durch Gespräche, Aufmunterungen oder Unternehmungen, möchte ich danken. Eure Hilfe weiß ich sehr zu schätzen.

Der Helmholtz Graduate School for Hadron and Ion Research danke ich für das Stipendium, das diese Arbeit ermöglicht hat sowie die vielen hilfreichen und interessanten Seminare und Workshops.

# Selbstständigkeitserklärung

Ich erkläre:

Ich habe die vorgelegte Dissertation selbstständig und ohne unerlaubte fremde Hilfe und nur mit den Hilfen angefertigt, die ich in der Dissertation angegeben habe. Alle Textstellen, die wörtlich oder sinngemäß aus veröffentlichten Schriften entnommen sind, und alle Angaben, die auf mündlichen Auskünften beruhen, sind als solche kenntlich gemacht. Bei den von mir durchgeführten und in der Dissertation erwähnten Untersuchungen habe ich die Grundsätze guter wissenschaftlicher Praxis, wie sie in der Satzung der Justus-Liebig-Universität Gießen zur Sicherung guter wissenschaftlicher Praxis niedergelegt sind, eingehalten.

---

Ort, Datum

---

Walter Heupel